



저작자표시-비영리-변경금지 2.0 대한민국

이용자는 아래의 조건을 따르는 경우에 한하여 자유롭게

- 이 저작물을 복제, 배포, 전송, 전시, 공연 및 방송할 수 있습니다.

다음과 같은 조건을 따라야 합니다:



저작자표시. 귀하는 원저작자를 표시하여야 합니다.



비영리. 귀하는 이 저작물을 영리 목적으로 이용할 수 없습니다.



변경금지. 귀하는 이 저작물을 개작, 변형 또는 가공할 수 없습니다.

- 귀하는, 이 저작물의 재이용이나 배포의 경우, 이 저작물에 적용된 이용허락조건을 명확하게 나타내어야 합니다.
- 저작권자로부터 별도의 허가를 받으면 이러한 조건들은 적용되지 않습니다.

저작권법에 따른 이용자의 권리는 위의 내용에 의하여 영향을 받지 않습니다.

이것은 [이용허락규약\(Legal Code\)](#)을 이해하기 쉽게 요약한 것입니다.

[Disclaimer](#)

공학박사 학위논문

리튬 이차 전지의 양극과 전해질 간
계면 거동에 관한 연구

**A fundamental study on interfacial
behavior between cathode and
electrolyte in lithium rechargeable
batteries**

2019년 2월

서울대학교 대학원
재료공학부
성 원 모

Abstract

A fundamental study on interfacial behavior between cathode and electrolyte in lithium rechargeable batteries

Won Mo Seong

Department of Materials Science and Engineering

The Graduate School

Seoul National University

It is becoming highly crucial to meet the increasing demands on lithium rechargeable batteries with higher energy density than ever to apply this system currently prevailing in consumer electronics to large-scale energy storage systems and electric vehicles. Accomplishing this tough task can be highly supported by increasing energy density of cathode material in lithium rechargeable batteries, because it normally act as a bottleneck of total energy density of a battery. However, the methods to raise the energy density of cathode materials including widening operational range of conventional material and discovering new cathode material are now facing considerable obstacles: degradation problem at the cathode-electrolyte interface (CEI). These issues are receiving much more attention than ever because

battery now should endure much harsher condition such as high temperature and high voltage which promotes the notorious effects at CEI. Therefore, even if cathode material itself exhibits high energy density, formation of robust interface with electrolyte should be in advance to apply it to lithium rechargeable battery system. However, the thorough studies on this field is still scarce due to the needs on interdisciplinary research on cathode and electrolyte and limitation of evaluation tool at this narrow region. In this thesis, fundamental studies on interfacial behavior between cathode and electrolyte have been conducted to contribute to this unattended field.

In **Chapter 2**, it has revealed that the surface degradation by reaction between electrolyte salt and LiCoO_2 cathode material during short-term high-temperature storage led to the formation of lithium-rich material at the surface of LiCoO_2 . This material act as an internal parasite even after surrounding temperature cooled down, and chemically provide lithium to charged Li_xCoO_2 to permanently accelerate self-discharge rate of battery. This phenomenon is called as abnormal self-discharge, and detailed mechanism was suggested.

In **Chapter 3**, new method to modify surface of LiCoO_2 for high-voltage cycling was suggested. At extremely high-voltage condition, surface reconstruction layer of LiCoO_2 is rather dissolved out to exhibit superior cyclability compared with moderate high-voltage condition. This subtractive surface modification method also enabled us to decouple the effect of surface and bulk of LiCoO_2 in degrading battery performance during high-voltage cycling, and this new understanding on behavior of LiCoO_2 was thoroughly studied.

In **Chapter 4**, an effective method to suppress notorious interfacial dynamics was reported. During the synthesis of high-Ni $\text{LiNi}_{0.91}\text{Co}_{0.06}\text{Mn}_{0.03}\text{O}_2$, we injected reactive gas to form protective film by modifying residual lithium chemistry.

The large amount of surface LiOH and Li₂CO₃ on high-Ni layered cathode has been biggest obstacle for its commercialization and increase the synthetic cost by demand on post-treatment. However, this method ruled out the necessity of post-treatment to cut down the synthetic cost significantly, and simultaneously mitigated the several problems that has been caused by surface residual lithium.

Keywords: Lithium rechargeable batteries, Large-scale energy storage system (ESS), Electric vehicle (EV), Cathode-electrolyte interface (CEI), Surface reconstruction

Student Number: 2011-22865

Contents

List of Tables	ix
----------------------	----

List of Figures	x
-----------------------	---

Chapter 1. Introduction..... 1

1.1. Lithium rechargeable batteries for large-scale energy storage	2
1.2. Barriers of obtaining lithium batteries with high energy density	5
1.3. Interfacial dynamics between cathode and electrolyte in lithium batteries	12
1.3.1. Surface reconstruction of cathode material	13
1.3.2. Gas evolution by side reaction of CEI film or during CEI film formation	15
1.4. Purpose of this thesis	25
1.5. References	27

Chapter 2. Abnormal self-discharge in lithium-ion batteries 31

2.1. Introduction	31
2.2. Experimental section	31
2.2.1. Synthesis and characterization of LiCoO_2	34
2.2.2. Electrochemical Characterization of Li_xCoO_2	34
2.2.3. Conditions of self-discharge experiments for Li_xCoO_2	35
2.2.4. Characterization of Li_xCoO_2 electrodes	36
2.3. Results and discussion	40
2.3.1. Demonstration of abnormal self-discharge	40
2.3.2. Underlying mechanism of abnormal self-discharge.....	54
2.3.3. The origin of internal parasite	70
2.4. Results and discussion	80
2.5. References	81

Chapter 3. Unveiling the intrinsic cycle reversibility of a LiCoO_2 electrode at 4.8-V cut-off voltage through

subtractive surface modification for lithium-ion batteries	85
3.1. Introduction	85
3.2. Experimental section	89
3.2.1. Synthesis and characterization of pristine LiCoO ₂ powder.....	89
3.2.2. Electrochemical analyses	90
3.2.3. Characterizations of Li _x CoO ₂ electrodes after electrochemical test	90
3.3. Results and discussion	93
3.3.1. Inspiration: unexpected superior cyclability of LiCoO ₂ electrode at 4.8-V cut-off compared with 4.6-V cut-off.....	93
3.3.2. Mitigated surface construction: the origin of superior cyclability of LiCoO ₂ at 4.8-V cut-off	102
3.3.3. Suggestion of a new subtractive surface modification method	120
3.4. Conclusion	135
3.5. References	136

Chapter 4. Controlling residual lithium chemistry during the synthesis of high-Nickel (>90%)

Li(Ni_xCo_yMn_z)O₂ cathode.....	141
4.1. Introduction	141
4.1.1. Obstacles for commercialization of high-Ni (>80 %) layered cathode materials.....	141
4.1.2. Current understanding on residual lithium at high-Ni NCM surface	143
4.1.3. Several attempts to mitigate residual lithium in high-Ni NCM	144
4.1.4. Purpose of this research.....	144
4.2. Experimental section	146
4.2.1. Procedure of synthesis and SO ₂ -treatment of high-Ni LiNi _{0.91} Co _{0.06} Mn _{0.03} O ₂ powder	146
4.2.2. Characterization of LiNi _{0.91} Co _{0.06} Mn _{0.03} O ₂ powder	146
4.2.3. Electrode preparation and electrochemical analyses	147
4.3. Results and discussion	149
4.3.1. The suggestion of in-situ gas-phase reaction method for surface modification of high-Ni layered cathode material	149
4.3.2. Characterization of the surface of high-Ni layered cathode material	161
4.3.3. Optimization of battery performance of SO ₂ -treated NCM9163	175
4.4. Conclusion	186

4.5. Reference187

Chapter 5. Concluding remarks 191

Chapter 6. Abstract in Korean..... 193

Chapter 7. Curriculum Vitae 196

List of Tables

Table 1.2.1.	Characteristics of representative conventional cathode and anode materials for lithium rechargeable batteries; average potentials and theoretical/practical capacity.....	8
Table 1.2.2.	Elemental Characteristics of various representative cathode and materials with high average potential or specific capacity for lithium rechargeable batteries.....	9
<hr/>		
Table 3.3.1.	Concentration of dissolved cobalt ions in 1 M LiPF ₆ in EC/DMC (1:1 v/v) electrolyte from charged Li _x CoO ₂ measured by ICP-MS. The Li _x CoO ₂ electrodes for the measurement were retrieved from Li/LiCoO ₂ coin cells when the potential reached each cut-off at various cycle numbers: 1st, 10th, and 50th cycles with or without AlPO ₄ coating	134
<hr/>		
Table 4.3.1.	List of standard gibbs free energy of formation for various LiX compounds.....	158
Table 4.3.3.	Summary of the amount of residual lithium compounds at different reaction point with SO ₂ gas and ratio of I ₍₀₀₃₎ /I ₍₁₀₄₎ calculated from XRD pattern of corresponding NCM9163 powder. For	

	comparison, the amount of residual lithium compounds on NCM622 powder was also measured and corresponding results are shown.....	159
Table 4.3.3.	The amount of residual lithium compounds of NCM9163 powder which undergone the treatment with other kinds of gas than SO ₂ at ~500 °C during cooling.....	160
Table 4.3.4.	Summary of the amount of residual lithium compounds of Diluted-SO ₂ -treated NCM9163 whose battery performance showed optimized properties	185

List of Figures

Figure 1.1.1.	Comparison of the cost for discharged electrical energy as a function of cycling frequency.....	4
Figure 1.2.1.	Summary of characteristics of various electrochemical rechargeable batteries	10
Figure 1.2.2.	Representative voltage profile of Li _x CoO ₂ by extracting lithium electrochemically	11

Figure 1.3.1.	A comparison of voltage profile of Li/LiCoPO ₄ cell adopting conventional carbonate-based electrolyte (black line) and newly developed electrolyte (red line)	18
Figure 1.3.2.	Computation result of reduction and oxidation energy levels of broadly known lithium rechargeable battery electrolyte solvents and solvated salts.....	19
Figure 1.3.3.	Current understanding on the composition and distribution of the (a) SEI on anodes and (b) CEI on cathodes in lithium rechargeable batteries.	20
Figure 1.3.4.	Surface reconstruction of LiNi _{0.5} Co _{0.2} Mn _{0.3} O ₂ surface after 50 cycles under 3.0-4.5 V (vs. Li/Li ⁺) conditions observed by high-resolution transmission electron microscope (HR-TEM).....	21
Figure 1.3.5.	Schematic illustration of nucleophilic attack of aprotic electrolyte solvents.....	22
Figure 1.3.6.	Schematic illustration of oxygen evolution from LiCoO ₂ by electronic structure of it.....	23
Figure 1.3.7.	Oxygen evolution rate as a function of SOC of representative lithium transition metal oxide cathodes	24

Figure 2.2.1.	(a) XRD pattern, (b) SEM image, (c) and (d) high-resolution TEM (HRTEM) lattice image of LiCoO ₂ powder. The inset in (c) shows the fast Fourier transformation calculated from the entire image..	37
Figure 2.2.2.	(a) Charge-discharge profile at sixth cycle and (b) cycle stability of Li/LiCoO ₂ cell	38
Figure 2.2.3.	X-ray diffraction pattern of synthesized Li ₄ Ti ₅ O ₁₂ powder	39
Figure 2.3.1.	Comparison of voltage profiles of Li _x CoO ₂ before and after heating at 60 °C	45
Figure 2.3.2.	Representative voltage decay curve of Li _x CoO ₂ cathode charged to SOC 20 measured at 25 °C. Before the start of measurement, each coin cell was stored at various temperatures overnight, as indicated in the graph.....	46
Figure 2.3.3.	(a) SEM images of synthesized LiFePO ₄ particle, respectively. (b) Representative voltage decay curve of Li _x FePO ₄ and Li(Ni _{0.6} Co _{0.2} Mn _{0.2})O ₂ cathode charged to SOC 20, respectively, with/without 60 °C thermal history. Inset figure shows the representative voltage profile of Li/LiFePO ₄ cell. Current rate was set to 17 mA/g.	47
Figure 2.3.4.	(a) Voltage profiles and (b) dQ/dV^{-1} plots from (a) of self-discharged	

Li_xCoO₂ for which a thermal history at 60 °C was written obtained by recharging it with a current of 27 mA/g. The voltage profile was monitored until the 7th cycle, and the representative results are compared with that before the Li_xCoO₂ was self-discharged (marked as ‘Before SD (self-discharge)’).……………48

Figure 2.3.5. XRD pattern of Li_xCoO₂ electrode at SOC 0 approached by self-discharge of cathode (voltage decay to 3.3 V), which had been heated at 60 °C overnight compared with that of the electrode from the reference LiCoO₂. The inset shows the XRD pattern magnified near the (003) peak of Li_xCoO₂……………49

Figure 2.3.6. Voltage decay curve of LiCoO₂ cathode with thermal history at 60 °C at various SOCs (SOC 60 and 90). All the measurements were performed at 25 °C. In each case, the voltage decay behavior was universally observed upon storage at 60 °C ……………50

Figure 2.3.7. Summary statistics for time to complete self-discharge (when the potential of the Li/LiCoO₂ half-cell approached 3.3 V) at 25 °C collected from more than 5 samples charged to SOC 20 with different thermal histories. ……………51

Figure 2.3.8. (a) Typical charge/discharge profile of a full cell using a Li_xCoO₂ cathode and Li_{4+x}Ti₅O₁₂ anode. (b) Decay of OCV for a cell exposed to 60 °C heat treatment. The cathode was soaked in electrolyte

solution at 60 °C.....52

Figure 2.3.9. (a) Representative electrochemical voltage profile of Li/LiCoO₂ pouch-type cell. Current density for charge and discharge was set to 1 mA. Inset photograph shows the relative size of the pouch (left: 10 cm × 10 cm) compared with the conventional 2032 coin-type cell (right). The pouch-type cell was fabricated using 2 cm × 7 cm rectangular LiCoO₂ cathode, lithium metal anode, 1 M LiPF₆ in EC/DMC (1:1 v/v) and Celgard 2400 separator. (b) The probe of the voltage decay as a function of time for the pouch-cell containing Li_xCoO₂ cathode with/without 60 °C thermal history. The open-circuit-voltages of the two cells were monitored for 5 days.....53

Figure 2.3.10. TEM images of surface of Li_xCoO₂ with thermal history at 60 °C after self-discharge was performed: (a) low-magnification image and (b, c) high-magnification images of regions outlined by (b) white dashed square and (c) yellow dashed square in (a). (e) Fast Fourier transforms calculated from degraded region in (a). (d) High-magnification TEM image of degraded region of Li_xCoO₂ obtained directly after charging to SOC 20..... 61

Figure 2.3.11. TEM images of surface of Li_xCoO₂ without heating: (a) low-magnification image and (b) high-magnification image of region outlined by yellow dashed square in (a)..... 62

- Figure 2.3.12.** Low-magnification TEM image of Li_xCoO_2 obtained directly after charge to SOC 20 for which a thermal history of 60 °C was recorded.63
- Figure 2.3.13.** (a) Fast Fourier transforms calculated from degraded region in (a). (d) High-magnification TEM image of degraded region of Li_xCoO_2 obtained directly after charging to SOC 20. (b) Fast Fourier transform calculated from degraded region of charged Li_xCoO_264
- Figure 2.3.14.** Traces of XRD patterns of charged Li_xCoO_2 (SOC 20) electrode with thermal history at 60 °C. The electrodes were retrieved from the coin cell and rinsed, dried, and stored in an argon atmosphere.....65
- Figure 2.3.15.** Trace of XRD patterns of charged Li_xCoO_2 (SOC 20) electrode without thermal history.....66
- Figure 2.3.16.** (a) SEM image and (b) XRD pattern of synthesized Li_3P powder. Traces of XRD patterns of delithiated $\text{Li}_{0.9}\text{CoO}_2$ powder (c) mixed with Li_3P powder or (d) not mixed with Li_3P powder during storage in an argon atmosphere.....67
- Figure 2.3.17.** Change of open-circuit voltage of Li/LiCoO_2 cell with thermal history during storage which is allowed to decrease under 3.0 V. Inset shows the same figure magnified at the region nearby ~1.7 V.....68

Figure 2.3.18. (a) STEM image of surface region of charged Li_xCoO_2 with thermal history. The samples were prepared directly after the potential of the Li/LiCoO_2 half-cell decreased to ~ 3.3 V. Elemental mapping across the dashed line in (a) for (b) P, (d) F, (e) Co, and (f) C of Li_xCoO_2 surface after storage at 60°C and self-discharge. (c) EDS line profile of phosphorus across degraded region and bulk Li_xCoO_2 , as indicated by red arrow in (b). The orange dashed lines in (a)–(b) and (d)–(f) mark the same positions in each figure to guide the eye. 69

Figure 2.3.19. XPS depth profile of Li_xCoO_2 electrode (a) without thermal history and (b) with thermal history at 60°C . All the samples were charged to SOC 20 and analyzed after the self-discharge was complete. The sputtering time is indicated underneath each spectrum. 75

Figure 2.3.20. (a) Comparison of self-discharge rate of bare LiCoO_2 and LiCoO_2 with 60°C thermal history using electrolyte of 1 M LiClO_4 in EC/DMC (1:1 v/v). (b) Comparison of self-discharge rate of bare LiCoO_2 and LiCoO_2 with thermal history consisting of soaking the cathode electrode in EC/DMC (1:1 v/v) solvent without salt at 80°C . The self-discharge rate in (b) was measured using 1 M LiPF_6 in EC/DMC (1:1 v/v) electrolyte. 76

Figure 2.3.21. Schematic illustration of proposed mechanism for accelerated self-discharge rate based on the written thermal history at the surface of Li_xCoO_2 77

Figure 2.3.22. Simplified model for calculation of required Li_3P film thickness (a in the sphere right side) for chemical lithiation of charged sphere Li_xCoO_2 with radius of 1 μm 78

Figure 2.3.23. SEM image of surface of (a) pristine LiCoO_2 and (b) LiCoO_2 cycled at 4.8 V-cut off for 50 cycles. 79

Figure 3.2.1. Rietveld refinement results of HRPD pattern of synthesized LiCoO_2 . (b) SEM image of synthesized LiCoO_2 powder..... 92

Figure 3.3.1. XRD patterns of Li_xCoO_2 electrodes after charging to desired cut-off voltage..... 95

Figure 3.3.2. (a) Representative voltage-SOC profile of Li_xCoO_2 . (b) Ex-situ XRD pattern of Li_xCoO_2 electrodes charged to desired SOC indicated in graph..... 96

Figure 3.3.3. Galvanostatic charge/discharge profiles of Li/LiCoO_2 cell for upper cut-off voltage of (b) 4.6 and (c) 4.8 V. Applied current density is 27 mA g^{-1} 97

Figure 3.3.4. Cyclic voltammetry results of Li/LiCoO_2 cell for cycling at (a) 4.6-V and (b) 4.8-V cut-off potentials. The scan rate is 0.06 mV s^{-1} . 98

Figure 3.3.5.	Change of (d) specific discharge capacity and (e) energy efficiency of Li/LiCoO ₂ cell as electrochemical cycling proceeds.....	99
Figure 3.3.6.	(a) Discharge capacity retention and (b) energy efficiency of Li/Li _x CoO ₂ cells for electrochemical cycling at various upper potential cut-offs	100
Figure 3.3.7.	Summary of capacity retention of Li/LiCoO ₂ cells at various upper cut-off voltages.	101
Figure 3.3.8.	XRD patterns of discharged Li _x CoO ₂ electrodes after 50 cycles at 4.6- and 4.8-V cut-offs.	107
Figure 3.3.9.	SEM images of (a) pristine LiCoO ₂ , (b) LiCoO ₂ electrode cycled in 3.0–4.6 V range, and (c) LiCoO ₂ electrode cycled in 3.0–4.8 V range.....	108
Figure 3.3.10.	Deconvolution result of (003) plane XRD peak showing that this peak is composed of more than one peak. For deconvolution, the full width at half maximum (FWHM) was fixed at 0.2°, which is the same as that for the pristine LiCoO ₂ (003) peak in Figure 3.3.8.	109
Figure 3.3.11.	XRD pattern of Li _x CoO ₂ obtained by maintaining its voltage at 3 V (vs. Li/Li ⁺) for 12 h after 50 cycles of 4.6-V cycling (indicated as	

‘4.6 V cut: recovered’), which shows the recovery of its (003) peak broadness to that for 4.8-V cycling. 110

Figure 3.3.12. GITT measurements for Li/LiCoO₂ cell for (a) 4.6- and (b) 4.8-V cycling.111

Figure 3.3.13. Nyquist plots from *in situ* EIS measurement results for upper voltage limit of (d) 4.6 and (e) 4.8 V. For each semi-circle, the corresponding charge-transfer resistance (R_{ct}) value is shown. . 112

Figure 3.3.14. XPS results from O 1s spectra of (a) 4.6- and (b) 4.8-V-cycled LiCoO₂, which show both the outermost surface (0 nm) and etched surface (20 nm). In the legend, the oxygen atoms that form the chemical bonds corresponding to each de-convoluted XPS peak are highlighted in red in the molecular formula. 113

Figure 3.3.15. XPS spectra for Co 2p, F 1s, C 1s, and P 2p photoelectrons from (a) 4.6-V-cycled Li_xCoO₂ and (b) 4.8-V-cycled Li_xCoO₂. The spectra were obtained before and after Ar-ion etching, as indicated in the graph..... 114

Figure 3.3.16. (a) TEM image and (b) SAED pattern of pristine LiCoO₂ particle..... 115

Figure 3.3.17. (a) and (d) bright-field TEM images, (b) and (e) SAED patterns, and

(c) and (f), dark-field TEM images of LiCoO₂ particle obtained from electrochemically discharged electrode after 50 cycles of charge/discharge with upper voltage of 4.6 and 4.8 V, respectively. The position of the objective aperture for the dark-field image is indicated by the red circle in (b) and (e)..... 116

Figure 3.3.18. XRD pattern of 4.6- and 4.8-V-cycled LiCoO₂ discharged to 3.0 V (same result as **Figure 2a**) for entire 2θ measurement range (15°–70°)..... 117

Figure 3.3.19. (a) and (b) high-resolution TEM images of near-surface region of LiCoO₂ for upper voltage of 4.6 and 4.8 V, respectively. (c)–(f) fast Fourier transformation calculated from regions 1–4, respectively. 118

Figure 3.3.20. TEM images of the surface of (a and b) 4.6-V-cycled LiCoO₂ and (c and d) 4.8-V-cycled LiCoO₂ for other samples than those in **Figure 3.3.17**..... 119

Figure 3.3.21. Galvanostatic charge/discharge profiles when upper voltage cut-off was changed from 4.8 V for 100 cycles to 4.6 V..... 126

Figure 3.3.22. Nyquist plot obtained from EIS measurements by changing upper voltage cut-off (a) from 4.6 to 4.8 V and (b) from 4.8 to 4.6 V. The surface charge-transfer resistance R_{ct} values calculated from several

	representative semi-circles are denoted.....	127
Figure 3.3.23.	(a) TEM images of near-surface region of LiCoO ₂ after 4.8 V for 100 cycles → 4.6 V for 50 cycles. (band c) FFT calculations from region 1 and 2, respectively.	128
Figure 3.3.24.	Galvanostatic charge/discharge profiles when upper voltage cut-off was changed from 4.6 V for 100 cycles to 4.8 V	129
Figure 3.3.25.	(a) TEM images of near-surface region of LiCoO ₂ after 4.6 V for 100 cycles → 4.8 V for 50 cycles. (b and c) FFT calculations from region 1 and 2, respectively.	130
Figure 3.3.26.	(a) SEM image of the surface of AlPO ₄ -coated LiCoO ₂ . (b) Al 2p XPS spectra of AlPO ₄ -coated LiCoO ₂ (right) and bare LiCoO ₂ (left). The measurements were performed two times before and after Ar-ion milling for 30 s. (c–f) Comparison of cycle stability for 4.6- and 4.8-V-cut charge conditions after coating of AlPO ₄ onto bare LiCoO ₂ . (c) and (d) Galvanostatic charge/discharge profiles for upper voltage cut-offs of 4.6 and 4.8 V, respectively. (e) Discharge capacity and (f) energy efficiency change during electrochemical cycling.....	131
Figure 3.3.27.	A comparison among the normalized discharge capacity cycled at (a) 4.6-V cut-off and (b) 4.8-V cut-off potential.....	132

Figure 3.3.28. (a) XRD patterns of discharged non-coated and AlPO_4 -coated LiCoO_2 electrode 50 cycles of 4.8-V cycling. (b) The enlarged XRD pattern of **Figure 3.3.28a** for the region where the presence or absence of Co_3O_4 impurities in the cycled electrode can be well compared. 133

Figure 4.3.1. Schematic illustration of suggested in-situ gas-phase reaction method during synthesis of high-Ni NCM. 153

Figure 4.3.2. XRD patterns of synthesized NCM9163 powders for various reaction timing with SO_2 gas during annealing. 154

Figure 4.3.3. Effect of Li_2SO_4 on titration result by mixing LiOH , Li_2CO_3 , and Li_2SO_4 powder. (a) Titration curve of $\text{LiOH-Li}_2\text{CO}_3\text{-Li}_2\text{SO}_4$ mixture. Legend shows the volume of each powder-based aqueous solution (concentration of powder was fixed to 2500 ppm). (b) A summary of equivalent points (EPs) derived from titration curve at (a)..... 155

Figure 4.3.4. XRD patterns of synthesized NCM9163 powders for various reaction temperature with SO_2 gas during cooling step during annealing..... 156

- Figure 4.3.5.** Changing trend of various characteristic parameters (The amount of residual lithium and $I_{(003)}/I_{(104)}$ which is an indicator of quality of layered structure) of surface-modified NCM9163. 157
- Figure 4.3.6.** SEM images of (a and b) pristine NCM9163 particle and (c and d) surface-modified NCM9163 particle..... 165
- Figure 4.3.7.** Cross-sectional SEM image of (a and b) pristine NCM9163 particle and (c and d) surface-modified NCM9163 particle..... 166
- Figure 4.3.8.** TEM images of the surface of NCM9163 pristine powder: (a) Low-magnification image for NCM9163 showing Pt deposition layer used to protect NCM9163 powder during milling by focused-ion beam (FIB) of Ga^+ . (b and c) High-magnification image of image (a). (d) fast-fourier-transformation calculation result from square region indicated by red-dotted line in (c).. 167
- Figure 4.3.9.** TEM images of the surface of NCM9163 pristine powder: (a) Low-magnification image for SO_2 -treated NCM9163 showing Pt deposition layer used to protect NCM9163 powder during milling by focused-ion beam (FIB) of Ga^+ . (b and c) High-magnification image of image (a). (d) fast-fourier-transformation calculation result from square region indicated by red-dotted line in (c). 168
- Figure 4.3.10.** (a) STEM image of the surface region of NCM9163 pristine powder.

	STEM-EDS mapping result acquired from image in (a) for (b) Ni, (c) Pt, and (d) S.....	169
Figure 4.3.11.	(a) STEM image of the surface region of SO ₂ -treated NCM9163 pristine powder. STEM-EDS mapping result acquired from image in (a) for (b) Ni, (c) Pt, and (d) S	170
Figure 4.3.12.	XPS spectra of (a) Ni 2p, (b) S 2p, (c) O 1s core electron from the surface of NCM9163 powder (left-side panels) and SO ₂ -treated NCM9163 powder (right-side panels).	171
Figure 4.3.13.	ToF-SIMS spectra showing peaks for LiC ⁺ , LiOH ⁺ , Li ₂ O ⁺ , and Li ₂ OH ⁺ on NCM9163 and SO ₂ -treated NCM9163. Intensity was normalized by the total ion density.....	172
Figure 4.3.14.	Voltage profile of Li/NCM9163 half-cell.....	173
Figure 4.3.15.	Voltage profile of Li/(SO ₂ -treated-NCM9163) half-cell.....	174
Figure 4.3.16.	XRD patterns of NCM9163 reacted with diluted O ₂ /SO ₂ (5%) mixture gas with various flow rate.	179
Figure 4.3.17.	Voltage profile of Li/ (O ₂ /SO ₂ (5%)-treated NCM9163) half-cell after surface treatment method was optimized.	180

Figure 4.3.18. Cycle stability test result of Li/(O ₂ /SO ₂ (5%)-treated NCM9163) powder whose surface modification condition was optimized compared with Li/(pristine NCM9163) cell.	181
Figure 4.3.19. <i>In-situ</i> gas analysis result during charge process of the (a) Li/NCM9163 cell and (b) Li/ (O ₂ /SO ₂ (5%)-treated NCM9163) cell by DEMS.	182
Figure 4.3.20. BJH pore size distribution plot and BET surface area of pristine NCM9163, SO ₂ -treated and O ₂ /SO ₂ (5 %) -treated NCM9163 powder.	183
Figure 4.3.21. Photographs of slurry of (a) mixture of super-P carbon, PVDF binder and NMP solvent and (b) NCM9163 pristine powder mixed with slurry in (a), and (c) O ₂ /SO ₂ (5%)-treated NCM9163 powder mixed with slurry in (a).	184

Chapter 1. Introduction

1.1. Lithium rechargeable batteries for large-scale energy storage

Globally raised environmental issues such as greenhouse effect and climate change from the emission of CO₂ gas from fossil fuel have been mainly caused by ever-increasing energy demand of humanity. Nevertheless, this demand is rather being augmented much faster than before due to unprecedented explosive global population growth and increasing access to energy in the developing countries¹⁻⁴. To cope with both of two needs, mitigating environmental problem and meeting increasing energy demands, energy generation from renewable energy sources such as seawater, wind, and solar, has now become an inevitable choice. However, attempts to apply this kind of energy to the electrical power grid or conventional passenger vehicles have encountered significant obstacles due to their intrinsic limitation come from intermittent and dispersed supply^{1, 3}. For example, this can render peak energy supply hour of the renewable source and peak demand time of electricity not consistent⁴, which led to the requirement of corresponding efficient large-scale energy storage systems (ESSs). Up to now, pumped hydroelectric storage and compressed air storage have accounted for the most of worldwide energy storage capacity due to their cost-effective and technologically mature characteristics^{4, 5}. In this circumstances, due to superior energy and power characteristics, CO₂-free operation, low maintenance, and long cycle life, lithium rechargeable batteries which already adapted broadly into portable storage system emerged as a new alternative

to conventional systems nowadays^{1, 3-5}. Their design and size flexibility make them suitable for use at distributed locations and application in the electric power grid to prevent the massive power outage⁵, and in addition, lithium battery already opened a new era of EVs and made its market share larger than consumer electronics recently⁶⁻⁸.

Although lithium rechargeable batteries are currently prevailing in the electronics market and have thus been optimized for that purpose, these large-scale applications present new challenges for batteries that are distinct from those of consumer electronics. First, cost per energy and power capacity of lithium rechargeable batteries is too expensive to be substituted for conventional ESS and combustion engine in passenger vehicles. Recently, it was reported that the cost of discharged electrical energy for current lithium battery-based ESS (\$0.14/kWh) is about four times of that for conventional ESS (\$0.035/kWh) in case of daily cycling (**Figure 1.1.1**)⁴. For this issue, increasing the energy density of lithium batteries by widening operation range or adapting new active material can be a fundamental solution. In addition, the energy density of lithium rechargeable battery is also essential for EV technology because it is related to driving mileage of EVs^{6, 7, 9, 10}. Still, the most affordable EVs currently provide a shorter driving range than that offered by conventional engines^{11, 12}, which creates a high demand for lithium rechargeable batteries with even higher energy density. Second, one of the main differences for large-scale operation environments is that the batteries may be exposed to temperatures far below (in winter) or above (in summer) room temperature for an extended period. Moreover, the batteries would mostly be in a rest state at certain SOCs without being used for long periods. These conditions are quite dissimilar from those expected for the typical use of consumer electronics, which are mostly at room temperature and under constant operation. To address this

issue, preventing the unwanted situations in batteries based on fundamental understanding is crucial.

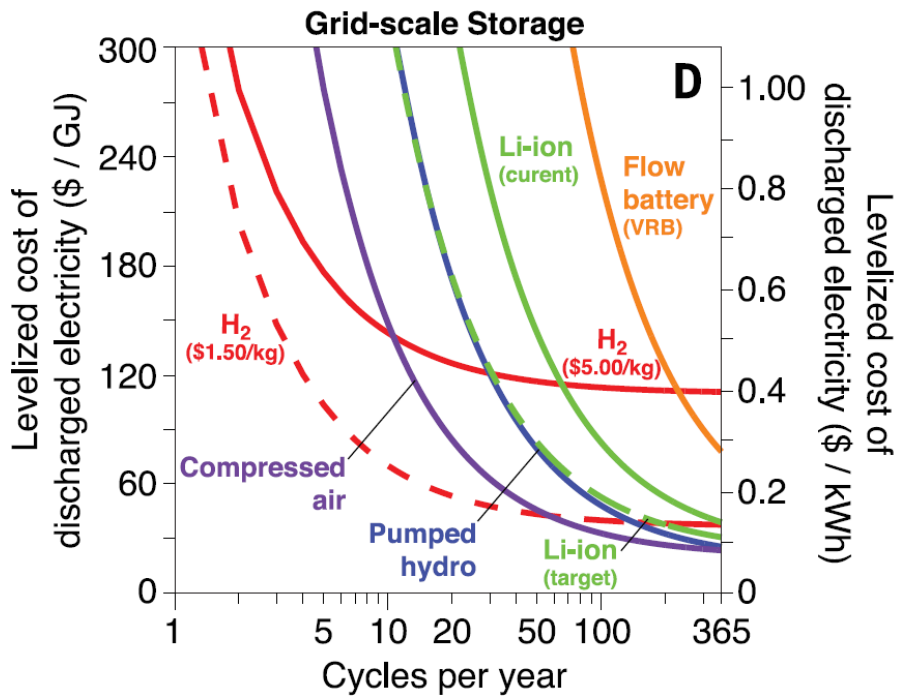


Figure 1.1.1. Comparison of the cost for discharged electrical energy as a function of cycling frequency. Reprinted with permission from ref 4. (Copyright 2018, AAAS)

1.2. Barriers of obtaining lithium batteries with high energy density

One of the main reason why lithium batteries dominate over other types of rechargeable batteries such as lead-acid cells, nickel-cadmium cells, and nickel-metal hydride is its highest energy density (**Figure 1.2.1.**)^{13, 14}. The Energy density (specific energy) of a battery is defined as the stored amount of electrical energy capacity per unit volume or mass of a material or a device:

$$\text{Energy density (W h kg}^{-1}\text{)} = \text{Specific capacity (A h kg}^{-1}\text{)} \times \text{Average potential (V)}$$

Normally, the overall energy density of lithium battery is determined by the energy density of cathode^{9, 12-16}. Considering that energy density is a product of the cell voltage and specific capacity as shown in the equation above, it's because of much lower specific capacity of cathode than that of anode in addition to average potential of cathode that has made trouble in widening the overall energy density of batteries. As shown in **Table 1.2.1**, even the specific capacity of commercialized graphite anode (372 mAh g⁻¹) exceeds that of the most of cathode materials which is currently being either industrially or academically investigated. This simply means that the best solution to address this energy density issue is to develop cathode materials with high specific capacity and high average potential.

To develop cathode materials with high energy density, a variety of new type of materials was nominated for the component of next-generation lithium rechargeable batteries (**Table 1.2.2**). First, various layered-type transition metal oxides such as high-Ni LiNi_xMn_yCo_{1-x-y}O₂ and Li-rich layered oxides have been explored^{12, 15, 17, 18} and implemented in state-of-the-art LIBs. Second, cathode materials with other crystal structure than conventional layered structure such as

olivine, spinel, fluorosulfate and pyrophosphate have been also investigated^{10, 19, 20}. Theoretically, these materials are expected to show higher energy density than conventional counterparts due to their even higher average potential reaching ~5 volts. However, deploying these materials in ESSs and EVs is still far from accomplishment due to various problems including inferior cycle stability and safety issue. For instance, high-nickel (>80%) $\text{LiNi}_x\text{Mn}_y\text{Co}_{1-x-y}\text{O}_2$ layered oxides suffer from its chemically unstable surface to generate LiOH and Li_2CO_3 compounds known as ‘residual lithium’, which react electrolyte vigorously to promote the gas evolution^{12, 17, 18}. Also anisotropic volume expansion nature of it during electrochemical cycling induces the propagation of microcrack, forming fresh contact with the electrolyte to consume a large amount of electrolyte by making new interface film accompanying the increase of polarization of whole battery^{12, 17, 18}. $\text{LiNi}_{0.5}\text{Mn}_{1.5}\text{O}_4$, so-called ‘High-voltage spinel’ possesses advantages of excellent rate capability, lower cost, and higher safety to attract emerging interests from battery society. However, the high average potential of it rather deteriorates its cycle stability owing to aggressive side reactions at the interface with an electrolyte which in turn rapidly consumes the electrolyte in a commercialized cell which contains a limited amount of it^{10, 21}. Also, transition metal dissolution issue becomes significant by a severe side reaction with electrolyte¹⁰. Similarly, other cathode candidates all are facing these types of interfacial side reaction problems with electrolyte due to high-voltage operation although the extent of it is different from each other and requires suitable electrode-electrolyte pairs.

In natural, developing high-energy-density cathode materials would include the simplest way: increasing both of specific capacity and operating potential by widening the operation range of conventional cathode materials. For example, LiCoO_2 , the canonical cathode material adopted in commercialized lithium-ion

batteries (LIBs) has been restricted its reversible state-of-charge (SOC) range to ~ 0.5 Li^{22, 23}. However, as shown by its voltage profile (**Figure 1.2.2**)²⁴, if reversible SOC range is extended to a maximum of 1.0, its charge voltage reaching ~ 5.2 V and specific capacity of 274 mA h g^{-1} would make it desired high-energy-density cathode material to be selected for state-of-art EVs and ESSs. Nevertheless, until now there was a limited success in widening the working SOC window by modifying the surface of this material. In this case, also the side reaction of electrolyte generating various interfacial problem^{22, 23} has been indicated as the most essential issue to be overcome. Although there are many ways suggested for obtaining high-energy-density cathode materials, interfacial issues rather than issues from material characteristics have been the main obstacle for their commercialization.

Anode material	Average potential (V vs. Li/Li⁺)	Theoretical capacity (mA h g⁻¹)
Li ₄ Ti ₅ O ₁₂	1.5-1.6	175
C ₆ (graphite)	0.1-0.2	372
Sn	0.6-0.8	960
Si	0.1-0.3	3579
Li	0	3860

Cathode material	Average potential (V vs. Li/Li⁺)	Theoretical/practical capacity (mA h g⁻¹)
LiMn ₂ O ₄	4.1	148/120
LiCoO ₂	3.9	274/150
LiNi _{0.33} Co _{0.33} Mn _{0.33} O ₂	3.7	280/160
LiFePO ₄	3.4	170/165
LiNi _{0.8} Co _{0.15} Al _{0.05} O ₂	3.7	280/200

Table 1.2.1. Characteristics of representative conventional cathode and anode materials for lithium rechargeable batteries; average potentials and theoretical/practical capacity^{6, 10, 19, 20 25}.

Cathode material	Average potential (V vs. Li/Li ⁺)	Theoretical/rev-ersible capacity* (mA h g ⁻¹)
LiNi _x Co _y Mn _z O ₂ (x≥0.8)	3.7	270-280/>200
Li- and Mn-rich layered (xLi ₂ MnO ₃ ·(1-x)LiMO ₂ (M=Ni, Mn, Co))	3.6-3.7	≥200
LiNi _{0.5} Mn _{1.5} O ₄	4.7	148/140
LiCoPO ₄	4.8	167/>120
LiNiPO ₄	5.1	169/>75
LiFeSO ₄ F (triplite)	3.9	151/130
Li ₂ CoP ₂ O ₇	5.0	109/90

* Because the properties of those materials are not considered to be adequate for test in practical use, a term of reversible capacity, not the ‘practical capacity’ was used.

Table 1.2.2. Characteristics of various representative cathode and materials with high average potential or specific capacity for lithium rechargeable batteries^{10, 15, 20,}

25.

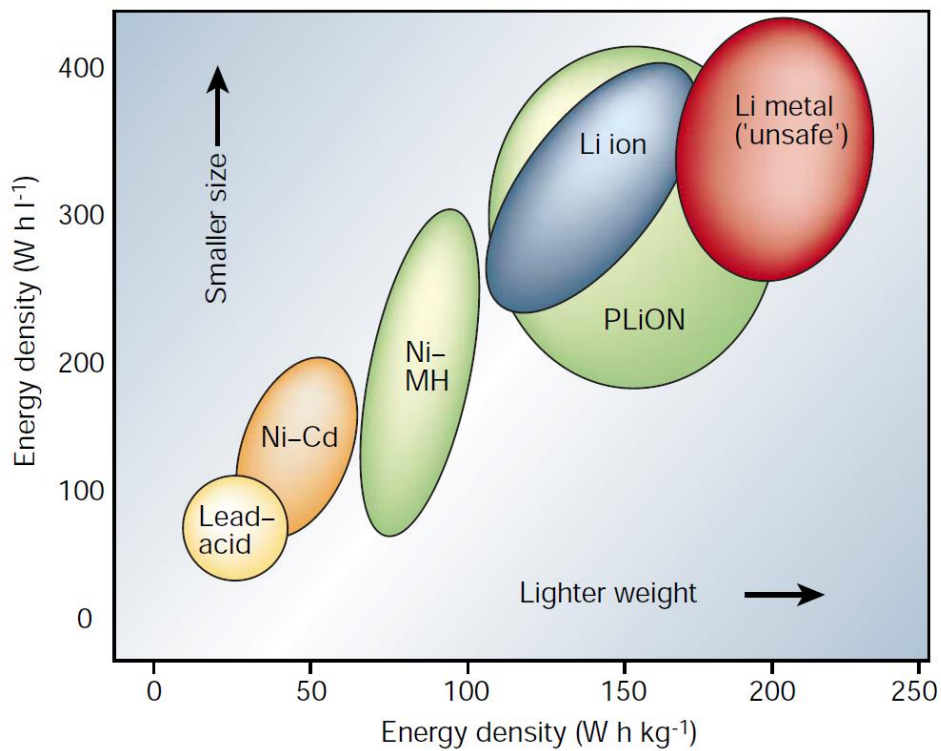


Figure 1.2.1. Summary of characteristics of various electrochemical rechargeable batteries. Reprinted by permission from Springer Nature, *Nature*, ref 13, Copyright 2001.

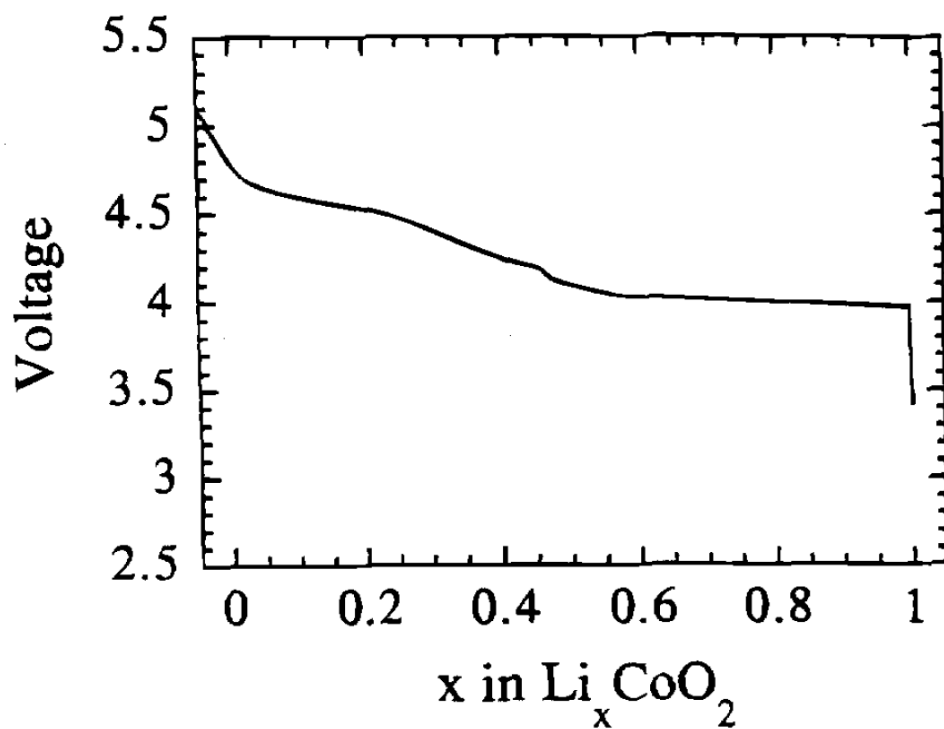


Figure 1.2.2. Representative voltage profile of Li_xCoO_2 by extracting lithium electrochemically. From ref 24. Reproduced with permission of Electrochemical Society, Copyright 1996.

1.3. Interfacial dynamics between cathode and electrolyte in lithium batteries

As mentioned in previous chapters, high-energy-density cathode materials suffer from side reactions at the interface with electrolyte. Therefore, controlling these side reactions based on an understanding of interfacial dynamics between cathode and electrolyte can lead to the new opportunity of utilizing cathode materials already being investigated. A significance of interfacial dynamics between electrode and electrolyte can be easily noted by the revolutionary triumph of adopting graphite anode in commercializing lithium-ion batteries (LIBs). Choosing graphite for anode material in lithium-ion batteries was possible due to the formation of uniform and compact solid electrolyte interphase (SEI) layers on it^{10, 21, 26}. Owing to this stable SEI layer, additional electrolyte reduction reaction at graphite surface and lithium consumption during cycling was effectively blocked to ensure high coulombic efficiency, superior cycle stability and safety of LIBs^{10, 21}. Although lithium metal with much higher energy density (see **Table 1.2.1**) was investigated as candidate for anode of commercialized cell previously, non-uniform nature of SEI layer on lithium metal induced non-uniform deposition of lithium and in turn, well-known lithium dendrite growth occurs to make safety issue and commercialization of LIBs were delayed until the application of graphite anode^{10, 21, 27}. Very recently, a success of the reversible operation of 5-Volt-class Li/LiCoPO₄ cell whose utilization has been limited with currently commercialized electrolyte has reported by adopting new non-flammable electrolyte (**Figure 1.3.1**)²⁸. These examples imply that the development of proper electrode-electrolyte pair is as important as that of new electrode material itself.

The formation of SEI layer on the anode is based on thermodynamically unstable nature of aprotic solvent of an electrolyte such as ethylene carbonate (EC) and polyethylene carbonate (PC) under the reductive environment at near 0 volts (*vs.* Li/Li⁺)^{29, 30}. This thermodynamic feature can be easily understood by a stability window of the electrolyte (**Figure 1.3.2**)²¹. When the potential of the anode reaches almost 0 volts during the first charge of a battery, Fermi level of anode became higher than that of lowest unoccupied molecular orbital (LUMO) level of electrolyte, and have a driving force to donate electrons to electrolyte solvent. In contrast, there is no thermodynamic driving force in cathode material to oxidize aprotic electrolyte solvent at the potential of cathode >6.0 V (*vs.* Li/Li⁺). This makes big discrepancy between finding on a film formed by an oxidation reaction of electrolyte solvent on the conventional cathode materials and its much lower operational potential range than that thermodynamic driving force of electro-oxidation of electrolyte solvent exists³¹⁻³³. In addition, it has been revealed that the composition of a film on the cathode is similar with that on anode formed at reductive environment (**Figure 1.3.3**)^{33, 34}. A number of research groups have tried to explain the origin of the formation of cathode electrolyte interface (CEI) film, but there are still a lack of understanding on the interfacial dynamics between cathode and electrolyte due to scarce thorough studies on this issue. This led to currently limited fundamental knowledge on the deleterious effect of side reaction at CEI to cathode material and thus to overall battery performance. Following chapters are about current understandings on interfacial phenomena degrading the overall performance of battery, which are the basis of my following researches on fundamental study on cathode-electrolyte interfacial dynamics.

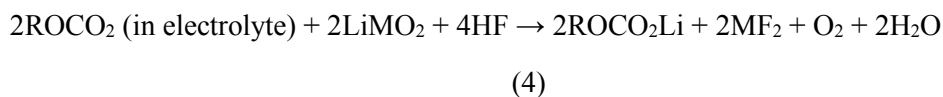
1.3.1. Surface reconstruction of cathode material

During the formation of CEI film by side reaction at the interface between cathode and electrolyte, the active material itself can be deteriorated by change or distortion of its crystal structure accompanying the reduction of transition metal oxidation state, which is so-called surface reconstruction. Normally this phenomenon has demonstrated as spinel or spinel-like phase formation at the region nearby the surface of layered transition metal oxide material^{10, 21}. The origin of the surface reconstruction is still not clear and under debating, but triggering reaction is oxidation reaction of electrolyte to transfer an electron to cathode surface whether the reaction is electrochemical or chemical. For example, it has reported that just an immersion of cathode material in the electrolyte can induce surface reconstruction by reducing Co^{3+} to Co^{2+} at the surface of LiCoO_2 ³⁵. The beginning of charge after then generates spinel-like phase at the surface. Furthermore, in another report, the surface of layered $\text{LiNi}_x\text{Co}_y\text{Mn}_z\text{O}_2$ transforms from layered ($R-3m$) into spinel ($Fm-3m$) first, and then to rock-salt phase ($Fm-3m$) such as NiO (**Figure 1.3.4**) by electrochemical cycling³⁶. Because these transformed phases do not have lithium storage property in the conventional operating potential range of cathode (>3.0 V vs. Li/Li^+), they act as an ionically resistive surface film to degrade the overall performance of a battery.

This surface reconstruction process seems to be closely related with CEI dynamics as shown in the following example of CEI film formation derived by LiPF_6 salt decomposition. Thermally-activated decomposition reaction of LiPF_6 salt occurs from 107 °C³⁷. Generally, the decomposition proceeds as shown by the following equations^{37, 38}:



With only a trace amount of water in the electrolyte, HF can be formed and triggers a series of reactions ³⁹⁻⁴¹:



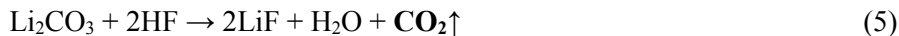
Equation (3) involves the degradation of layered structure other types of crystal structure which can be regarded as reconstruction reaction. Other than the equations above, it has been known that the decomposition of LiPF_6 salt directly results in well-known phosphorus oxides such as $\text{Li}_x\text{PF}_y\text{O}_z$ and organophosphates ($\text{OP}(\text{OR})_3$) reported as components of CEI film ⁴⁰.

In addition, ring-opening reaction of the solvent molecule by the nucleophilic attack as well as salt decomposition reaction can trigger the surface reconstruction (**Figure 1.3.5**)^{21, 42}. By this reaction, solvent molecule newly forms a chemical bond with oxygen ion at the surface of cathode material and share electrons with each other. The rate of this reaction becomes greater as nucleophilicity (or Lewis basicity) of the oxygen at the surface increases, and this is why higher nucleophilicity of oxygen in $\text{Li}_{1-x}\text{NiO}_2$ is being considered to be a reason of higher surface impedance after cycling than that of $\text{Li}_{1-x}\text{CoO}_2$ ²¹. As mentioned above, strategy for mitigating surface reconstruction should not consider only cathode material itself, but also the combined effect of the pairing of electrolyte and cathode material, which makes the fundamental understanding on this phenomenon much

more complex.

1.3.2. Gas evolution by side reaction of CEI film or during CEI film formation

Another notorious phenomenon which occurs by side reaction between cathode and electrolyte is a gas evolution during battery operation. For example, Li_2O and Li_2CO_3 which consist of CEI film on the surface of cathode material can generate CO_2 or CO gas when LiPF_6 salt is used in the electrolyte as follows⁴³⁻⁴⁵:



LiOH and Li_2CO_3 species is also well-known residual lithium compound at the surface of high-Ni $\text{LiNi}_x\text{Co}_y\text{Mn}_z\text{O}_2$ layered transition metal oxide^{12, 17, 18}. This is why gas evolution issue has been of great interest from the industrial point of view. In addition to CO_2 and CO gas, O_2 gas release by side reaction at the interface between cathode and electrolyte. Normally the amount of oxygen gas release is not as much as that of CO_2 gas^{46, 47}, the effect of O_2 gas is much more detrimental in that it can directly cause the battery explosion by small ignition and also be a reason of surface reconstruction⁴⁷. During battery charging, it has been proved by previous reports that surface oxygen also participate in a redox reaction to be partly oxidized

into super- (O_2^-) or peroxides (O_2^{2-})^{48,49}. Those species are strongly reactive toward organic carbonate electrolyte to make CEI films, and it has been speculated that peroxide anions reacts further to generate oxygen gas (**Figure 1.3.6**)⁵⁰. As shown in **Figure 1.3.6**, a greater amount of oxygen gas will be generated when SOC of the cathode is increased because the redox reaction occurs more vigorously at high SOC level (**Figure 1.3.7**)⁵¹. Still, the detailed mechanism of oxygen evolution at the surface of cathode materials is not clear, and needs to be studied further. Besides, this oxygen evolution reaction inevitably induces the surface reconstruction because of the loss of lattice oxygen in the crystal structure. In terms of the atomic ratio between transition metal and oxygen, it should be 1:2 in conventional layered structure, but oxygen loss from lattice can make spinel (1:1.33) or rock-salt (1:1) more favorable. Therefore, it can be inferred that gas evolution from side reaction at CEI causes not only the safety issue and the consumption of electrolyte, but also the degradation of the cathode material to deteriorate the overall battery performance. Applying this fact to the relationship between oxygen gas evolution and SOC in **Figure 1.3.7** easily lead to a conclusion that, battery cycling in wide SOC range would trigger the severe degradation of the cathode material.

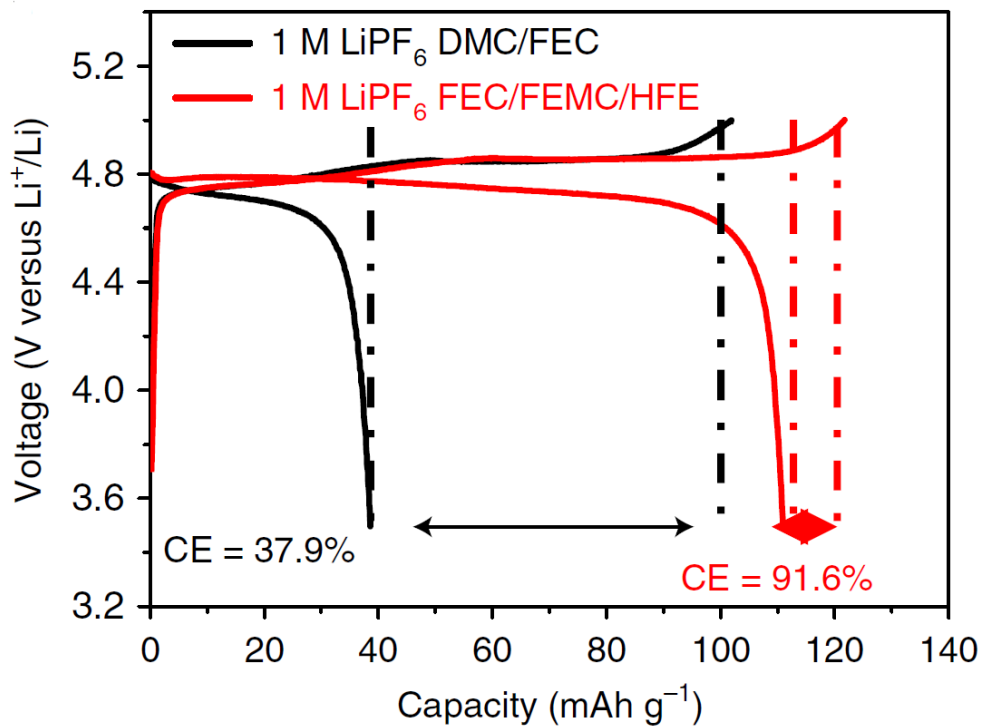


Figure 1.3.1. A comparison of voltage profile of Li/LiCoPO₄ cell adopting conventional carbonate-based electrolyte (black line) and newly developed electrolyte (red line). Reprinted by permission from Springer Nature, *Nature nanotechnology*, ref 18, Copyright 2018.

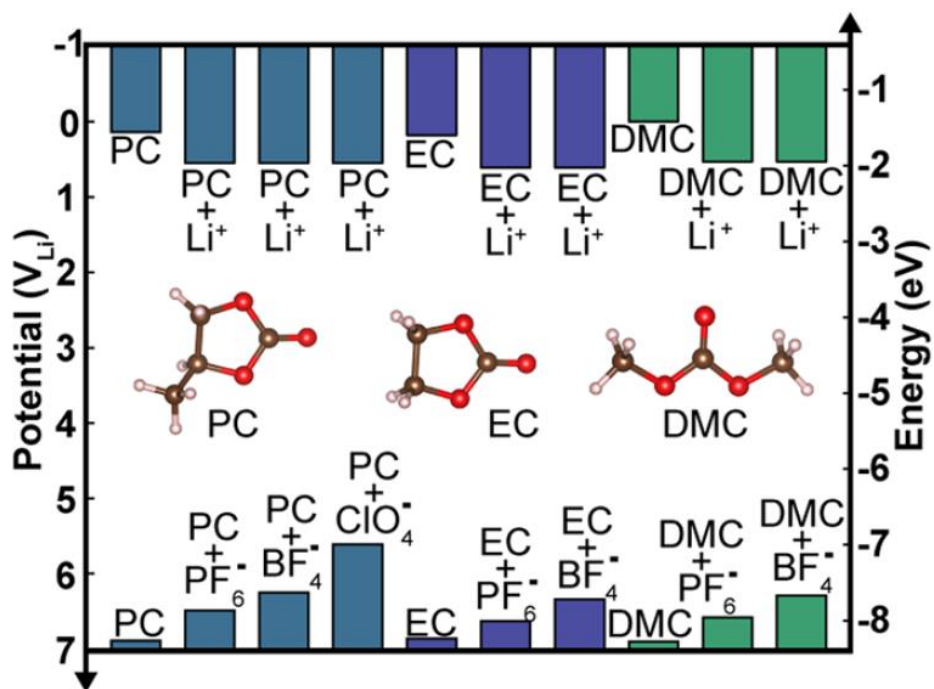


Figure 1.3.2. Computation result of reduction and oxidation energy levels of broadly known lithium rechargeable battery electrolyte solvents and solvated salts. Reprinted with permission from ref 21. Copyright 2015 American Chemical Society.

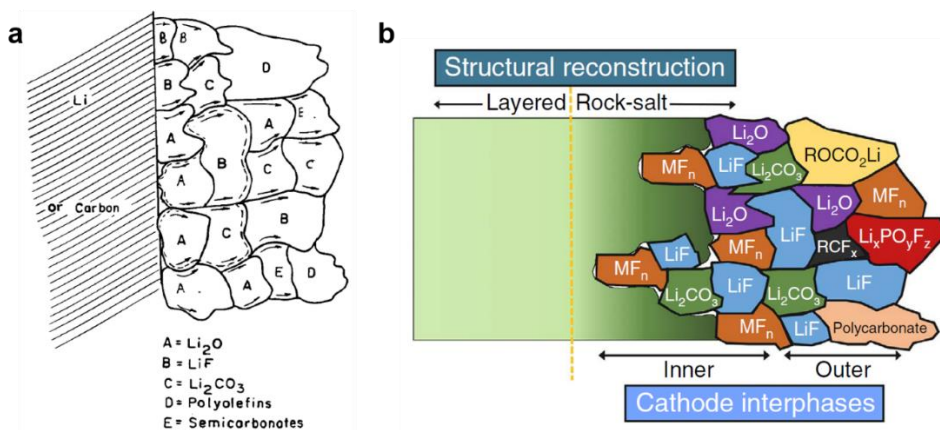


Figure 1.3.3. Current understanding on the composition and distribution of the (a) SEI on anodes and (b) CEI on cathodes in lithium rechargeable batteries. From ref 34. Reproduced with permission of Electrochemical Society, Copyright 1997. For Figure 1.3.3b, this work is licensed under the Creative Commons Attribution 4.0 International License. To view a copy of this license, visit <http://creativecommons.org/licenses/by/4.0/> or send a letter to Creative Commons, PO Box 1866, Mountain View, CA 94042, USA.

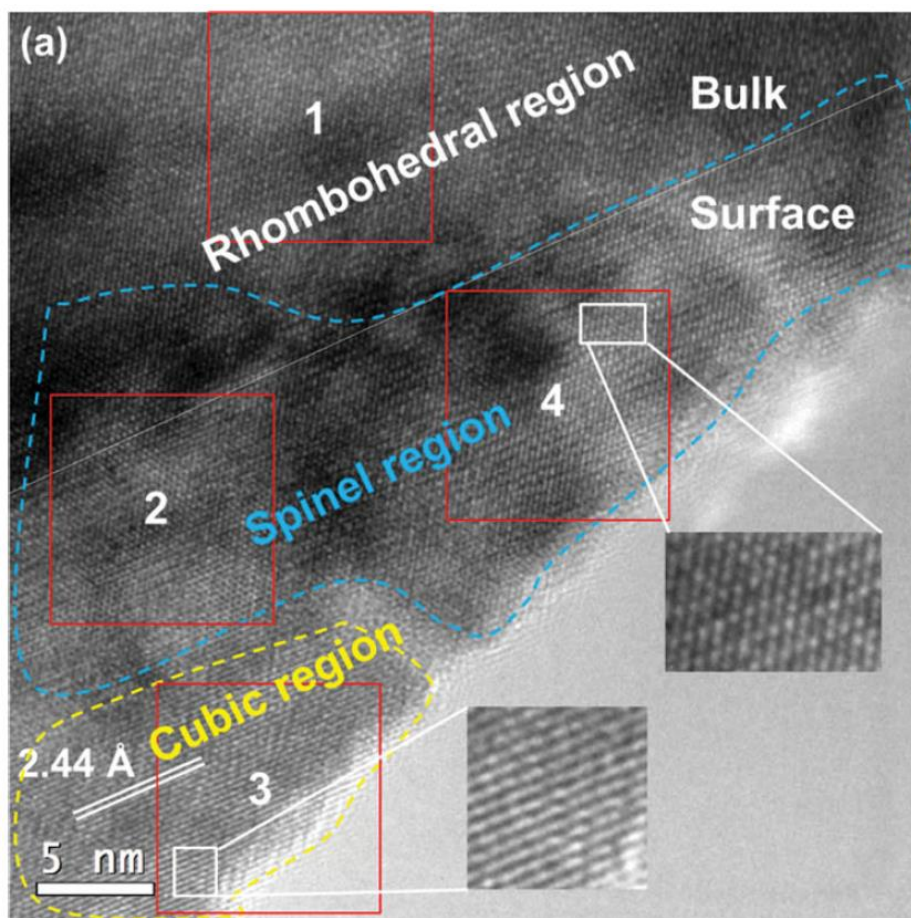


Figure 1.3.4. Surface reconstruction of $\text{LiNi}_{0.5}\text{Co}_{0.2}\text{Mn}_{0.3}\text{O}_2$ surface after 50 cycles under 3.0-4.5 V (vs. Li/Li^+) conditions observed by high-resolution transmission electron microscope (HR-TEM). Reprinted with permission from ref 36. Copyright 2014, Wiley-VCH.

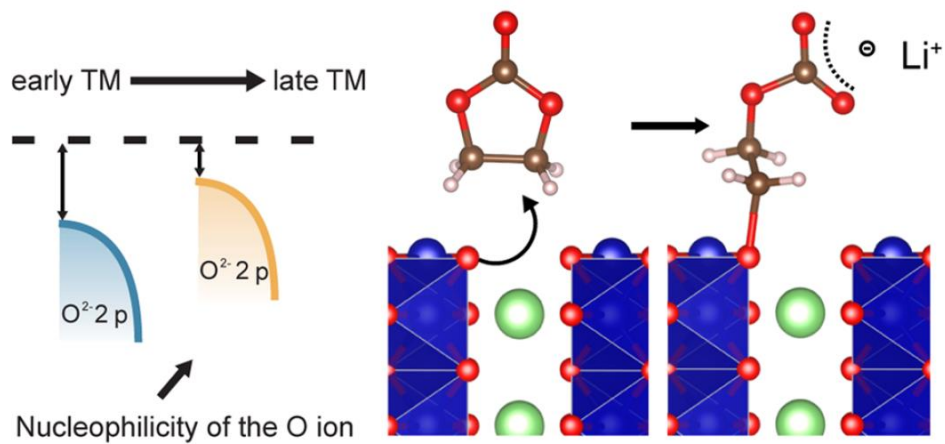


Figure 1.3.5. Schematic illustration of nucleophilic attack of aprotic electrolyte solvents. Reprinted with permission from ref 21. Copyright 2015 American Chemical Society.

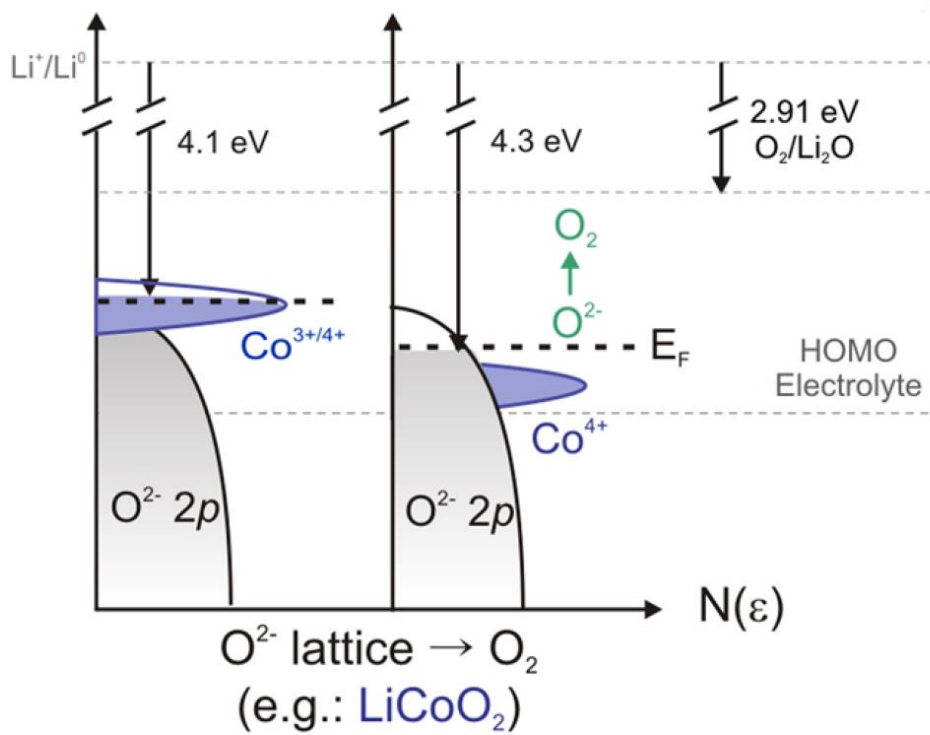


Figure 1.3.6. Schematic illustration of oxygen evolution from LiCoO_2 by electronic structure of it. Reprinted with permission from ref 21. Copyright 2015 American Chemical Society.

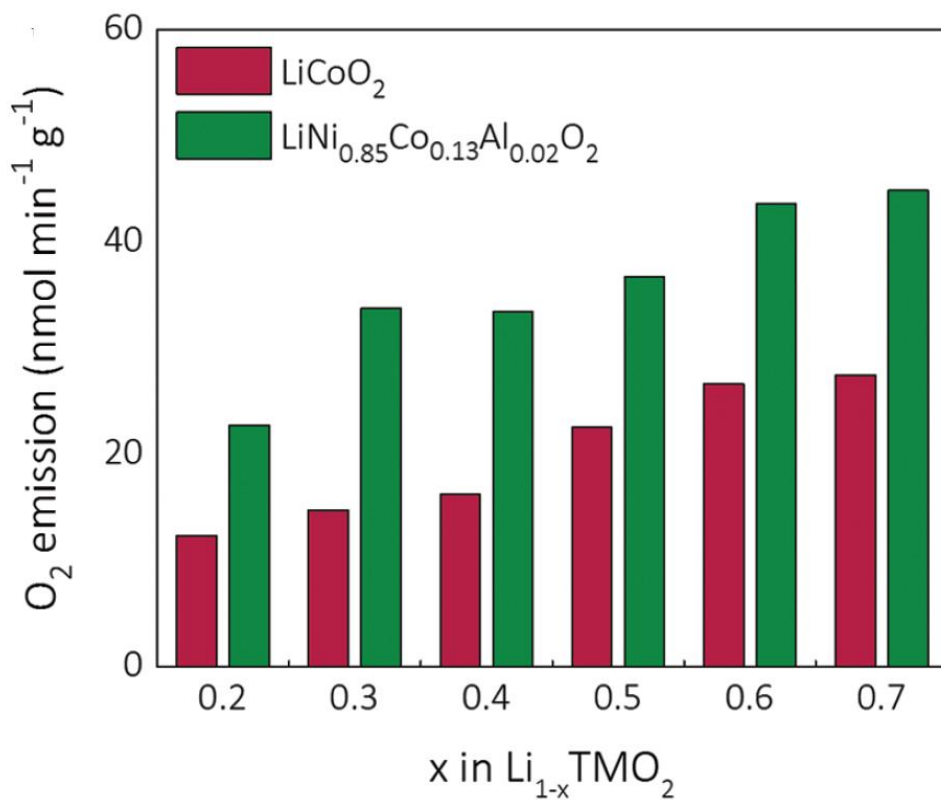


Figure 1.3.7. Oxygen evolution rate as a function of SOC of representative lithium transition metal oxide cathodes. Reprinted with permission from ref 51. Copyright 2017, Wiley-VCH.

1.4. Purpose of this thesis

Aforementioned, the development of lithium rechargeable batteries with high energy density is crucial for successful adoption to ESSs and EVs. To reach high enough energy density, fundamental understanding of interfacial dynamics between cathode and electrolyte is now essential and can make a breakthrough in current battery technology. It is because of much harsher condition such as high temperature and operating voltage, which can induce more serious interfacial problems, that battery should tolerate for future use. However, the research on this field requires an interdisciplinary approach including a cathode, electrolyte (both of solvent and salt), and even the pairing effect of cathode and electrolyte. Furthermore, contribution of various components at the same time for interfacial behaviors makes the decoupling of each contribution difficult. This is why there is still only a little thorough research on this field in spite of the importance of the fundamental understanding of it. In this thesis, I performed a series of fundamental researches on the interfacial behavior between cathode and electrolyte to extract an inspiration for developing high-energy-density cathodes.

First, fundamental studies on interfacial degradation phenomenon at CEI at high temperature condition have been conducted. It occurred as intimate interplay of electrolyte salt and cathode surface generating other type of crystal structure. This phenomenon is closely related with acceleration of self-discharge of lithium battery even after cooling, which has been neglected due to its intrinsic low self-discharge rate enabling its market-dominator position. I call it as thermal history-driven abnormal self-discharge in lithium batteries.

Second, a new type of strategy to control the surface reconstruction at the cathode surface at extremely high voltage condition was reported. Even if transition

metal dissolution has been known as notorious effect for cathode material, it acted here rather beneficial role at extremely high potential by removing resistive spinel-like surface reconstruction layer. Validity of this strategy has proved by superior cycle stability of Li/LiCoO₂ cell at 4.8 V cut-off compared with cycle stability at 4.6 V cut-off. I call this strategy as subtractive surface modification method, as a counterpart of common additive surface modification such as a coating of alien materials.

Finally, an effective method to suppress the notorious interfacial behavior has reported. Herein, a way of controlling residual lithium chemistry by a simple *in-situ* gas-phase reaction during the synthesis of high-Ni LiNi_xCo_yMn_zO₂ was suggested. Injection of reactive gas for only short duration made a protective thin-film on this material. The gelation of cathode slurry during battery preparation and vigorous gas evolution during battery operation by residual lithium has blocked the commercialization of high-Ni layered oxide. However, by this new strategy, all of these troubles were successfully resolved with ruling out the needs on post-treatment which can cause production cost issue.

As a result, this series of researches on fundamental understandings of interfacial dynamics at CEI was successful to suggest new phenomenon and strategies for mitigating problems which have never been considered before. This indicates again that, fundamental understanding of this unattended field can make a breakthrough for lithium battery technology. It is expected that this thesis will be a good example for engineers and scientists who are finding new ways to address the issues generated at interface between cathode and electrolyte to fabricate lithium batteries with high energy density adaptable in ESSs and EVs.

1.5. Reference

1. Larcher, D.; Tarascon, J. M. *Nat. Chem.* **2014**, 7, 19.
2. Obama, B. *Science* **2017**.
3. Chu, S.; Cui, Y.; Liu, N. *Nat. Mater.* **2016**, 16, 16.
4. Davis, S. J.; Lewis, N. S.; Shaner, M.; Aggarwal, S.; Arent, D.; Azevedo, I. L.; Benson, S. M.; Bradley, T.; Brouwer, J.; Chiang, Y.-M.; Clack, C. T. M.; Cohen, A.; Doig, S.; Edmonds, J.; Fennell, P.; Field, C. B.; Hannegan, B.; Hodge, B.-M.; Hoffert, M. I.; Ingersoll, E.; Jaramillo, P.; Lackner, K. S.; Mach, K. J.; Mastrandrea, M.; Ogden, J.; Peterson, P. F.; Sanchez, D. L.; Sperling, D.; Stagner, J.; Trancik, J. E.; Yang, C.-J.; Caldeira, K. *Science* **2018**, 360, (6396).
5. Dunn, B.; Kamath, H.; Tarascon, J.-M. *Science* **2011**, 334, (6058), 928-935.
6. Berckmans, G.; Messagie, M.; Smekens, J.; Omar, N.; Vanhaverbeke, L.; Van Mierlo, J. *Energies* **2017**, 10, (9), 1314.
7. Yang, F.; Xie, Y.; Deng, Y.; Yuan, C. *Nat. Commun.* **2018**, 9, (1), 2429.
8. Kwade, A.; Haselrieder, W.; Leithoff, R.; Modlinger, A.; Dietrich, F.; Droeder, K. *Nat. Energy* **2018**, 3, (4), 290-300.
9. Choi, J. W.; Aurbach, D. *Nature Reviews Materials* **2016**, 1, 16013.
10. Li, W.; Song, B.; Manthiram, A. *Chem. Soc. Rev.* **2017**, 46, (10), 3006-3059.
11. Kempton, W. *Nat. Energy* **2016**, 1, 16131.
12. Myung, S.-T.; Maglia, F.; Park, K.-J.; Yoon, C. S.; Lamp, P.; Kim, S.-J.; Sun, Y.-K. *ACS Energy Lett.* **2017**, 2, (1), 196-223.
13. Tarascon, J. M.; Armand, M. *Nature* **2001**, 414, 359.
14. Armand, M.; Tarascon, J. M. *Nature* **2008**, 451, 652.
15. Nayak, P. K.; Erickson, E. M.; Schipper, F.; Penki, T. R.; Munichandraiah,

- N.; Adelhalm, P.; Sclar, H.; Amalraj, F.; Markovsky, B.; Aurbach, D. *Adv. Energy Mater.* **2018**, 8, (8), 1702397.
16. Susai, F. A.; Sclar, H.; Shilina, Y.; Penki, T. R.; Raman, R.; Maddukuri, S.; Maiti, S.; Halalay, I. C.; Luski, S.; Markovsky, B.; Aurbach, D. *Adv. Mater.* **2018**, 30, (41), 1801348.
17. Liu, W.; Oh, P.; Liu, X.; Lee, M.-J.; Cho, W.; Chae, S.; Kim, Y.; Cho, J. *Angew. Chem. Int. Ed.* **2015**, 54, (15), 4440-4457.
18. Kim, J.; Lee, H.; Cha, H.; Yoon, M.; Park, M.; Cho, J. *Adv. Energy Mater.* **2018**, 8, (6), 1702028.
19. Kraytsberg, A.; Ein-Eli, Y. *Adv. Energy Mater.* **2012**, 2, (8), 922-939.
20. Nitta, N.; Wu, F.; Lee, J. T.; Yushin, G. *Materials Today* **2015**, 18, (5), 252-264.
21. Gauthier, M.; Carney, T. J.; Grimaud, A.; Giordano, L.; Pour, N.; Chang, H.-H.; Fenning, D. P.; Lux, S. F.; Paschos, O.; Bauer, C.; Maglia, F.; Lupart, S.; Lamp, P.; Shao-Horn, Y. *The Journal of Physical Chemistry Letters* **2015**, 6, (22), 4653-4672.
22. Kalluri, S.; Yoon, M.; Jo, M.; Liu, H. K.; Dou, S. X.; Cho, J.; Guo, Z. *Adv. Mater.* **2017**, 29, (48), 1605807.
23. Wang, L.; Chen, B.; Ma, J.; Cui, G.; Chen, L. *Chem. Soc. Rev.* **2018**, 47, (17), 6505-6602.
24. Amatucci, G. G.; Tarascon, J. M.; Klein, L. C. *J. Electrochem. Soc.* **1996**, 143, (3), 1114-1123.
25. Howard, W. F.; Spotnitz, R. M. *J. Power Sources* **2007**, 165, (2), 887-891.
26. Aurbach, D.; Ein-Eli, Y.; Markovsky, B.; Zaban, A.; Luski, S.; Carmeli, Y.; Yamin, H. *J. Electrochem. Soc.* **1995**, 142, (9), 2882-2890.
27. Aurbach, D.; Zaban, A.; Schechter, A.; Ein-Eli, Y.; Zinigrad, E.;

- Markovsky, B. *J. Electrochem. Soc.* **1995**, 142, (9), 2873-2882.
28. Fan, X.; Chen, L.; Borodin, O.; Ji, X.; Chen, J.; Hou, S.; Deng, T.; Zheng, J.; Yang, C.; Liou, S.-C.; Amine, K.; Xu, K.; Wang, C. *Nat. Nanotechnol.* **2018**, 13, (8), 715-722.
29. Zhang, X.; Kostecki, R.; Richardson, T. J.; Pugh, J. K.; Ross, P. N. *J. Electrochem. Soc.* **2001**, 148, (12), A1341-A1345.
30. Leung, K. *Chem. Phys. Lett.* **2013**, 568-569, 1-8.
31. Kanamura, K.; Toriyama, S.; Shiraishi, S.; Ohashi, M.; Takehara, Z.-i. *J. Electroanal. Chem.* **1996**, 419, (1), 77-84.
32. Browning, J. F.; Baggetto, L.; Jungjohann, K. L.; Wang, Y.; Tenhaeff, W. E.; Keum, J. K.; Wood, D. L.; Veith, G. M. *ACS Appl. Mater. Interfaces* **2014**, 6, (21), 18569-18576.
33. Li, W.; Dolocan, A.; Oh, P.; Celio, H.; Park, S.; Cho, J.; Manthiram, A. *Nat. Commun.* **2017**, 8, 14589.
34. Peled, E.; Golodnitsky, D.; Ardel, G. *J. Electrochem. Soc.* **1997**, 144, (8), L208-L210.
35. Takamatsu, D.; Koyama, Y.; Orikasa, Y.; Mori, S.; Nakatsutsumi, T.; Hirano, T.; Tanida, H.; Arai, H.; Uchimoto, Y.; Ogumi, Z. *Angew. Chem. Int. Ed.* **2012**, 51, (46), 11597-11601.
36. Jung, S. K.; Gwon, H.; Hong, J.; Park, K. Y.; Seo, D. H.; Kim, H.; Hyun, J.; Yang, W.; Kang, K. *Adv. Energy Mater.* **2014**, 4, (1), 1300787.
37. Yang, H.; Zhuang, G. V.; Ross, P. N. *J. Power Sources* **2006**, 161, (1), 573-579.
38. Smagin, A. A.; Matyukha, V. A.; Korobtsev, V. P. *J. Power Sources* **1997**, 68, (2), 326-327.
39. Takanashi, Y.; Orikasa, Y.; Mogi, M.; Oishi, M.; Murayama, H.; Sato, K.;

- Yamashige, H.; Takamatsu, D.; Fujimoto, T.; Tanida, H.; Arai, H.; Ohta, T.; Matsubara, E.; Uchimoto, Y.; Ogumi, Z. *J. Power Sources* **2011**, 196, (24), 10679-10685.
40. Champion, C. L.; Li, W.; Lucht, B. L. *J. Electrochem. Soc.* **2005**, 152, (12), A2327-A2334.
41. Gu, Y.; Chen, D.; Jiao, X. *The Journal of Physical Chemistry B* **2005**, 109, (38), 17901-17906.
42. Moshkovich, M.; Cojocaru, M.; Gottlieb, H. E.; Aurbach, D. *J. Electroanal. Chem.* **2001**, 497, (1), 84-96.
43. Andersson, A. M.; Abraham, D. P.; Haasch, R.; MacLaren, S.; Liu, J.; Amine, K. *J. Electrochem. Soc.* **2002**, 149, (10), A1358-A1369.
44. Tasaki, K.; Goldberg, A.; Lian, J.-J.; Walker, M.; Timmons, A.; Harris, S. *J. J. Electrochem. Soc.* **2009**, 156, (12), A1019-A1027.
45. Kim, Y. *Phys. Chem. Chem. Phys.* **2013**, 15, (17), 6400-6405.
46. Robert, R.; Bünzli, C.; Berg, E. J.; Novák, P. *Chem. Mater.* **2015**, 27, (2), 526-536.
47. Streich, D.; Erk, C.; Guéguen, A.; Müller, P.; Chesneau, F.-F.; Berg, E. J. *The Journal of Physical Chemistry C* **2017**, 121, (25), 13481-13486.
48. Graetz, J.; Hightower, A.; Ahn, C. C.; Yazami, R.; Rez, P.; Fultz, B. *The Journal of Physical Chemistry B* **2002**, 106, (6), 1286-1289.
49. Dahéron, L.; Dedryvère, R.; Martinez, H.; Ménétrier, M.; Denage, C.; Delmas, C.; Gonbeau, D. *Chem. Mater.* **2008**, 20, (2), 583-590.
50. Tarascon, J. M.; Vaughan, G.; Chabre, Y.; Seguin, L.; Anne, M.; Strobel, P.; Amatucci, G. *J. Solid State Chem.* **1999**, 147, (1), 410-420.
51. Cho, W.; Myeong, S.; Kim, N.; Lee, S.; Kim, Y.; Kim, M.; Kang, S. J.; Park, N.; Oh, P.; Cho, J. *Adv. Mater.* **2017**, 29, (21), 1605578.

Chapter 2. Abnormal self-discharge in lithium-ion batteries

(The content of this chapter has been published in *Energy & Environmental Science*. Reproduced with permission from W. M. Seong *et al.* Abnormal self-discharge in lithium-ion batteries. *Energy Environ. Sci.*, **2018**, *11*, 970-978. Copyright 2018, Royal Society of Chemistry.)

2.1. Introduction

Lithium-ion batteries have emerged as key power options for electric vehicles (EVs) and large-scale energy storage systems (ESSs) for renewable electricity production, as the associated intermittent and dispersed energy supply requires suitable storage systems. Their high and flexible energy/power characteristics, versatility, low maintenance, and high round-trip efficiency make lithium-ion batteries a promising alternative to other traditional batteries or conventional mechanical ESSs¹⁻³. Although lithium-ion batteries are currently prevailing in the electronics market and have thus been optimized for that purpose, these large-scale applications present new challenges for batteries that are distinct from those of consumer electronics. In addition to requiring unprecedentedly high energy storage characteristics per capita, the batteries must also be sustained in harsher operating environments⁴. One of the main differences for large-scale operation environments is that the batteries may be exposed to temperatures far below (in winter) or above (in summer) room temperature for an extended period. Moreover, the batteries would mostly be in a rest state at certain states of charge (SOCs) without being used for long periods, such as when EVs are parked outside. These conditions differ greatly from those expected

for the typical use of consumer electronics, which are mostly at room temperature and under constant operation.

When batteries are stored at a charged state for an extended period, one of the essential properties to consider is the self-discharge of the battery, which refers to the loss of charged capacity under open-circuit conditions^{5, 6}. The unwanted loss of capacity during the rest period is not only problematic in itself but also makes the prediction of the usable capacity of the battery non-trivial, which is critical for applications such as the use of EVs after parking. The main cause of self-discharge has conventionally been attributed to parasitic reactions between the active material and electrolyte^{4,7-9}, causing the degradation of the active material and involving transition metal dissolution^{10,11} and phase transformation^{12,13}. However, the understanding of the precise self-discharge mechanism and rate remains unclear. Nevertheless, LIBs have widely been perceived to exhibit the lowest self-discharge rate (<5% of stored capacity over 1 month of storage)¹⁴⁻¹⁶ of various types of rechargeable batteries such as nickel–metal hydride, nickel–cadmium, and lead-acid batteries. The new environments of batteries for EV and ESS applications, however, cast doubts over whether this low self-discharge rate of LIBs can be sustained even upon exposure of the battery to relatively harsh conditions such as fluctuating outdoor temperatures or long-term storage at various charged states, which would frequently occur for batteries stationed outside^{2,4}. In addition, recently, LIBs' validity at extreme temperatures such as <0 °C or >60 °C conditions has been the topic of the interest^{7,17-19}. There is thus a critical need to carefully revisit the self-discharge characteristics of LIBs under these new operating and rest conditions.

Herein, we report that the self-discharge of LIBs can be sensitively accelerated with short-term thermal exposure of the battery. It is demonstrated that when a 'history' has been generated by even short-term exposure to a moderate

temperature (60 °C or 80 °C), this thermal history is memorized in the cell and expedites the self-discharge of batteries even at room temperature. We verify that during short-term heating, the surface of the cathode is damaged by an oxidative reaction with the electrolyte, yielding a thin layer of a lithium-rich phase. In addition, this change is unrecoverable by cooling. More importantly, the phase formed at the surface can act as an internal ‘parasite’, continuously inducing gradual self-discharge by supplying lithium to the cathode. While it has been widely known that the battery operation at elevated temperature induces generally faster degradation of capacity over cycles^{5, 20}, this finding suggests that not only the operation temperature but also the ‘thermal history’ of the battery should be carefully considered as this history continues to affect the self-discharge rate afterwards.

2.2. Experimental section

2.2.1. Synthesis and characterization of LiCoO₂

LiCoO₂ powder was synthesized *via* a conventional solid-state reaction. Stoichiometric amounts of Li₂CO₃ (98%, Aldrich) and Co₃O₄ (Aldrich) were mixed using high-energy ball milling (Pulverisette 5, FRITTSCH) at 400 rpm for 4 h followed by calcination at 900 °C for 24 h in air. The structure of LiCoO₂ in the powder and electrode state was characterized using X-ray diffraction (XRD, D2 PHASER, Bruker). The LiCoO₂ crystal structure was determined to be the α -NaFeO₂-type structure with $R\text{-}3m$ space group and lattice parameters of $a = 2.815 \text{ \AA}$ and $c = 14.07 \text{ \AA}$ (**Figure 2.2.1a**), which are in good agreement with previously reported values^{21,22}. Based on scanning electron microscopy (SEM, SU-70, Hitachi) analysis, the LiCoO₂ secondary particles were determined to be approximately 1–5 μm in size and composed of smaller primary particles with spherical morphology (**Figure 2.2.1b**). The crystal structure of the surface regions of the LiCoO₂ was examined using transmission electron microscopy (TEM, JEM-2100F, JEOL), and its pristine nature retained the typical layered structure from the bulk to surface region (**Figures 2.2.1c and 2.2.1d**).

2.2.2. Electrochemical Characterization of Li_xCoO₂

A mixture of 92 wt% LiCoO₂ powder, 4 wt% super P carbon black, and 4 wt% polyvinylidene fluoride (PVDF) was dissolved in *N*-methyl-2-pyrrolidone (NMP, anhydrous, 99.5%, Aldrich) for the electrode preparation. The well-mixed slurry was applied onto aluminum foil using the doctor-blade method and dried under vacuum

overnight. Coin-type half cells (CR2032, Wellcos) were assembled using the composite electrode, a lithium metal counter electrode, a glass microfiber filter (grade GF/F, Whatman) as a separator, and 1 M LiPF₆ in ethylene carbonate/dimethyl carbonate (EC/DMC, 1:1 v/v, PanaX Etec) as the electrolyte. The water content in the electrolyte was measured to be less than 10 ppm using Karl–Fisher titration measurements. All of the preparation processes were performed in an argon-filled glove box. Galvanostatic measurements of the charge/discharge of the Li/LiCoO₂ cells were conducted within the voltage range between 3.0 and 4.2 V with a current density of 27 mA/g at 25 °C using a multichannel potentiogalvanostat (WBCS-3000, Wonatech, Korea). To ensure the reproducibility of the data, several tens of coin cells were examined, all of which exhibited similar behaviors (an example is presented in **Figure 2.2.2**).

2.2.3. Conditions of self-discharge experiments for Li_xCoO₂ electrode

Galvanostatic charge/discharge for seven pre-cycles were conducted under the previously described conditions before the self-discharge experiments. After seven formation cycles, the cells were charged to desired SOCs (0, 20, 60, and 90) at the eighth cycle and then transferred to an oven at either 60 °C or 80 °C and stored overnight (< 12 h). The cells were then transferred back to the cycler, and another seven galvanostatic cycles were performed at 25 °C. After the cycles, the cells were charged again to the desired SOCs, and the open-circuit voltage was measured as a function of time to probe the self-discharge of the cell. Experiments were also performed in the same manner for a full-cell setup, which consisted of a LiCoO₂ cathode and Li₄Ti₅O₁₂ anode (the details of the preparation and characterization of Li₄Ti₅O₁₂ are provided in **Figure 2.2.3**). To obtain the Li₄Ti₅O₁₂, stoichiometric

quantities of Li_2CO_3 (98% Aldrich) and TiO_2 (99% Aldrich) were mixed using high-energy ball milling (Pulverisette 5, FRITSCH) at 400 rpm for 12 h, and the mixture was calcined at 850 °C for 6 h in air. The resulting powder was confirmed to be spinel $\text{Li}_4\text{Ti}_5\text{O}_{12}$ with Fd-3m space group based on XRD measurements.

2.2.4. Characterization of Li_xCoO_2 electrodes

After the self-discharge tests, the Li_xCoO_2 electrodes were retrieved from the cells, lightly rinsed with DMC solvent to remove any residual electrolyte salts, and analyzed using XRD, TEM, and X-ray photoelectron spectroscopy (XPS; PHI 5000 VersaProbe, ULVAC-PHI). In the XPS analysis, a monochromatic Al $K\alpha$ X-ray source (1486.6 eV) was generated using an acceleration voltage of 15 kV, and the binding energy was referenced to the C 1s peak at 284.5 eV. The electron takeoff angle was 45° relative to the sample plane, and the pass energy was set to 23.5 eV. Depth profile analysis was performed with Ar-ion sputtering of 3 kV acceleration voltage, and the raster size was $2 \times 2 \text{ mm}^2$. The sputtering was performed in 1-min intervals for a total sputtering time of 5 min, and the rate was calibrated using a 100 nm SiO_2 reference film. It was observed that 20 nm of SiO_2 was etched by 1 min of sputtering. To minimize the damage of the sample with the organic thin film, which can be vulnerable to the electron beam, the acceleration voltage was set to 120 kV in the TEM observation.

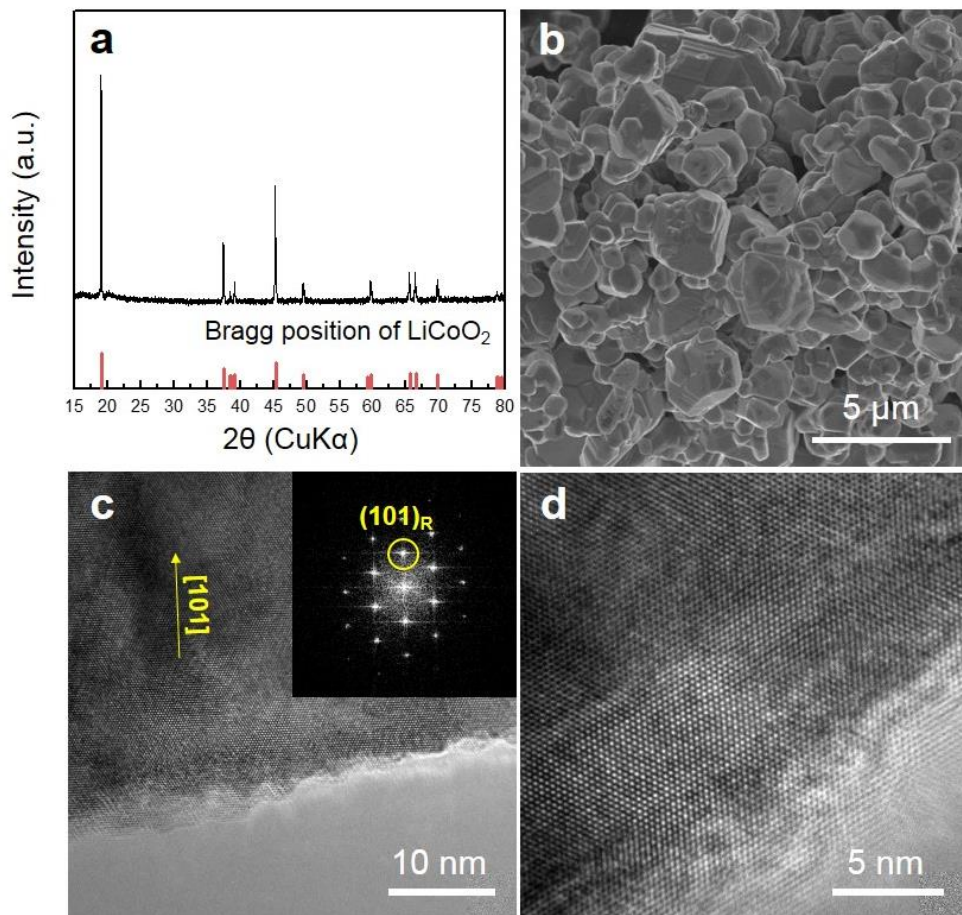


Figure 2.2.1. (a) XRD pattern, (b) SEM image, (c) and (d) high-resolution TEM (HRTEM) lattice image of LiCoO₂ powder. The inset in (c) shows the fast Fourier transformation calculated from the entire image.

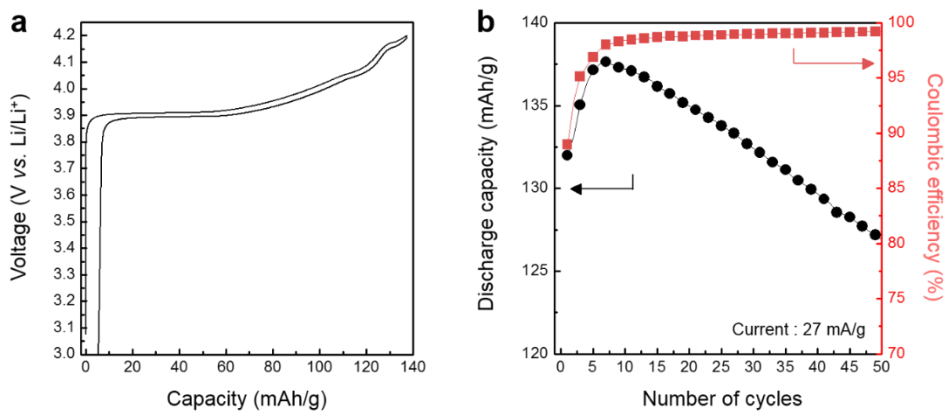


Figure 2.2.2. (a) Charge-discharge profile at sixth cycle and (b) cycle stability of Li/LiCoO₂ cell.

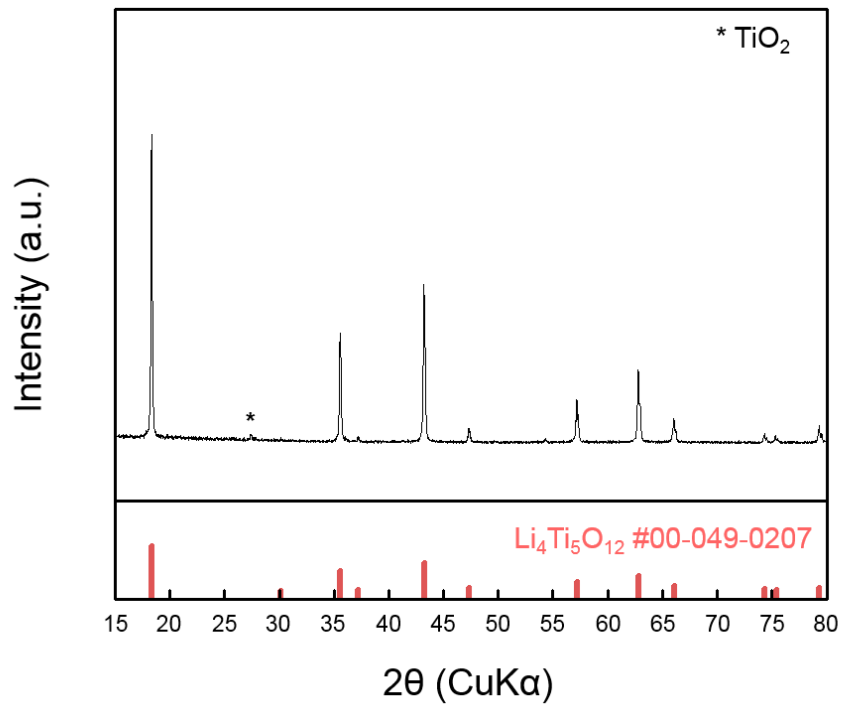


Figure 2.2.3. X-ray diffraction pattern of synthesized $\text{Li}_4\text{Ti}_5\text{O}_{12}$ powder.

2.3. Results and discussion

2.3.1. Demonstration of abnormal self-discharge

A conventional electrode/electrolyte pair, *i.e.*, a LiCoO₂ cathode and 1 M LiPF₆ in an EC and DMC (1:1 volume ratio) electrolyte was selected as a platform for the investigation. The electrochemical properties of LiCoO₂ half cells at room temperature are compared before and after storage at 60 °C, as shown in **Figure 2.3.1**. Seven pre-cycles were performed at room temperature before the fully discharged cell was stored at 60 °C overnight (the detailed experimental procedures are described in the experimental section). **Figure 2.3.1** presents the subsequent charge/discharge profiles of the two cells, which were almost identical regardless of the 60 °C storage except for a slight decrease in the capacity of less than 5 mAh/g. Although the reduction of the capacity after the high-temperature storage overnight was not substantial, it is consistent with the findings of Li *et al.*, who observed that the discharge capacity of a graphite/Li_xCoO₂ cell decreased after storage at 55 °C for 100 days²³. In that study, the reduction of the capacity was attributed to the formation of a resistive LiF phase on the surface of cathode *via* side reactions with electrolytes. We performed further experiments on the two cells by charging them to SOC 20 (~0.1 Li) and monitoring the open-circuit voltage at 25 °C. **Figure 2.3.2** shows the change in the open-circuit voltages (OCVs) of the cells over more than two weeks of measurements. The OCVs of the pristine cell were stably maintained at a constant value of 3.9 V (*vs.* Li/Li⁺) for more than 20 days (as indicated by the red squares). However, the cell that was heated at 60 °C overnight ('60 °C heated cell' in the graph) exhibited a gradual voltage reduction after 10 days and experienced an abrupt

voltage drop after 14 days in contrast to the pristine cell despite the similar electrochemical performance observed in **Figure 2.3.1**. The voltage was observed to further drop below 3.6 V (vs. Li/Li⁺) for the '60 °C heated cell' over a few more days. When the same experiment was performed using a cell that had been stored at higher temperature such as 80 °C ('80 °C heated cell' in the graph), a more rapid decrease of the voltage occurred over time. Additionally, we performed a similar experiment only for the cathode, which was retrieved from the pre-cycled reference cell. After storing this electrode in the electrolyte at 60 °C, a half cell was reassembled to monitor the rate of voltage decay ('60 °C heated electrode' in the graph). Notably, precisely the same behavior as the '60 °C heated cell' was observed for the '60 °C heated electrode', strongly implying that the observed voltage decay of the cell primarily originated from the cathode with thermal exposure.

In addition, we could confirm that this phenomenon is not a special case of LiCoO₂. The similar acceleration of the voltage decay rate was also observed for other commercialized cathode material such as LiFePO₄ after the short thermal exposure at 60 °C (**Figure 2.3.3**). In the synthesis of LiFePO₄ (LFP), a stoichiometric amount of Li₂CO₃, FeC₂O₄·H₂O and (NH₄)₂HPO₄ were mixed by wet ball-milling process in acetone for 24 hours, dried in vacuum, calcined at 350 °C for 10 hours, pelletized and heated at 600 °C again for 10 hours in Ar atmosphere¹. The pristine material was used without additional surface treatment. The morphology of the material is provided in **Figure 2.3.3a**, which is consistent with previous literatures^{24,25}. For the LFP sample, the electrodes were fabricated in almost same way with that for LiCoO₂ electrodes; the mixture of LFP, polyvinylidene fluoride (PVDF) binder, and super-P carbon with weight ratio of 7:1:2 was dissolved in N-Methyl-2-pyrrolidone (NMP) solvent, then the slurry was applied onto Al foil by doctor-blade method. The electrodes were dried at room temperature for overnight

before use. The coin-cells employing the LFP cathode, 1 M LiPF₆ in EC/DMC (1:1 v/v) electrolyte, GF/F glass fiber separator and Li metal anode were assembled and stored at 60 °C for 10 hours in identical protocols to the case of LiCoO₂ cells. After the short-term thermal history, the cell was charged into SOC 20 states, and their behaviors of voltage decay were carefully monitored in comparison to the one without the thermal history. Since the LFP undergoes the two-phase reaction with a flat voltage (~3.4 V vs. Li/Li⁺), a significant deviation from 3.4 V in the OCV would imply the self-discharge. In fact, we observed that the self-discharge is obviously accelerated in the case of LFP with the short-term thermal history as shown in **Figure 2.3.3b**. While the LFP electrode without thermal history (denoted as 'pristine cell') maintains its characteristic 3.4 V for the extended time (10 days), the one with the thermal history (denoted as '60 °C heated cell') displays the rapid voltage drop after 3 days. It clearly demonstrates that the LFP electrode undergoes the serious self-discharge once the thermal history is recorded.

Before further discussion, it was necessary to verify whether the voltage decay originated from the self-discharge or other types of side reactions. Therefore, we recharged the cells that had experienced the voltage decay in **Figure 2.3.2** after reaching ~3.3 V (vs. Li/Li⁺). **Figure 2.3.4** shows that the cells could be recharged, following the same electrochemical profile as that of the pristine cell, confirming that the voltage decay was due to the self-discharge. Moreover, we examined the Li_{0.9}CoO₂ electrodes by disassembling the cell after the self-discharge using XRD analysis, as shown in **Figure 2.3.5**. The XRD pattern of the electrode at SOC 20 before the voltage decay was characteristic of a typical delithiated Li_xCoO₂ structure with two-phase coexistence, consistent with previous reports^{21, 26}. However, a major change occurred in the pattern after the voltage decay, with the appearance of only a single characteristic (003) peak with an identical position to that of the reference

LiCoO₂ (see inset of **Figure 2.3.5**); this finding is indicative of the formation of stoichiometric LiCoO₂. The recovery of the stoichiometric LiCoO₂ (SOC 0) from the Li_{0.9}CoO₂ (SOC 20) clearly confirms the self-discharge of the cell, which involves lithium reinsertion into the bulk Li_xCoO₂. In our further experiments, we observed that this type of thermal-history-induced self-discharge occurs not only for cells at SOC 20 but also in various other SOCs such as SOC 60 and 90 (**Figure 2.3.6**). These findings imply that this self-discharge can universally occur whenever the battery is in charged states. We also found here that thermal history at higher SOCs induced slightly faster self-discharge rate, which is attributed to a more oxidative condition of the LiCoO₂ cell causing side products generated, as will be discussed in detail later.

To validate the reproducibility of the self-discharge of the cells, multiple numbers of cells were examined under similar conditions, and the resulting statistics are presented in **Figure 2.3.7**. In this figure, the time (days) needed for the cell initially at SOC 20 to reach the self-discharged state (SOC 0) is plotted as a function of the thermal history. The average time of the self-discharge for the 60 °C history was 13.8 ± 5.8 days, whereas that for the 80 °C history was 10.1 ± 6.5 days, demonstrating the stronger dependency with higher-temperature history and the reproducibility of the thermal-history-induced self-discharge of the Li_xCoO₂ electrode. Self-discharge tests were also performed using a full cell composed of a LiCoO₂ cathode and Li₄Ti₅O₁₂ anode to exclude the possible detrimental effect of the lithium electrode in the half cell.

The accelerated self-discharge was consistently observed even in full cells, as shown in **Figure 2.3.8**. The demonstration of abnormal acceleration of self-discharge was also possible with pouch-type cell with a larger energy storage capability. (**Figure 2.3.9**). The fabricated cell is shown in the inset (left) of **Figure**

2.3.9a, in comparison to the original 2032 coin-type cell (right). The electrochemical operation of the cell showed the characteristic charge/discharge profile of LiCoO₂ cathode at the current of 1 mA in the voltage range of 2.8-4.3 V (vs. Li/Li⁺) as shown in **Figure 2.3.9a**. For this fabricated pouch-type cell, we performed the same self-discharge test as in the original coin cell with or without thermal history. **Figure 2.3.9b** clearly confirms that the accelerated self-discharge induced from a short-term thermal exposure is observed in the practically used pouch-type cell. Compared with the cell without a thermal history (indicated as ‘pristine cell’ in the graph), the open-circuit-voltage of the pouch-cell suddenly drops after a few days of storage below 3.6 V when 60 °C of thermal history had been recorded (indicated as ‘60 °C heated cell’ in the graph). Note that it is an even more dramatic difference arising from the thermal history than the case observed for the coin cell. While it can be partly attributed to the non-optimized pouch-type cell configuration here, it implies that the surface parasitic reaction that causes the self-discharge can be more sensitively expedited with the un-optimization of cells. The consistent observation indicates that the accelerated self-discharge behavior with the thermal history is the common phenomenon regardless of the cell-types.

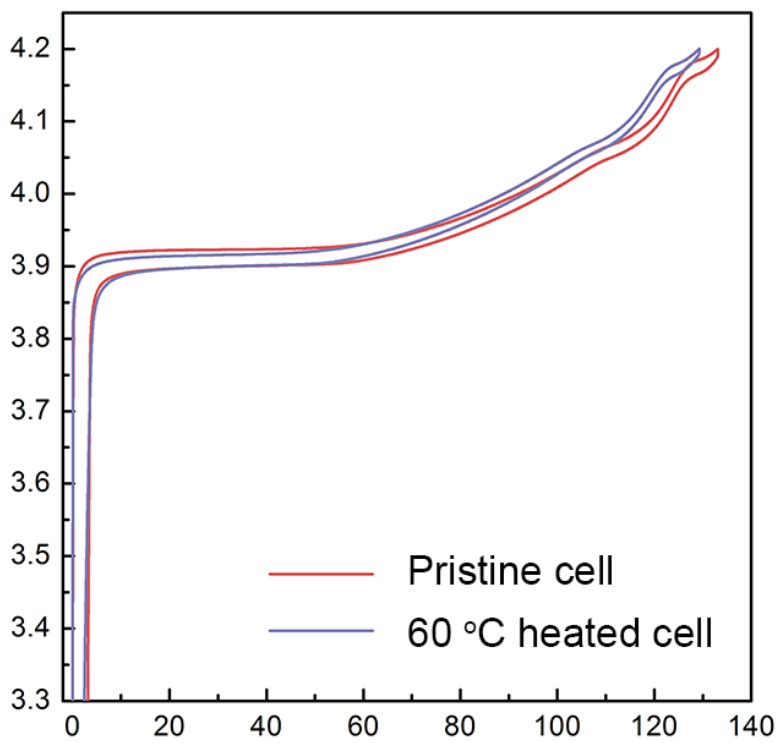


Figure 2.3.1. Comparison of voltage profiles of Li_xCoO_2 before and after heating at 60 °C.

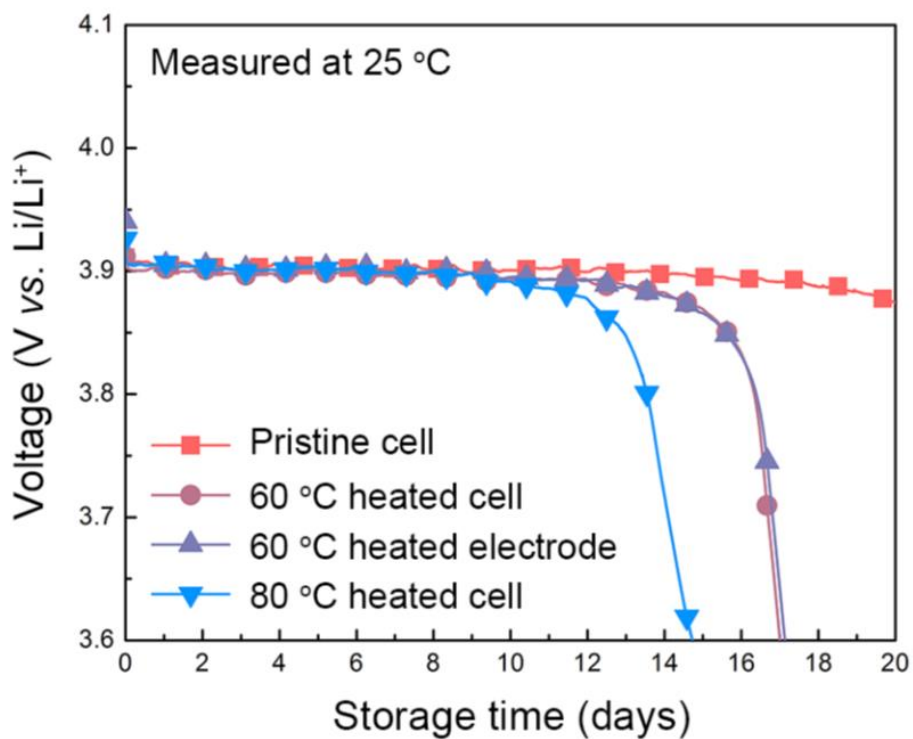


Figure 2.3.2. Representative voltage decay curve of Li_xCoO_2 cathode charged to SOC 20 measured at 25 °C. Before the start of measurement, each coin cell was stored at various temperatures overnight, as indicated in the graph.

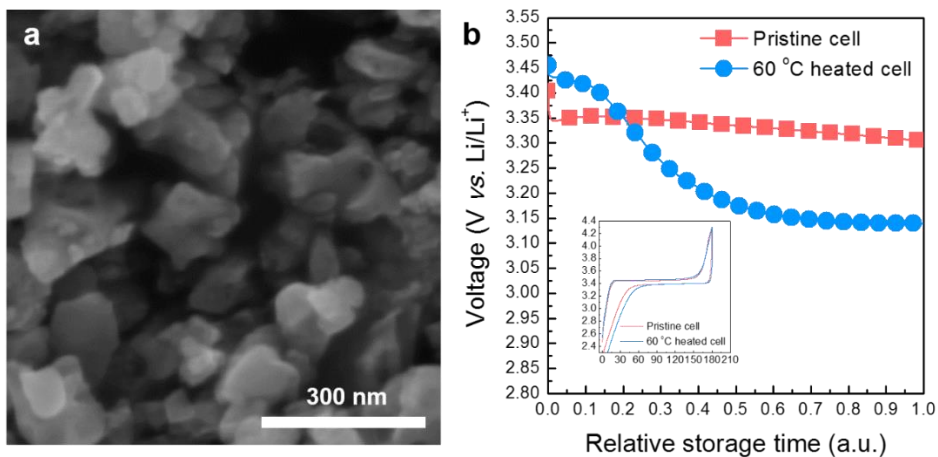


Figure 2.3.3. (a) SEM images of synthesized LiFePO_4 particle, respectively. (b) Representative voltage decay curve of Li_xFePO_4 and $\text{Li}(\text{Ni}_{0.6}\text{Co}_{0.2}\text{Mn}_{0.2})\text{O}_2$ cathode charged to SOC 20, respectively, with/without 60 °C thermal history. Inset figure shows the representative voltage profile of $\text{Li}/\text{LiFePO}_4$ cell. Current rate was set to 17 mA/g.

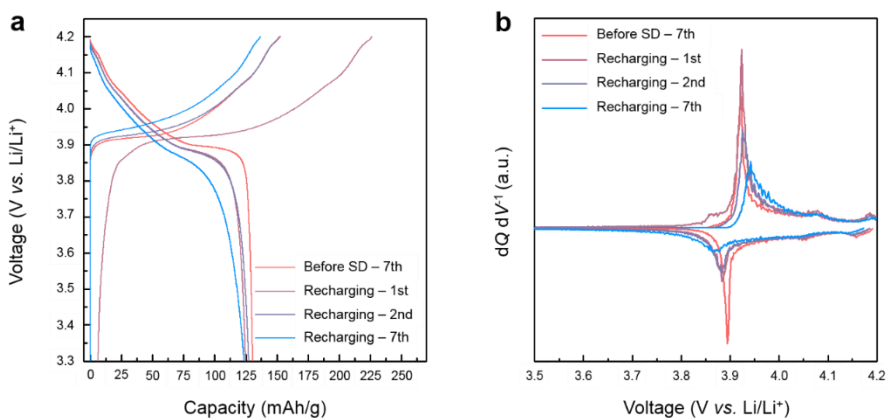


Figure 2.3.4. (a) Voltage profiles and (b) dQ/dV^{-1} plots from (a) of self-discharged Li_xCoO_2 for which a thermal history at 60°C was written obtained by recharging it with a current of 27 mA/g . The voltage profile was monitored until the 7th cycle, and the representative results are compared with that before the Li_xCoO_2 was self-discharged (marked as ‘Before SD (self-discharge)’).

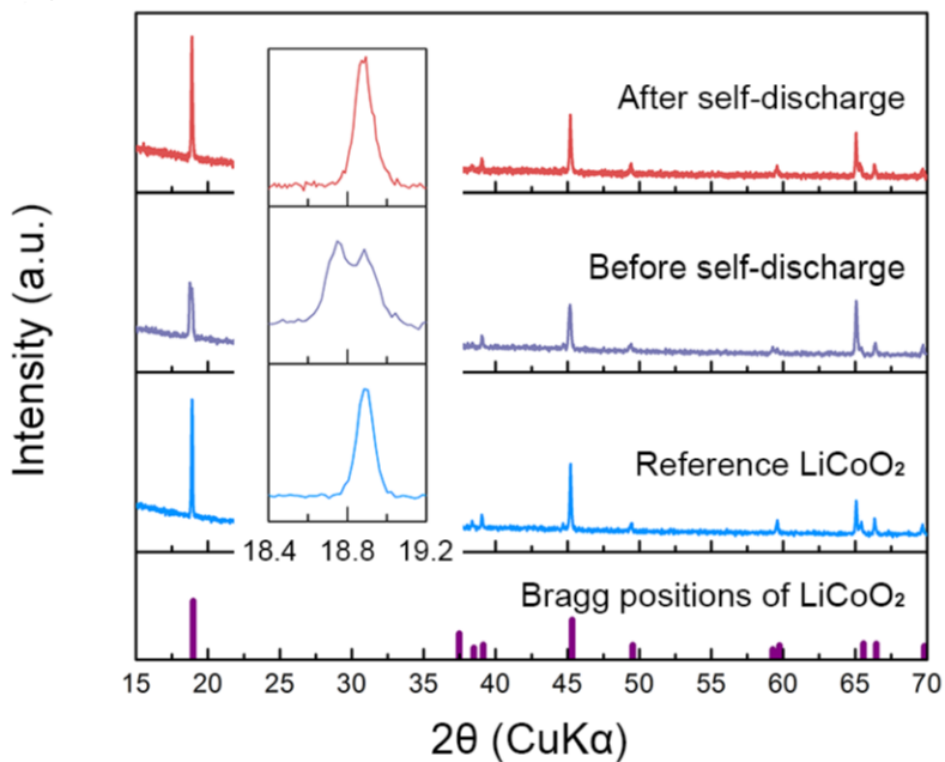


Figure 2.3.5. XRD pattern of Li_xCoO_2 electrode at SOC 0 approached by self-discharge of cathode (voltage decay to 3.3 V), which had been heated at 60 °C overnight compared with that of the electrode from the reference LiCoO_2 . The inset shows the XRD pattern magnified near the (003) peak of Li_xCoO_2 .

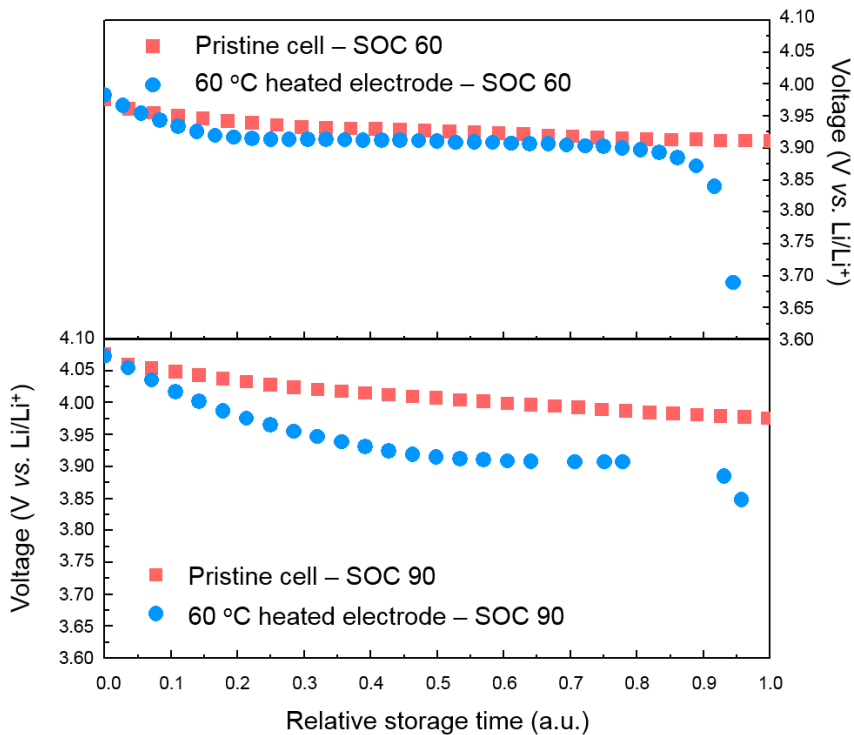


Figure 2.3.6. Voltage decay curve of LiCoO₂ cathode with thermal history at 60 °C at various SOC (SOC 60 and 90). All the measurements were performed at 25 °C. In each case, the voltage decay behavior was universally observed upon storage at 60 °C.

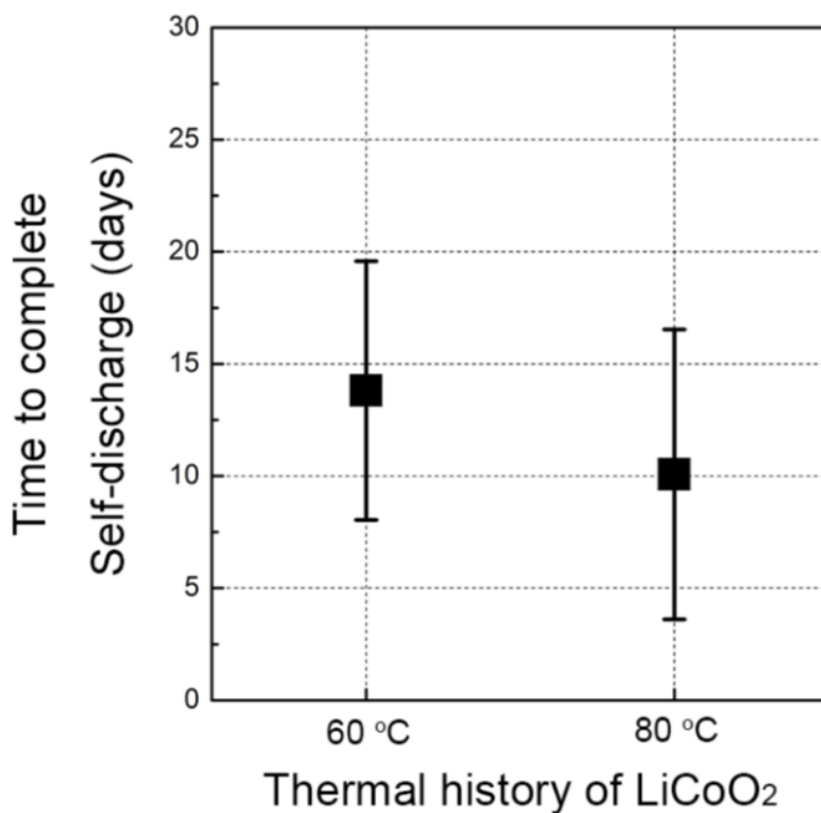


Figure 2.3.7. Summary statistics for time to complete self-discharge (when the potential of the Li/LiCoO₂ half-cell approached 3.3 V) at 25 °C collected from more than 5 samples charged to SOC 20 with different thermal histories.

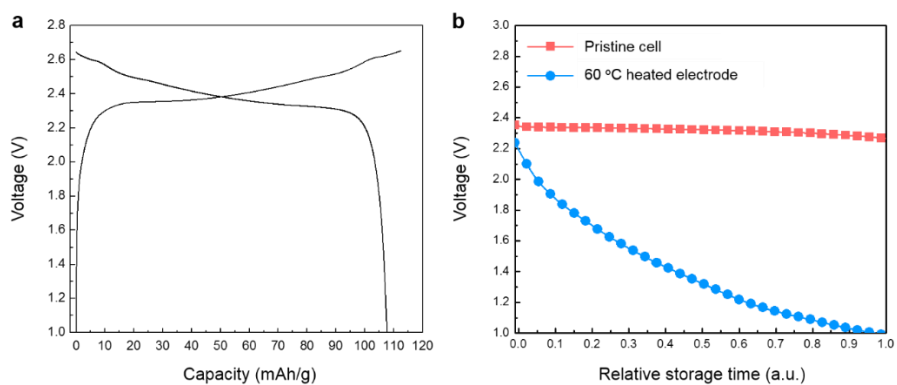


Figure 2.3.8. (a) Typical charge/discharge profile of a full cell using a Li_xCoO_2 cathode and $\text{Li}_{4+x}\text{Ti}_5\text{O}_{12}$ anode. (b) Decay of OCV for a cell exposed to 60 °C heat treatment. The cathode was soaked in electrolyte solution at 60 °C.

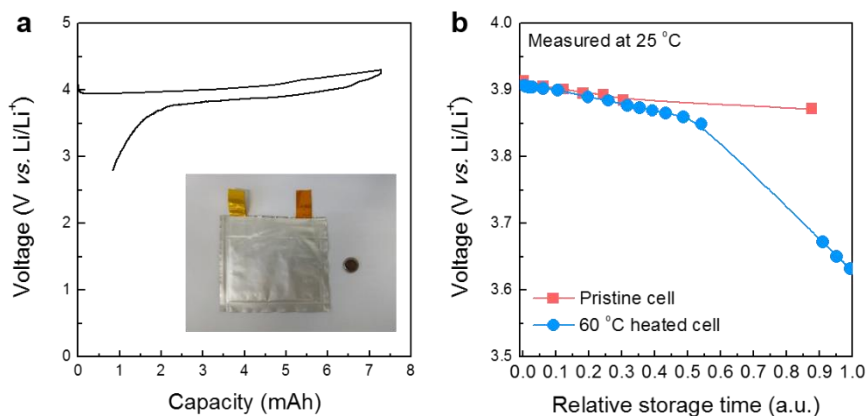


Figure 2.3.9. (a) Representative electrochemical voltage profile of Li/LiCoO₂ pouch-type cell. Current density for charge and discharge was set to 1 mA. Inset photograph shows the relative size of the pouch (left: 10 cm x 10 cm) compared with the conventional 2032 coin-type cell (right). The pouch-type cell was fabricated using 2 cm x 7 cm rectangular LiCoO₂ cathode, lithium metal anode, 1 M LiPF₆ in EC/DMC (1:1 v/v) and Celgard 2400 separator. (b) The probe of the voltage decay as a function of time for the pouch-cell containing Li_xCoO₂ cathode with/without 60 °C thermal history. The open-circuit-voltages of the two cells were monitored for 5 days.

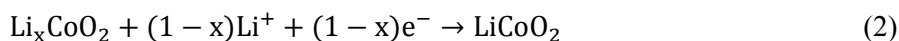
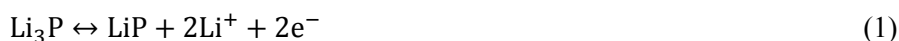
2.3.2. Underlying mechanism of abnormal self-discharge

To understand this unexpected abnormal self-discharge, the change of the Li_xCoO_2 electrode with thermal exposure was carefully examined. Although damage in the bulk structure was not obvious other than the re-lithiation as observed in the XRD pattern in **Figure 2.3.5**, surface-specific analysis of the electrode was performed to probe the possible origin of this self-discharge such as degradation of the interface between the active material and electrolyte²⁷⁻²⁹. **Figure 2.3.10a** presents a representative TEM image of the surface structure of the electrode after the self-discharge. Notably, a relatively thick surface layer (~ 50 nm) surrounded the bulk particle, which we labeled the ‘degraded region,’ as denoted by the red dotted line. This surface layer differed distinctively from the usual interface layer on an electrode after electrochemical cycling, which is typically an amorphous thin film with a thickness of less than 10 nm (**Figure 2.3.11**). In **Figure 2.3.11**, The 5-nm-thick crystalline region adjacent to the amorphous surface layer has a d-spacing of 2.4 Å, unlike that of the bulk region of 4.7 Å, which likely corresponds to the reduction of Li_xCoO_2 due to electrolyte oxidation, as previously observed by Ogumi *et al.*²⁹. This electrolyte oxidation may cause the extraction of lithium and induce the transformation of the LiCoO_2 at the surface to Co_3O_4 or other species *via* reduction.

Figures 2.3.10b and **2.3.10c** reveal that the degraded region consisted of many nanoparticles dispersed within an amorphous matrix with clear lattice images, which differs from that of typical Li_xCoO_2 . Although the bulk region in **Figure 2.3.10c** contains diffraction spots indexed as the characteristic planes of LiCoO_2 in fast Fourier transform (FFT), they became blurred at the boundary, and the degraded region (**Figure 2.3.10b**) only exhibited an amorphous character with embedded crystalline nanoparticles. To determine when this degraded region was formed, we

also examined the surface structure of the electrode (SOC 20) directly after the heat treatment without waiting for the self-discharge, as illustrated in **Figure 2.3.10d**. Nearly the same overall structure was observed randomly dispersed nanoparticles of ~10 nm in size embedded within the amorphous matrix, as indicated by the yellow dotted line (additional images are provided in **Figure 2.3.12**). The identical surface structures of the two different electrodes imply that it was formed immediately after the thermal exposure of the electrode and was maintained during the entire self-discharge process. Nevertheless, what is interesting is that the electrodes contained slightly different crystalline phases of nanoparticles in the amorphous framework according to the FFT analysis, as observed in **Figures 2.3.13a** and **2.3.13b**. Even though they both exhibited clear signatures of the CoP phase, the LiP phase was detected in the electrode after the self-discharge, whereas the Li₃P phase was exclusively observed for the electrode before the self-discharge without a trace of LiP. In addition, some unidentified spots were present in the FFT image, whose lattice could not be matched with known compounds containing Li, Co, P, F, C, or O (marked with white dotted lines in **Figures 2.3.13a** and **2.3.13b**).

It should be noted that the ‘charged’ Li_{0.9}CoO₂ (SOC 20) was initially surrounded by Li₃P after heating, whereas only the lithium-deficient LiP phase was detected on the surface of the ‘self-discharged’ LiCoO₂. This finding hints at the origin of the self-discharge, based on which we proposed the following possible mechanism. During the self-discharge, lithium is spontaneously inserted from Li₃P into Li_xCoO₂, which results in the conversion of Li₃P to LiP *via* the routes presented in the following reactions:



Li₃P has been reported to be capable of functioning as an anode material *via* the

conversion reaction in lithium cells expressed in (1)^{30,31}. We calculated the theoretical potential of reaction (1) and it exhibited ~ 0.87 V vs. Li/Li⁺, which agrees with previously reported experimental values^{30,31} (the formation energies used in the calculation were obtained from the *Materials Project* database³²). Thus, the Li₃P on the surface layer can serve as an internal source of lithium, inducing chemical lithiation of the Li_xCoO₂ cathode. The chemical potential of lithium in the Li₃P phase is higher than that in the charged Li_xCoO₂ cathode (~ 4 V vs. Li/Li⁺); thus, lithium from the surface Li₃P can be spontaneously inserted into the bulk Li_xCoO₂ even under rest conditions. To support our speculation of internal ‘parasites’ that induces the self-discharge, we stored a dried electrode with Li₃P on the surface in an argon atmosphere for a long time (>10 days) at 25 °C after charging to SOC 20 and then probed the evolution of this sample over time. **Figure 2.3.14** clearly reveals that the intensity ratio of the lithium-poor to lithium-rich phase (*i.e.*, LiCoO₂) gradually changed, with the peak corresponding to stoichiometric LiCoO₂ growing at the expense of that of the lithium-poor phase²³. The notable increase in the peak intensity of LiCoO₂ with time even after disassembly of the cell and the drying process supports the speculation that this occurs *via* chemical lithiation from the Li₃P. However, the electrode without Li₃P did not exhibit a noticeable change in the intensity ratio, as illustrated in **Figure 2.3.15**, inferring the absence of the self-discharge.

To further prove that the chemical lithiation of Li_xCoO₂ using Li₃P is possible, we simply mixed Li_{0.9}CoO₂ and Li₃P powders and stored the mixture in an argon atmosphere. The change of the XRD pattern of the Li₃P–Li_{0.9}CoO₂ powder mixture was monitored during the storage and compared with that of pristine Li_{0.9}CoO₂ powder. To synthesize Li₃P, we used a previously reported method⁴. Li metal and red phosphorus powder were mixed and heated at 200 °C for 5 h, and the

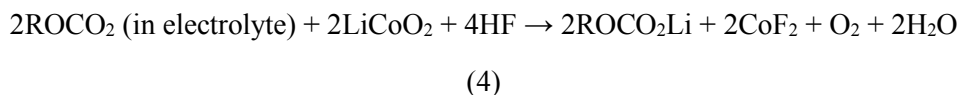
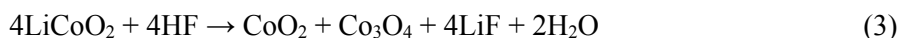
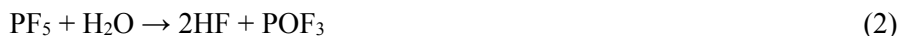
surrounding environment was further increased to 400 °C and maintained at this temperature for 5 h. The resulting compound was ground using a mortar and calcined again at 400 °C for 5 h. The entire procedure, including the calcination and grinding, was conducted in an argon atmosphere. As observed in the SEM image in **Figure 2.3.16a**, the average size of the Li_3P particles was $\sim 1 \mu\text{m}$, which is smaller than that of LiCoO_2 (see **Figure 2.3.16b**). This finding indicates that the contact of Li_3P and LiCoO_2 is intact when they are mixed together. The XRD pattern of the resulting powder in **Figure 2.3.16b** indicates the presence of the Li_3P phase as the majority phase and other unidentified impurity as the minority phase. The Li_3P powder was mixed with charged $\text{Li}_{0.9}\text{CoO}_2$ powder retrieved from the charged Li/LiCoO_2 coin cell (half of the retrieved powder was mixed with Li_3P powder at a weight ratio of 10:1). The XRD pattern of this mixture (which was stored in an argon atmosphere) was monitored for 7 days and compared with that from only $\text{Li}_{0.9}\text{CoO}_2$, which was obtained from the other half of the $\text{Li}_{0.9}\text{CoO}_2$ powder retrieved from the charged coin cell. As observed in **Figure 2.3.16c**, upon extended storage of this mixture, the peak corresponding to the lithium-poor phase gradually disappeared, whereas that of the lithium-rich phase grew, implying the spontaneous lithiation of the delithiated $\text{Li}_{0.9}\text{CoO}_2$. However, the storage of the pristine $\text{Li}_{0.9}\text{CoO}_2$ powder under identical conditions did not induce any change in the XRD pattern as shown in **Figure 2.3.16d**. This finding provides direct evidence of the role of Li_3P as a lithium source in the chemical lithiation of Li_xCoO_2 .

The origin of the Li_3P phase formation is unclear; however, it is speculated that the LiPF_6 salt or side product from it in the electrolyte served as an oxidizing agent, corroding the surface of the Li_xCoO_2 particles, which were reduced to form Li_3P -containing byproducts³³. It is well known that the thermal stability of LiPF_6 salt is relatively poor, and its decomposition starts from 107 °C³⁴. Generally, the

decomposition proceeds as shown by the following equations³⁵⁻³⁷:



When there is a trace amount of water in the electrolyte, HF is formed and triggers series of reactions shown below^{36,37}



Meanwhile, it is also known that a trace amount of water in electrolyte can react with salt itself to form HF³⁵:



It was suggested that several forms of fluorinated phosphoric acids can be formed, which led to formation of phosphoric acid³⁸:



Because of continuous generation of water as shown in equation (3) and (4), only small trace of water is sufficient to induce these reactions. Previous studies have suggested the role of phosphoric acid acting as phosphorus source for the formation

of phosphide when it is in chemical contact with metal sources in highly oxidative conditions such as at high temperature^{39,40}. We believe that this scenario is also applicable in the case of the surface of LiCoO_2 by the thermal history, where the phosphoric acid leaches out the lithium from LiCoO_2 forming the Li_3P . Therefore, only short exposure of electrolyte/electrode interface to 60 °C or 80 °C is enough to generate small amount of phosphide impurities to complete the chemical lithiation of Li_xCoO_2 during abnormal self-discharge. In order to support this conversion-type reaction of phosphide, we stored the Li/LiCoO_2 cell with the thermal history in room temperature for extended period and probed the open-circuit voltage (OCV). As shown in **Figure 2.3.17**, the decrease of OCVs of the cell did not stop at ~ 3.0 V, which is known as the OCV of fully discharged LiCoO_2 , and it dropped further down below ~ 1.7 V. This voltage matches well with the reported value of equilibrium potential of the Li_3P conversion reaction³¹, and clearly indicates the conversion-type of reaction on the surface of LiCoO_2 . This speculation was further explored by applying STEM analysis of the surface structure, as discussed in the following paragraph.

Elemental analysis of the surface was further performed for the self-discharged Li_xCoO_2 using scanning transmission electron microscopy coupled with energy-dispersive X-ray spectroscopy (STEM–EDS). **Figure 2.3.18** presents STEM images around the degraded region with the corresponding elemental mapping. A clear boundary is observed between the degraded region and Li_xCoO_2 bulk, as indicated by orange dashed line in **Figure 2.3.18a**. Notably, we observed the presence of significant amounts of phosphorus and fluorine in the degraded region, where the nanoparticles were mostly located, as shown in **Figures 2.3.18b** and **2.3.18d**. Moreover, the elemental line profile of phosphorus along the red line in **Figure 2.3.18b** suggests that the phosphorus content increased starting from the

degraded region and suddenly dropped at the boundary with the bulk region, as shown in **Figure 2.3.18c**, indicating that phosphorus is one of the major components of the degraded region. However, **Figure 2.3.18e** shows that cobalt was broadly distributed both in the bulk and in the degraded regions, confirming that the degraded region was related to the decomposition of Li_xCoO_2 itself. Carbon was also detected mainly in the degraded region, most likely due to the decomposition of the organic electrolyte and the formation of a solid-electrolyte interphase (SEI) layer^{41,42} and slightly in the bulk (**Figure 2.3.18f**). Considering that the sole source of both fluorine and phosphorus in the cell is the LiPF_6 salt, it is believed that the LiPF_6 salt in the electrolyte reacted with Li_xCoO_2 during the short heat treatment to produce the degraded surface structure. Moreover, the presence of the substantial amount of phosphorus is consistent with the presence of Li_3P in the degraded region, as observed in the TEM results in **Figures 2.3.18**, strongly supporting the speculation that the internal parasitic lithium source originated from interaction with the electrolyte salts.

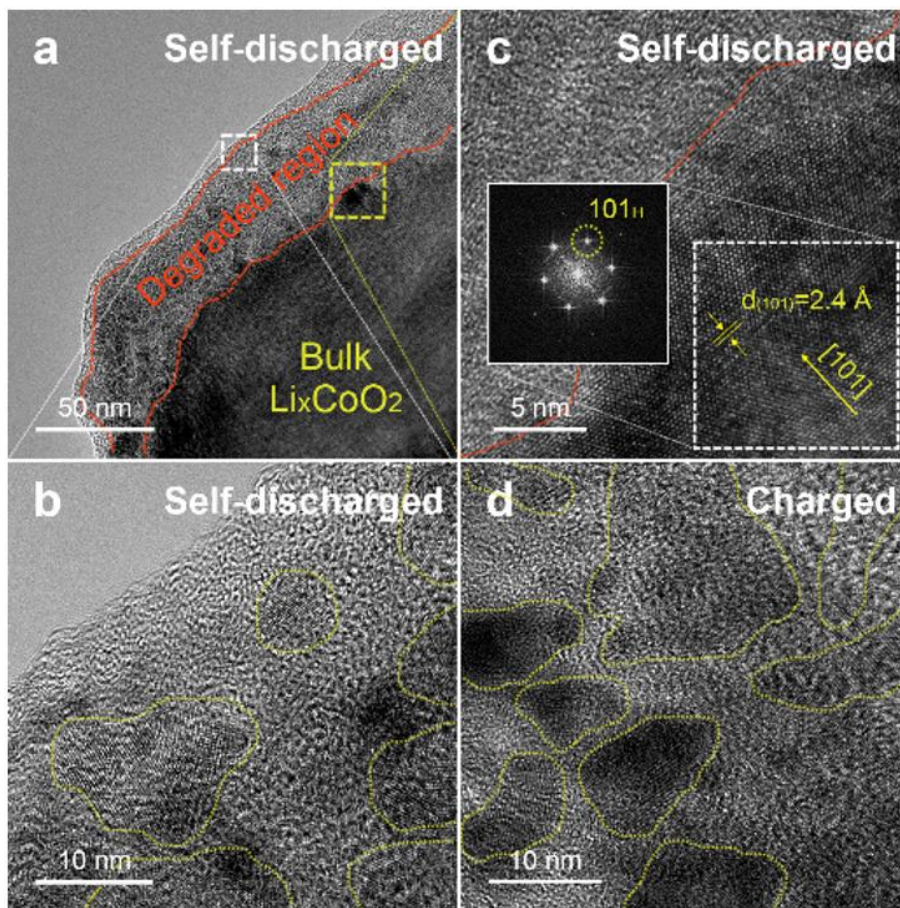


Figure 2.3.10. TEM images of surface of Li_xCoO_2 with thermal history at 60°C after self-discharge was performed: (a) low-magnification image and (b, c) high-magnification images of regions outlined by (b) white dashed square and (c) yellow dashed square in (a). (e) Fast Fourier transforms calculated from degraded region in (a). (d) High-magnification TEM image of degraded region of Li_xCoO_2 obtained directly after charging to SOC 20.

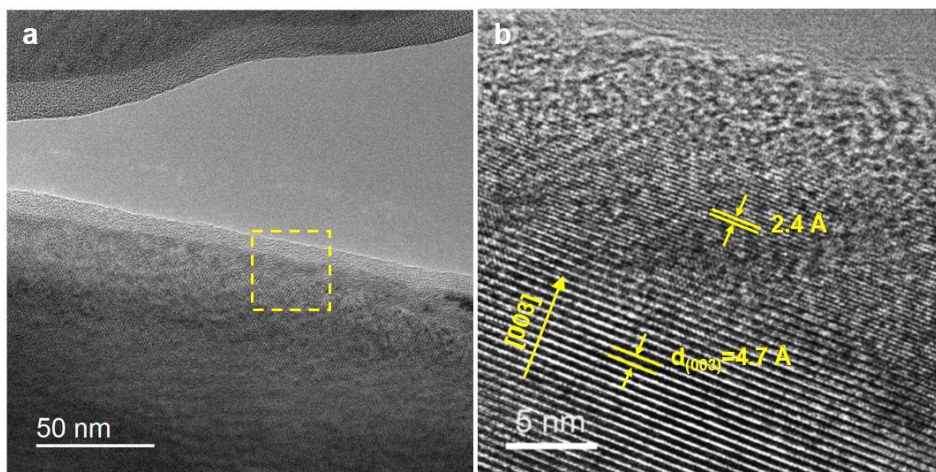


Figure 2.3.11. TEM images of surface of Li_xCoO_2 without heating: (a) low-magnification image and (b) high-magnification image of region outlined by yellow dashed square in (a).

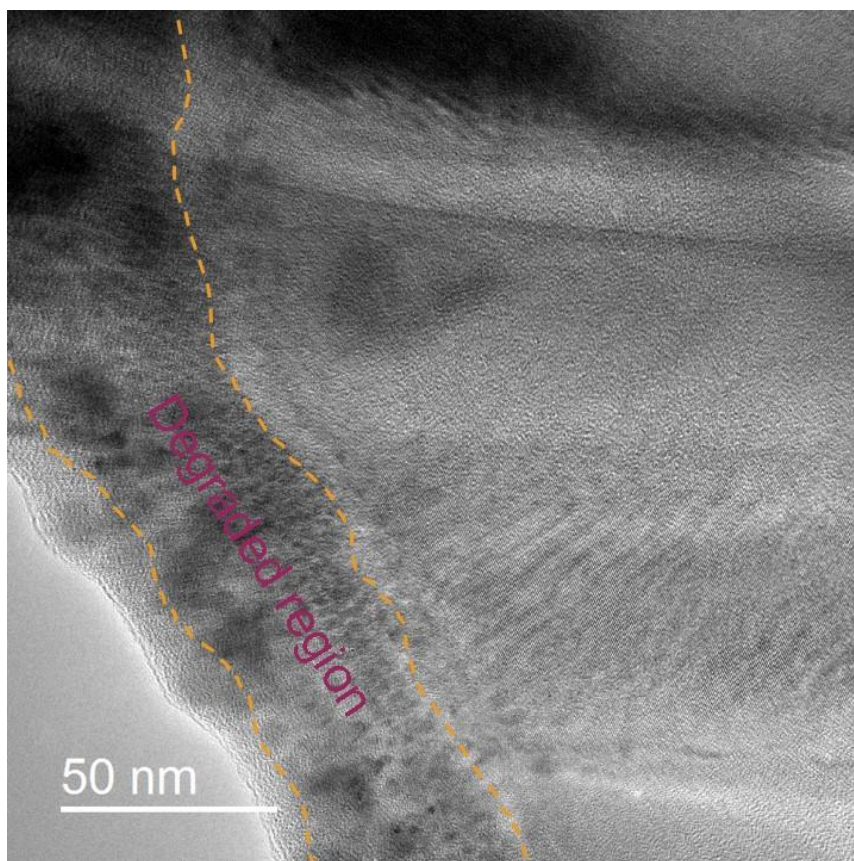


Figure 2.3.12. Low-magnification TEM image of Li_xCoO_2 obtained directly after charge to SOC 20 for which a thermal history of 60 °C was recorded.

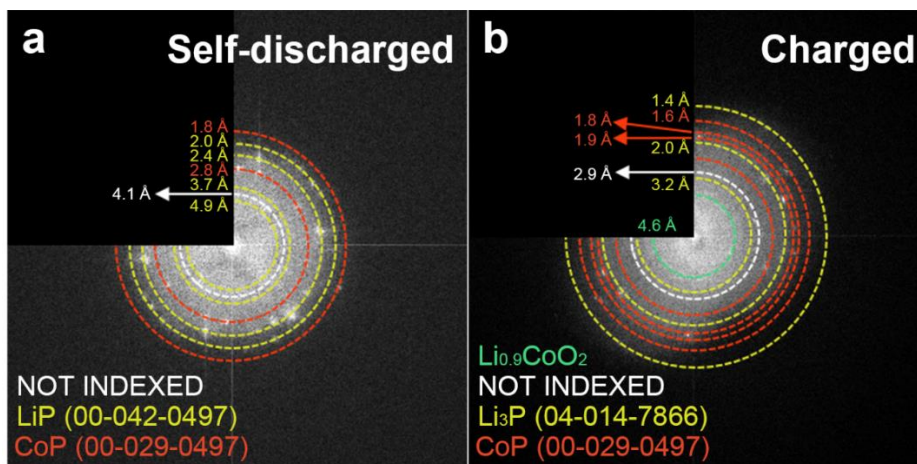


Figure 2.3.13. (a) Fast Fourier transforms calculated from degraded region in (a). (d) High-magnification TEM image of degraded region of Li_xCoO_2 obtained directly after charging to SOC 20. (b) Fast Fourier transform calculated from degraded region of charged Li_xCoO_2 .

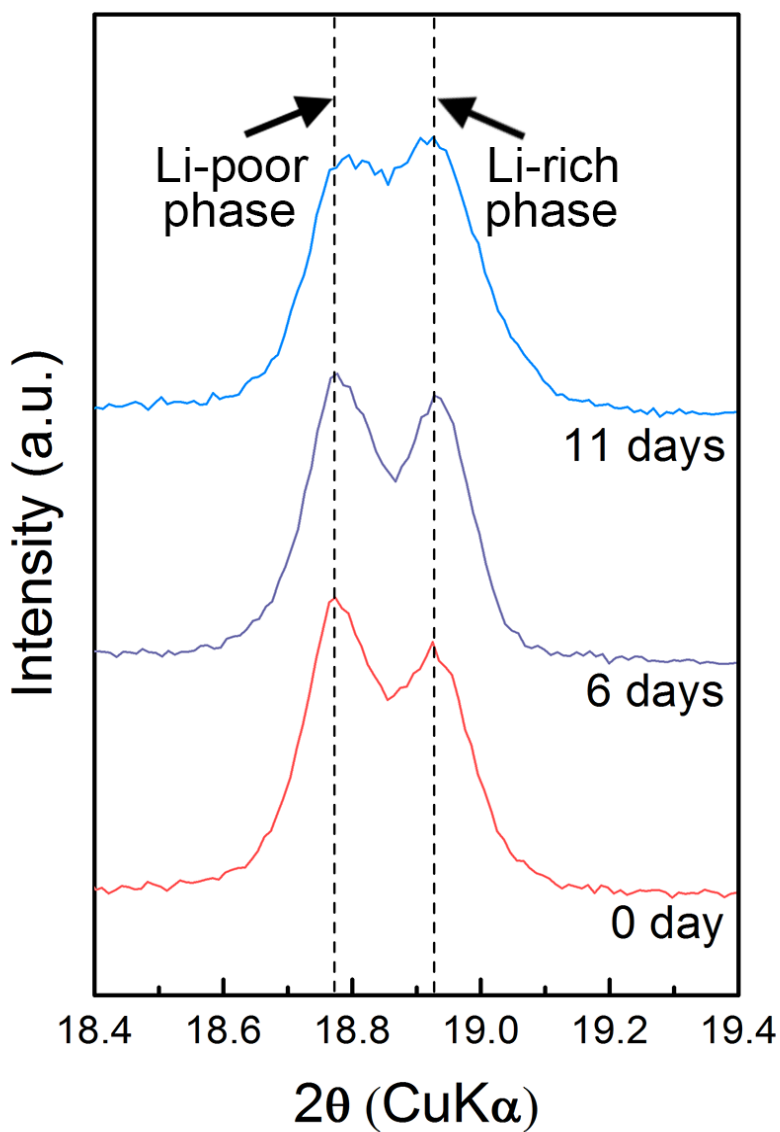


Figure 2.3.14. Traces of XRD patterns of charged Li_xCoO_2 (SOC 20) electrode with thermal history at 60 °C. The electrodes were retrieved from the coin cell and rinsed, dried, and stored in an argon atmosphere.

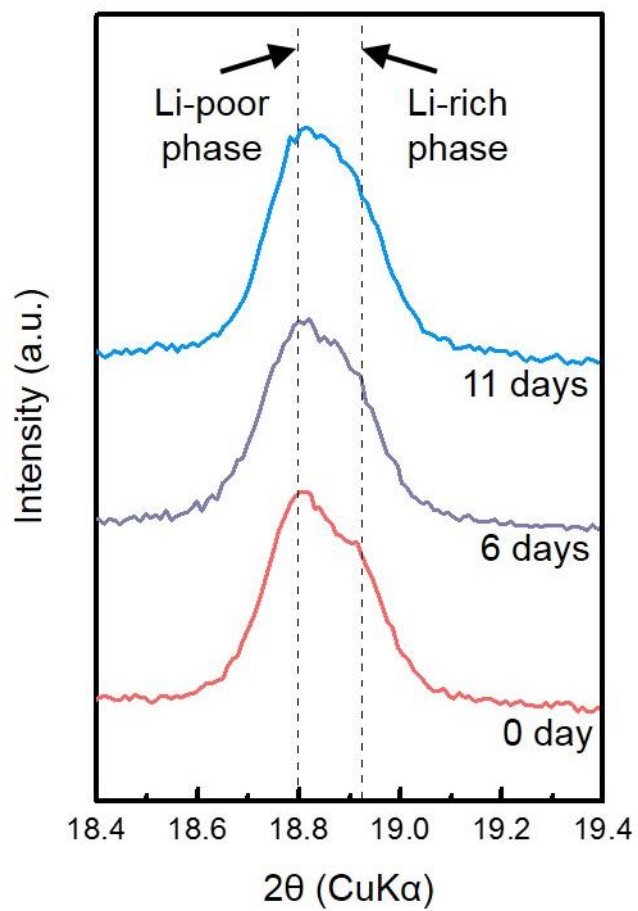


Figure 2.3.15. Trace of XRD patterns of charged Li_xCoO_2 (SOC 20) electrode without thermal history.

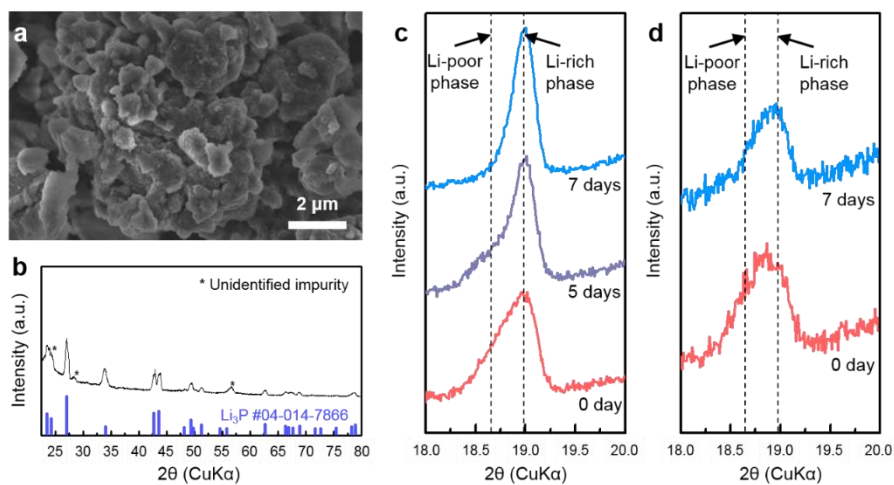


Figure 2.3.16. (a) SEM image and (b) XRD pattern of synthesized Li_3P powder. Traces of XRD patterns of delithiated $\text{Li}_{0.9}\text{CoO}_2$ powder (c) mixed with Li_3P powder or (d) not mixed with Li_3P powder during storage in an argon atmosphere.

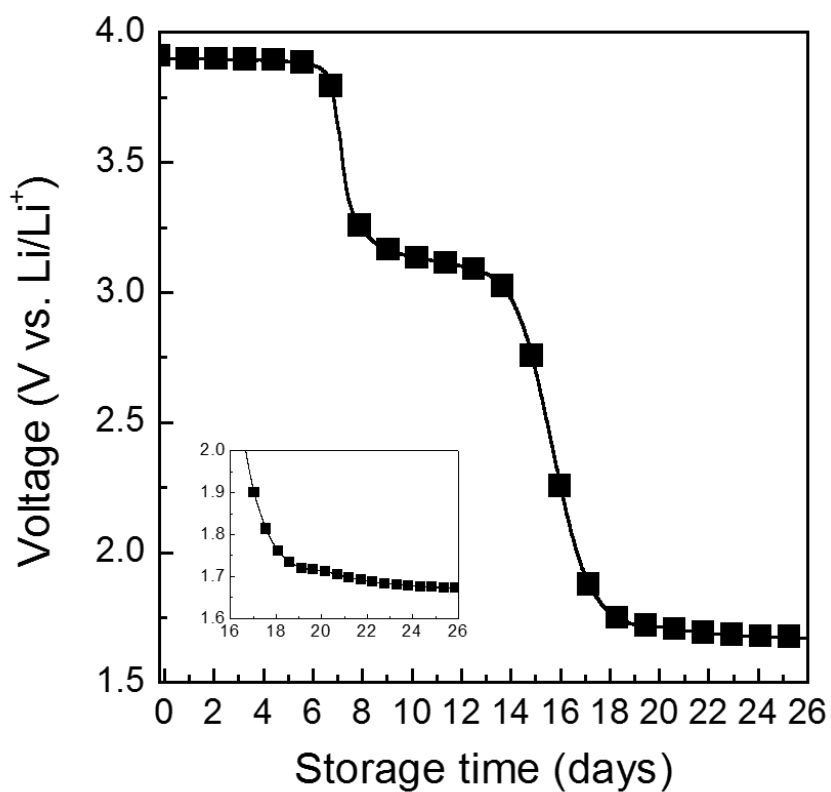


Figure 2.3.17. Change of open-circuit voltage of Li/LiCoO₂ cell with thermal history during storage which is allowed to decrease under 3.0 V. Inset shows the same figure magnified at the region nearby ~1.7 V.

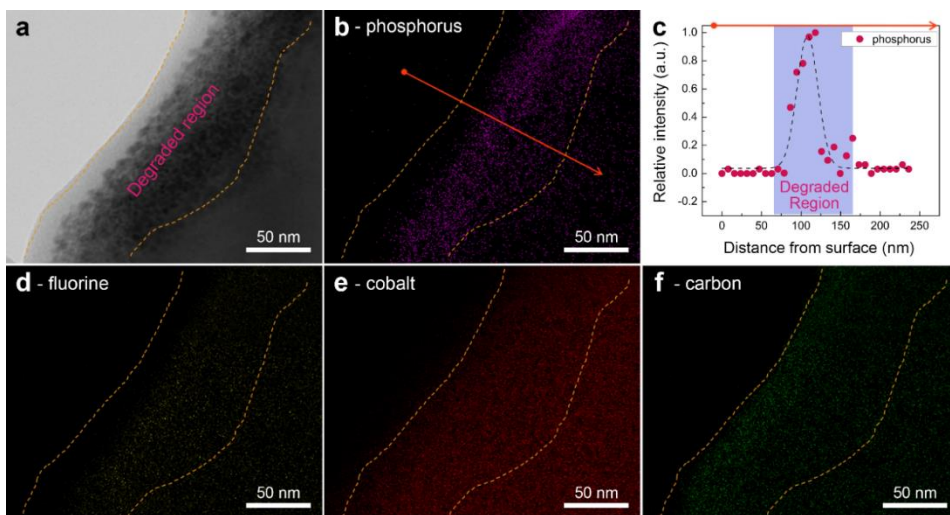


Figure 2.3.18. (a) STEM image of surface region of charged Li_xCoO_2 with thermal history. The samples were prepared directly after the potential of the Li/LiCoO_2 half-cell decreased to ~ 3.3 V. Elemental mapping across the dashed line in (a) for (b) P, (d) F, (e) Co, and (f) C of Li_xCoO_2 surface after storage at 60°C and self-discharge. (c) EDS line profile of phosphorus across degraded region and bulk Li_xCoO_2 , as indicated by red arrow in (b). The orange dashed lines in (a)–(b) and (d)–(f) mark the same positions in each figure to guide the eye.

2.3.3. The origin of internal parasite at surface

XPS depth-profiling analysis was performed to further understand the degraded region by comparing the surfaces of Li_xCoO_2 without and with a thermal history of $60\text{ }^\circ\text{C}$ (**Figures 2.3.19a** and **2.3.19b**, respectively). In **Figures 2.3.19**, the cobalt ions were observed to be close to the trivalent state for each sample, while it was difficult to discern $\text{Li}_{0.9}\text{CoO}_2$ and LiCoO_2 with the shift of Co $2p$ spectrum^{43,44}. However, in the outermost surface region, the peaks shifted to a lower binding energy, indicating the reduction of cobalt ions to less than the trivalent state for the pristine Li_xCoO_2 in **Figure 2.3.19a**. The reduction of the Li_xCoO_2 surface has been generally attributed to oxidation of the solvent in the electrolyte during the electrochemical cycle, which agrees with a previous report²⁹. In contrast, much less reduction of the cobalt was detected in the sample with the thermal history, as shown in **Figure 2.3.19b**. The smaller shift of the cobalt peak implies a slight oxidation reaction during the thermal treatment of the sample. It should be noted that the observed surface oxidation agrees with our speculation that the LiPF_6 salt in the electrolyte acts as an oxidizing agent during the short heating, and then it reduces into Li_3P -containing byproducts. The emergence of phosphorous in the electrode after the thermal treatment was confirmed by the P $2p$ XPS spectra in **Figure 2.3.19b**, where a peak at $\sim 134\text{ eV}$ assigned to P–O bonding is observable on the surface^{33,45}. This result matches well with that from the elemental mapping of the degraded region of Li_xCoO_2 in **Figure 2.3.18**.

The role of the phosphorous layer as an internal parasite could be determined using a similar self-discharge experiment with a phosphorus-free electrolyte. We assembled new sets of $\text{Li}/\text{Li}_x\text{CoO}_2$ half cells with 1 M of LiClO_4 salt dissolved in EC/DMC (1:1 v/v) instead of LiPF_6 and compared the self-discharge rate between

heated and pristine cells. While the use of LiClO_4 salt in practical batteries is not common due to its explosive^{46,47}, **Figure 2.3.20** shows that the self-discharge was not accelerated by the high-temperature storage. This finding indicates that the presence of phosphorus in the electrolyte is critical in triggering the self-discharge, where the formation of Li_3P serves as the parasitic lithium source in the chemical lithiation of the cathode. In addition, the selection of the salt and nature of its byproducts are important in preventing the self-discharge of the lithium cells at elevated temperature. Although several previous works have reported various byproducts on the surface of the active material from electrolytes²⁷⁻²⁹, this observation emphasizes the need for careful and systematic studies to subdue the self-discharge induced by them.

Based on all the observations, a possible self-discharge route with the thermal history is schematically proposed in **Figure 2.3.21**. When the LiCoO_2 electrode is electrochemically cycled under normal conditions, a typical SEI layer containing the organic compounds is generally formed, which is expected to induce a negligible amount of lithium influx to the charged Li_xCoO_2 at room temperature (**Figure 2.3.21** above). However, when stored at elevated temperature, the surface layer of the electrode undergoes partial oxidation with the phosphorous-containing salts and produces a lithium-rich phosphide such as Li_3P . Because the lithium chemical potential is generally higher in Li_3P than in the Li_xCoO_2 cathode, the lithium influx to the cathode through the chemical lithiation occurs and the lithium-rich phosphide would continuously supply lithium ions to the charged Li_xCoO_2 leading to accelerated self-discharge with extended time at rest even at room temperature. Furthermore, a larger contact area between the nanoparticles and the damaged Li_xCoO_2 surface would contribute to an increased supply rate of lithium, further accelerating the self-discharge (**Figure 2.3.21** below). Within this scenario,

one of the important questions to be addressed is whether the formation of the lithium-rich phosphide on the cathode surface is sufficient to result in noticeable self-discharge. We thus roughly estimated the amount of Li_3P required for self-discharge of typical micrometer-sized Li_xCoO_2 . Based on the SEM observation in **Figure 2.2.1b**, we assumed that the shape of the Li_xCoO_2 particle was a perfect sphere with an average diameter of 2 μm . This assumption renders the radius of the sphere 1 μm , simplifying our calculation. Here, we suggest the situation that lithium inserted into the Li_xCoO_2 sphere is provided by the surface film composed of only Li_3P . Using densities of 5.06 and 1.44 g/cm^3 and molecular masses of 97.87 and 51.80 g/mol for LiCoO_2 and Li_3P ^{48,49}, respectively, we calculated the amounts of these materials per cubic centimeter to be 52 and 28 mmol, respectively. Based on our suggestion for the route of self-discharge expressed in Equation (1), Li_3P can be considered to provide 2 Li per unit chemical formula. Therefore, Li_xCoO_2 occupies 52 mmol of lithium sites and Li_3P provides 56 mmol of lithium per cubic centimeter. Thus, for the same volume, Li_3P has ~ 1.08 times the number of lithium sites of those in Li_xCoO_2 . In addition, for this simple calculation, we make the assumption that the size of the Li_xCoO_2 sphere does not change even when the thermal history transforms its surface into a Li_3P thin film, as shown in **Figure 2.3.22**.

For the Li_3P film to fully lithiate the charged Li_xCoO_2 , the number of lithium sites provided by the Li_3P film should be more than that in the Li_xCoO_2 bulk. Therefore, we can calculate the minimum number of lithium sites in the Li_3P film for chemical lithiation of Li_xCoO_2 as follows:

$$(\text{Number of Li sites in unit } \text{Li}_x\text{CoO}_2) = (\text{Number of Li sites provided by unit } \text{Li}_3\text{P})$$

Because we already calculated that the number of lithium sites per unit volume in Li_3P is 1.08 times that in Li_xCoO_2 , the above equation can be written as

$$(1 - x) \times (\text{Volume of Li}_x\text{CoO}_2) = 1.08 \times (\text{Volume of Li}_3\text{P}).$$

Thus, the thickness of the Li₃P film, a , can be calculated as follows:

$$(1 - x) \times \frac{4}{3} \times \pi \times (1 \mu\text{m})^3 = 1.08 \times \frac{4}{3} \times \pi \times \left(((a + 1)\mu\text{m})^3 - (1 \mu\text{m})^3 \right).$$

In each SOC, we can input the corresponding x and find a by solving the cubic equation above. Thus, when Li _{x} CoO₂ is charged to $x=0.9$, a is calculated to be ~ 0.030 , corresponding to a thickness of only 30 nm. Even when Li _{x} CoO₂ is charged to $x=0.5$, representing the broadly known limit of charge for reversible operation of a secondary battery composed of this material, a is calculated to be ~ 0.135 , corresponding to a thickness of 135 nm. These results strongly support the notion that even a slight detrimental reaction between Li _{x} CoO₂ and the electrolyte during a short period of heating can induce severe acceleration of the self-discharge. When summarized, it can be said that the thickness of the surface film composed of Li₃P required for chemically inserting 0.1 Li into a 2 μm Li_{0.9}CoO₂ particle was determined to be only ~ 30 nm. Furthermore, the film thickness required to fully lithiate the charged Li_{0.5}CoO₂ (\sim SOC 90) is ~ 135 nm. This result supports the idea that a lithium-rich phosphide film with a thickness of only several tens of nanometers can sufficiently induce the accelerated self-discharge of Li _{x} CoO₂.

It is rational that the surface modification of electrode materials along with the modification of salts (or additives) can influence/reduce the ‘internal parasite’ formed at the surface region of active material triggered by the oxidative reaction of LiPF₆ salt in electrolyte; our proposed cause of the abnormal self-discharge. Indeed, it is well known that various battery company manufactures utilize different coating materials, coating morphologies, electrolyte additives to enhance the performance of conventional LIBs. And, we believe that these various coating conditions would

result in different self-discharge behaviors upon thermal history if rigorously investigated, while the investigation of them is beyond the scope of our study. Nevertheless, it is emphasized that this sort of the fundamental study focusing on the pristine electrode material regardless of various coatings that different companies may employ conveys a message that one should take into account of the potential parasitic surface reactions in considering the electrode design, which can seriously lead to the self-discharge upon thermal history. Moreover, LIBs in new applications will experience more and more harsh environments than ever, and the validity of such simple surface treatment process can be highly doubted in a long-term usage of LIBs at extreme surroundings. Chen *et al.* has pointed out that the sustainability of thin or rough coating on cathode material for an extended period of time should be carefully investigated⁵⁰. Especially, LiCoO_2 as well as high-Ni $\text{Li}(\text{Ni},\text{Co},\text{Mn})\text{O}_2$ cathode material has been known to suffer from the generation of microcracks during the operation for a prolonged period, which can induce new direct contact between electrolyte and bare active material^{51,52}. For instance, as shown in **Figure 2.3.23**, our synthesized LiCoO_2 also showed prominent microcracks after 50 cycles of charge/discharge at harsh 4.8 V-cycling. Under this condition, ‘fresh’ active material interface can be easily exposed to the electrolyte in spite of the pre-surface treatment, and the possibility of occurring abnormal self-discharge may not be negligible. This kind of unwanted surface degradation is expected to be more frequent, when LIBs are to be operated with wider voltage range and higher output energy density at fluctuating outdoor conditions for the extended period.

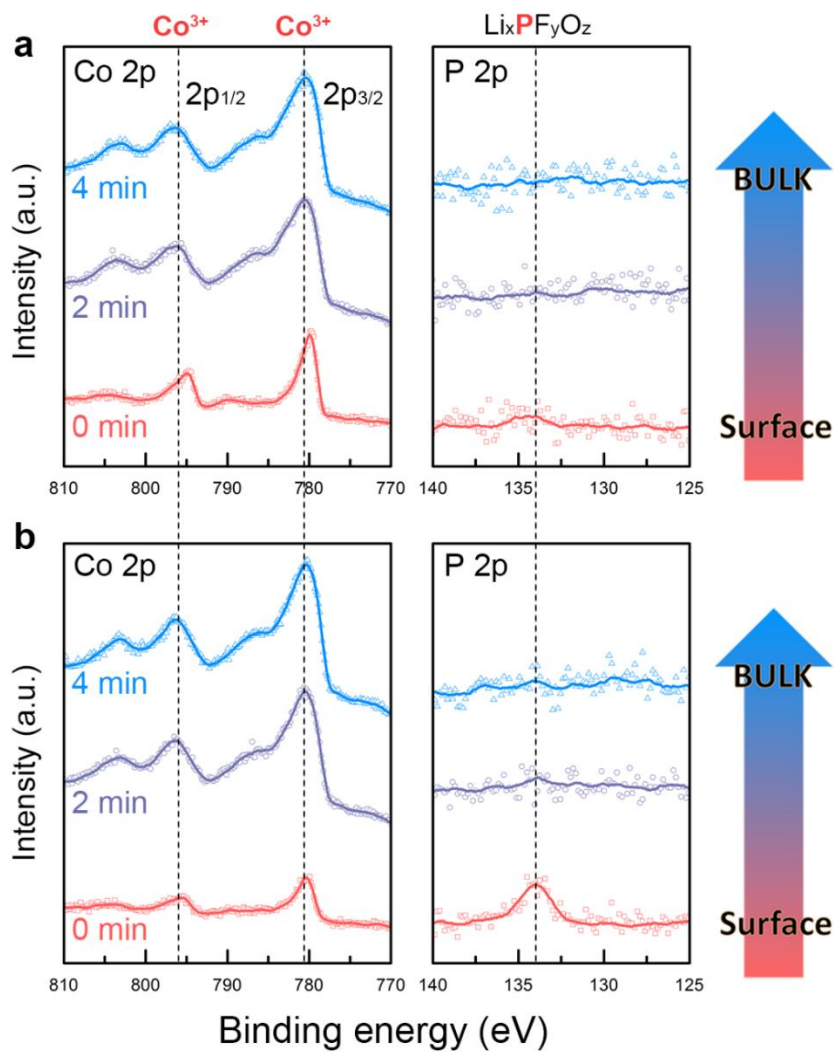


Figure 2.3.19. XPS depth profile of Li_xCoO_2 electrode (a) without thermal history and (b) with thermal history at 60 °C. All the samples were charged to SOC 20 and analyzed after the self-discharge was complete. The sputtering time is indicated underneath each spectrum.

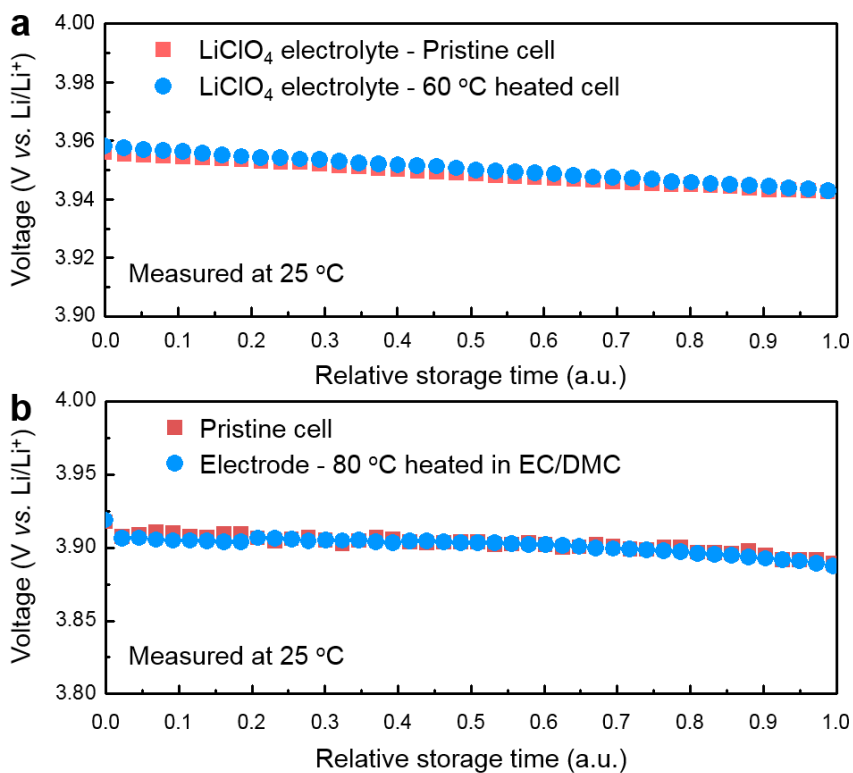


Figure 2.3.20. (a) Comparison of self-discharge rate of bare LiCoO₂ and LiCoO₂ with 60 °C thermal history using electrolyte of 1 M LiClO₄ in EC/DMC (1:1 v/v). (b) Comparison of self-discharge rate of bare LiCoO₂ and LiCoO₂ with thermal history consisting of soaking the cathode electrode in EC/DMC (1:1 v/v) solvent without salt at 80 °C. The self-discharge rate in (b) was measured using 1 M LiPF₆ in EC/DMC (1:1 v/v) electrolyte.

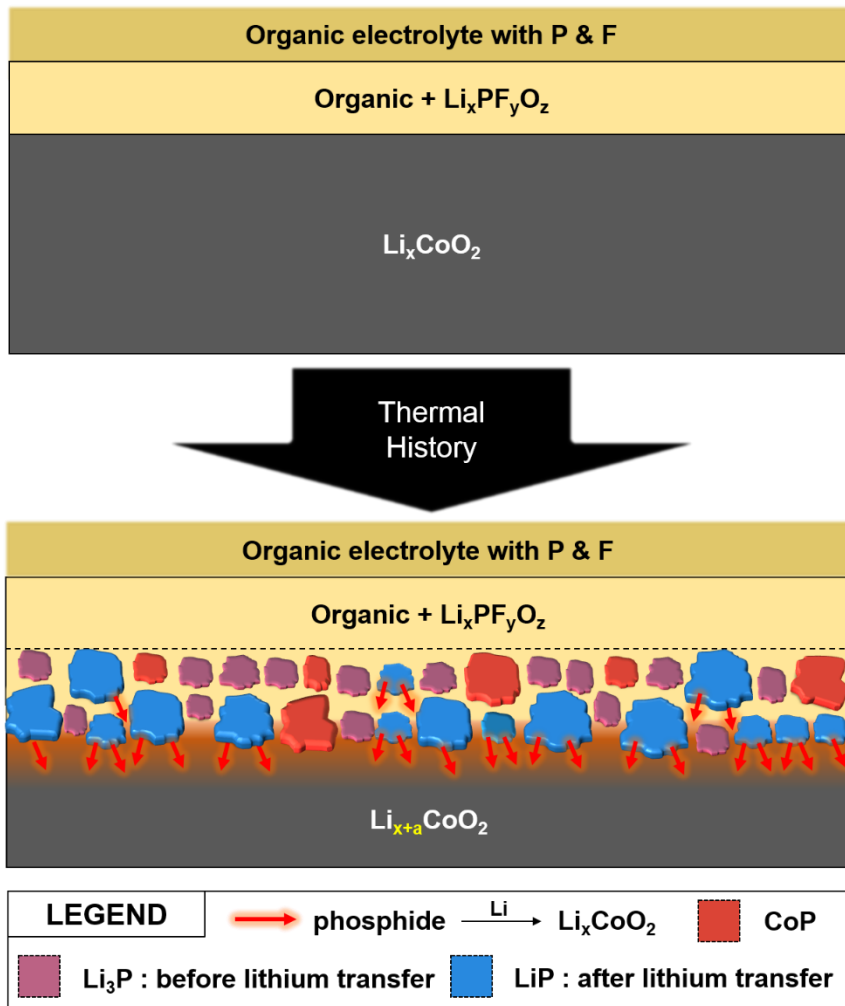


Figure 2.3.21. Schematic illustration of proposed mechanism for accelerated self-discharge rate based on the written thermal history at the surface of Li_xCoO_2 .

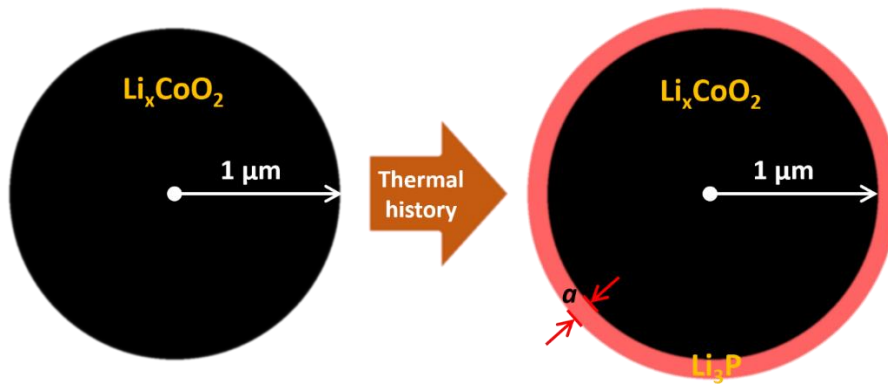


Figure 2.3.22. Simplified model for calculation of required Li_3P film thickness (a in the sphere right side) for chemical lithiation of charged sphere Li_xCoO_2 with radius of $1\ \mu\text{m}$.

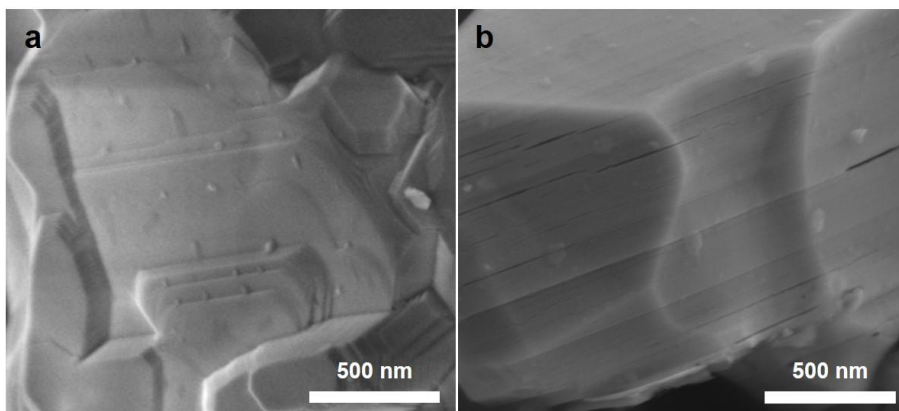


Figure 2.3.23. SEM image of surface of (a) pristine LiCoO₂ and (b) LiCoO₂ cycled at 4.8 V-cut off for 50 cycles.

2.4. Conclusion

We demonstrated that the lithium-ion cell, which has been regarded as the system with the lowest self-discharge among rechargeable batteries, can suffer from abnormally accelerated self-discharge with thermal exposure. Even with exposure to 60 °C or 80 °C for a short period, the lithium-ion cell operation at room temperature is critically affected with respect to the self-discharge. It was revealed that the lithium-rich phosphide (such as Li_3P) that forms as a result of the thermal history serves as a parasitic lithium source, inducing chemical lithiation of the cathode. Moreover, a thin layer of Li_3P with only a few tens of nanometer thickness was sufficient for the self-discharge of an entire micrometer-size Li_xCoO_2 particle because of the large amount of lithium in the Li_3P phase and the higher lithium chemical potential. As the formation of the parasitic lithium source is attributed to the side reactions occurring at the interface with electrolyte salts, the importance of controlling the surface of the cathode material to suppress this unwanted abnormal self-discharge and properly selecting electrolyte salts is emphasized. The self-discharge of lithium-ion batteries has remained largely ignored; however, our findings suggest that careful consideration should be paid to the self-discharge of lithium-ion batteries applied for large-scale ESSs, as, unlike mobile electronic devices, they would be exposed to various outdoor temperature conditions.

2.5. References

1. C. Liu, F. Li, L.-P. Ma and H.-M. Cheng, *Adv. Mater.*, 2010, **22**, E28-62.
2. B. Dunn, H. Kamath and J.-M. Tarascon, *Science*, 2011, **334**, 928-935.
3. D. Larcher and J. M. Tarascon, *Nat Chem*, 2015, **7**, 19-29.
4. M. R. Palacín and A. de Guibert, *Science*, 2016, **351**.
5. A. H. Zimmerman, *IEEE Aerospace and Electronic Systems Magazine*, 2004, **19**, 1924.
6. S. H. Choi, J. Kim and Y. S. Yoon, *J. Power Sources*, 2004, **138**, 283-287.
7. N. N. Sinha, A. J. Smith, J. C. Burns, G. Jain, K. W. Eberman, E. Scott, J. P. Gardner and J. R. Dahn, *J. Electrochem. Soc.*, 2011, **158**, A1194-A1201.
8. X. Liao, Q. Huang, S. Mai, X. Wang, M. Xu, L. Xing, Y. Liao and W. Li, *J. Power Sources*, 2014, **272**, 501-507.
9. J. Li, L. Xing, L. Zhang, L. Yu, W. Fan, M. Xu and W. Li, *J. Power Sources*, 2016, **324**, 17-25.
10. Y. J. Kim, J. Cho, T.-J. Kim and B. Park, *J. Electrochem. Soc.*, 2003, **150**, A1723-A1725.
11. E. Markevich, G. Salitra and D. Aurbach, *Electrochem. Commun.*, 2005, **7**, 1298-1304.
12. H. Gabrisch, R. Yazami and B. Fultz, *J. Electrochem. Soc.*, 2004, **151**, A891-A897.
13. S. K. Jung, H. Gwon, J. Hong, K. Y. Park, D. H. Seo, H. Kim, J. Hyun, W. Yang and K. Kang, *Adv. Energy Mater.*, 2014, **4**.
14. G. Nagasubramanian and D. Doughty, *J. Power Sources*, 2001, **96**, 29-32.
15. N. Kularatna, *IEEE Instrumentation & Measurement Magazine*, 2011, **14**, 20-33.

16. L. Lu, X. Han, J. Li, J. Hua and M. Ouyang, *J. Power Sources*, 2013, **226**, 272-288.
17. W. Li, B. L. Lucht, *J. Electrochem. Soc.*, 2006, **153**, A1617-A1625.
18. M.-T. F. Rodrigues, G. Babu, H. Gullapalli, K. Kalaga, F. N. Sayed, K. Kato, J. Joyner and P. M. Ajayan, *Nat. Energy*, 2017, **2**, 17108.
19. R. Genieser, S. Ferrari, M. Loveridge, S. D. Beattie, R. Beanland, H. Amari, G. West, R. Bhagat, *J. Power Sources*, 2018, **373**, 172-183.
20. V. Muenzel, M. Brazil, I. Mareels, J. Hoog, D. A. Thomas, IEEE 2013 Tencon - Spring, 2013, 470-474.
21. T. Ohzuku and A. Ueda, *J. Electrochem. Soc.*, 1994, **141**, 2972-2977.
22. J. Akimoto, Y. Gotoh and Y. Oosawa, *J. Solid State Chem.*, 1998, **141**, 298-302.
23. J. Li, J. Zhang, X. Zhang, C. Yang, N. Xu and B. Xia, *Electrochim. Acta*, 2010, **55**, 927-934.
24. K. -Y. Park, I. Park, H. Kim, G. Yoon, H. Gwon, Y. Cho, Y. S. Yun, J. -J. Kim, S. Lee, D. Ahn, Y. Kim, H. Kim, I. Hwang, W. -S. Yoon and K. Kang, *Energy Environ. Sci.*, 2016, **9**, 2902-2915.
25. H. Liu, F. C. Strobridge, O. J. Borkiewicz, K. M. Wiaderek, K. W. Chapman, P. J. Chupas, C. P. Grey, *Science*, 2014, **344**, 1252817.
26. M. Ménétrier, I. Saadoune, S. Levasseur and C. Delmas, *J. Mater. Chem.*, 1999, **9**, 1135-1140.
27. Z. Wang, X. Huang and L. Chen, *J. Electrochem. Soc.*, 2004, **151**, A1641-A1652.
28. Y. Gu, D. Chen and X. Jiao, *The Journal of Physical Chemistry B*, 2005, **109**, 17901-17906.
29. D. Takamatsu, Y. Koyama, Y. Orikasa, S. Mori, T. Nakatsutsumi, T.

- Hirano, H. Tanida, H. Arai, Y. Uchimoto and Z. Ogumi, *Angew. Chem. Int. Ed.*, 2012, **51**, 11597-11601.
30. D. Yang, J. Zhu, X. Rui, H. Tan, R. Cai, H. E. Hoster, D. Y. Yu, H. H. Hng and Q. Yan, *ACS Appl. Mater. Interfaces*, 2013, **5**, 1093-1099.
31. J. Yang, Y. Zhang, C. Sun, H. Liu, L. Li, W. Si, W. Huang, Q. Yan and X. Dong, *Nano Research*, 2016, **9**, 612-621.
32. A. Jain, S. P. Ong, G. Hautier, W. Chen, W. D. Richards, S. Dacek, S. Cholia, D. Gunter, D. Skinner, G. Ceder and K. A. Persson, *APL Materials*, 2013, **1**, 011002.
33. G. G. Eshetu, T. Diemant, S. Grugeon, R. J. Behm, S. Laruelle, M. Armand and S. Passerini, *ACS Appl. Mater. Interfaces*, 2016, **8**, 16087-16100.
34. G. A. Nazri, R. A. Conell and C. Julien, *Solid State Ionics*, 1996, **86**, 99-105.
35. Y. Gu, D. Chen and X. Jiao, *J. Phys. Chem. B*, 2005, **109**, 17901-17906.
36. Y. Takanashi, Y. Orikasa, M. Mogi, M. Oishi, H. Murayama, K. Sato, H. Yamashige, D. Takamatsu, T. Fujimoto, H. Tanida, H. Arai, T. Ohta, E. Matsubara, Y. Uchimoto and Z. Ogumi, *J. Power Sources*, 2011, **196**, 10679-10685.
37. H. Yang, G. V. Zhuang and P. N. Ross Jr., *J. Power Sources*, 2006, **161**, 573-579.
38. P. Andersson, P. Blomqvist, A. Loren and F. Larsson, *Fire Mater.*, 2016, **40**, 999-1015.
39. C. H. Choi, S. H. Park and S. I. Woo, *J. Mater. Chem.*, 2012, **22**, 12107-12115.
40. M. C. Lopez, G. F. Ortiz and J. L. Tirado, *J. Electrochem. Soc.*, 2012, **159**, A1253-A1261.
41. H. Lee, C. Wan and Y. Wang, *J. Electrochem. Soc.*, 2004, **151**, A542-A547.
42. J. Zheng, H. Zheng, R. Wang, L. Ben, W. Lu, L. Chen, L. Chen and H. Li, *Phys. Chem. Chem. Phys.*, 2014, **16**, 13229-13238.

43. M. Oku, *J. Solid State Chem.*, 1978, **23**, 177-185.
44. J. C. Dupin, D. Gonbeau, H. Benqlilou-Moudden, P. Vinatier and A. Levasseur, *Thin Solid Films*, 2001, **384**, 23-32.
45. Y.-C. Lu, A. N. Mansour, N. Yabuuchi and Y. Shao-Horn, *Chem. Mater.*, 2009, **21**, 4408-4424.
46. C. M. Olson, *J. Electrochem. Soc.*, 1969, **116**, 33C-35C.
47. H. Vogt, J. Balej, J. E. Bennett, P. Wintzer, S. A. Sheikh, P. Gallone, S. Vasudevan and K. Pelin, in *Ullmann's Encyclopedia of Industrial Chemistry*, Wiley-VCH Verlag GmbH & Co. KGaA, 2000, DOI: 10.1002/14356007.a06_483.pub2.
48. *LiCoO₂ Crystal Structure: Datasheet from "PAULING FILE Multinaries Edition – 2012" in SpringerMaterials (http://materials.springer.com/isp/crystallographic/docs/sd_0554601)*, Springer-Verlag Berlin Heidelberg & Material Phases Data System (MPDS), Switzerland & National Institute for Materials Science (NIMS), Japan.
49. *Li₃P Crystal Structure: Datasheet from "PAULING FILE Multinaries Edition – 2012" in SpringerMaterials (http://materials.springer.com/isp/crystallographic/docs/sd_0458524)*, Springer-Verlag Berlin Heidelberg & Material Phases Data System (MPDS), Switzerland & National Institute for Materials Science (NIMS), Japan.
50. Z. Chen, Y. Qin, K. Amine and Y.-K. Sun, *J. Mater. Chem.*, 2010, **20**, 7606-7612.
51. H. Wang, Y.-I. Jang, B. Huang, D. R. Sadoway and Y.-M. Chiang, *J. Electrochem. Soc.*, 1999, **146**, 473-480.
52. W. Liu, P. Oh, X. Liu, M.-J. Lee, W. Cho, S. Chae, Y. Kim and J. Cho, *Angew. Chem. Int. Ed.*, 2015, **54**, 4440-4457.

Chapter 3. Unveiling the intrinsic cycle reversibility of a LiCoO₂ electrode at 4.8-V cut-off voltage through subtractive surface modification for lithium-ion batteries

(The content of this chapter has been published in *Nano Letters*. Reproduced with permission from W. M. Seong *et al.* Unveiling the intrinsic cycle reversibility of a LiCoO₂ electrode at 4.8-V cut-off voltage through subtractive surface modification for lithium-ion batteries. *Nano Lett.*, **2018**, *Online published*. Copyright 2018, American Chemical Society.)

3.1. Introduction

Electric vehicles (EVs) are expected to progressively replace vehicles with combustion engines and represent a significant portion of the vehicle market in the future. This trend places lithium-ion batteries (LIBs), the most promising battery system for electrifying vehicles, at the center of worldwide interest¹⁻³. However, most affordable EVs currently provide a shorter driving range than that offered by conventional engines and a charging time of more than several hours⁴⁻⁶, which creates a high demand for LIBs with even higher energy density and rate capability. As a critical step toward advanced LIBs, the development of high-energy density cathodes is pivotal. Various new cathode materials such as LiNi_xMn_yCo_{1-x-y}O₂ and Li-rich layered oxides have been explored^{5,7-9} and implemented in state-of-the-art LIBs. However, LiCoO₂ is still the most widely adopted cathode material for LIBs in modern consumer electronics¹⁰ and remains one of the most attractive options for

batteries in EVs because of its high redox potential (~ 3.9 V vs. Li/Li⁺)¹¹⁻¹³, large theoretical capacity, and high electronic conductivity ($> \sim 10^{-4}$ S cm⁻¹) among layered-type cathode materials¹⁴⁻¹⁵ as well as its high tap density (4.1–4.3 g cm⁻³) and large-scale synthetic capability¹⁶.

Since the discovery of LiCoO₂ as a promising electrode material¹⁷, however, the full utilization of the lithium from LiCoO₂ has been far from that achieved in practice as it causes rapid cycle degradation. In addition, only a fraction of lithium can be electrochemically cycled by restricting the usable state-of-charge (SOC) limit. The practical specific capacity limit of a bare LiCoO₂ electrode is known to be ~ 140 mAh/g, corresponding to only ~ 0.5 Li^{5, 18}. Therefore, efforts to fully utilize the near theoretical capacity of LiCoO₂ have been extensively made, pushing the cut-off voltage higher by applying surface coatings or doping and adding suitable electrolyte additives^{14, 19-26}. Nevertheless, the current practical upper cut-off voltage and corresponding specific capacity are commonly limited to ~ 4.45 V (vs. Li/Li⁺) and ~ 180 mAh/g (corresponding to ~ 0.65 Li), respectively²⁷⁻²⁸. The fundamental reason behind this restriction is that the pristine layered crystal is unstable when more than half of the lithium is extracted, which causes an irreversible phase transformation²⁹⁻³¹. The inherent instability of LiCoO₂ at highly delithiated states has been shown to be typically triggered by side reactions with the electrolyte, followed by propagation of the degraded phase into the bulk³²⁻³⁵. Furthermore, the phase transition toward the O1 phase that appears with the extended delithiation of Li_xCoO₂ has been believed to be the most disruptive phase transition involving a large change in the lattice parameters, which induces electrochemical grinding and is thus only partially reversible³⁶⁻⁴¹.

Various attempts have been made in the past decades to stabilize the structure and suppress the phase transformation by altering the intrinsic properties of LiCoO₂,

i.e., by varying the stacking sequence of the layered structure such as in O2-type LiCoO_2 ⁴² or through partial substitution of Co with other transition metals such as Ni, Mn and Al^{5, 12, 43-45}, which have led to some remarkable enhancements in the specific capacity. However, these improvements are inevitably accompanied by substantial costs such as a lower redox potential, inferior tap density, or lower electrical conductivity. Surface modification of LiCoO_2 particles has also been shown to significantly extend the usable SOC range^{19-20, 23}. In the most recent works involving surface coatings^{22, 39, 46}, operation of a LiCoO_2 electrode at a cut-off voltage of >4.5 V (vs. Li/Li^+) has been shown to be feasible with appropriate coatings, with specific capacities of >180 mAh/g. Yano *et al.* reported that alumina-coated LiCoO_2 electrodes can deliver prolonged cycling capability at a cut-off voltage of 4.7 V (vs. Li/Li^+)³⁹, where the bulk structure was unexpectedly preserved except for mechanical cracks after cycling. This finding naturally raises questions about how the simple surface modification suppresses the bulk phase transformation governed by the intrinsic instability of Li_xCoO_2 ($x < 0.5$) and the extent to which surface protection of LiCoO_2 is 'effective'. To answer these questions, we herein could manage to decouple the factors related to the bulk and surface that contribute to the capacity fade, *i.e.*, the effects of the (i) intrinsic instability of highly delithiated LiCoO_2 and (ii) surface degradation at high voltages on the cycling stability.

We begin with the unforeseen observation that the electrochemical cycling of an uncoated LiCoO_2 electrode at a cut-off voltage of 4.8 V yielded superior capacity retention compared with that for the 4.6-V cut-off condition. Moreover, the voltage hysteresis between charge and discharge was observed to be substantially smaller for a cut-off voltage of 4.8 V than for one of 4.6 V. Considering the more severe driving force for the irreversible phase transformation of delithiated LiCoO_2 phase at higher voltage cut-offs, this finding contradicts with expectations. Our experimental

investigations here reveal that highly resistive surface layers consisting of nano-domains of the spinel phase are continuously formed during high-voltage cycling, which typically leads to rapid cycle degradation, particularly with 4.6-V cut-offs. In contrast, it is shown that an abnormally clean surface is retained after 4.8-V cycling. This unexpected observation is elucidated with the ‘subtractive’ surface modification occurring above a certain potential. It is further demonstrated that the instability of the crystalline Li_xCoO_2 ($x < 0.5$) has a limited effect on the cycle stability. This report sheds new light on the high-voltage cycling of LiCoO_2 electrode and indicates that suppression of the formation of the resistive layer is a necessary step for improved cycle stability either through additive or subtractive surface modification.

3.2. Experimental section

3.2.1. Synthesis and characterization of pristine LiCoO₂ powder

LiCoO₂ powder was synthesized *via* a conventional solid-state reaction⁴⁷⁻⁴⁸. Stoichiometric amounts of Li₂CO₃ (98%, Aldrich) and Co₃O₄ (71.0–74.0 wt% cobalt, Aldrich) were mixed by wet ball-milling using anhydrous ethanol for 24 h. The mixture was then dried at 120 °C for 12 h, heated at 600 °C for 12 h, re-ground, and re-heated at 900 °C for 24 h in air. After the heat treatment at 900 °C, the sample was slowly cooled and maintained at 200 °C before being transferred to an argon-filled glove box (exposure time at room temperature < 30 s). This process was used to minimize the exposure of the LiCoO₂ powder to atmospheric moisture. The crystal structure of LiCoO₂ was characterized using high-resolution powder diffraction (HRPD) with a synchrotron X-ray source (9B-HRPD beamline at the Pohang Light Source (PLS-II), Korea). The LiCoO₂ crystal structure was determined to be the α -NaFeO₂-type structure with $R\bar{3}m$ space group with lattice parameters of $a = 2.815$ Å and $c = 14.06$ Å (the Rietveld refinement results of the HRPD pattern are provided in **Figure 3.2.1a**), which are in good agreement with previously reported values⁴⁹⁻⁵⁰. Based on scanning electron microscopy (SEM; SUPRA 55VP, Carl Zeiss) analysis, the LiCoO₂ secondary particles were determined to be approximately 1–5 μm in size and composed of smaller primary particles with spherical morphology (**Figure 3.2.1b**).

3.2.2. Electrochemical analyses

LiCoO₂ powder, super P carbon black, and polyvinylidene fluoride (PVDF) were mixed in a weight ratio of 92:4:4 and added to *N*-methyl-2-pyrrolidone (NMP, anhydrous, 99.5%, Aldrich) for the electrode preparation. After this mixture was homogenized into a slurry, it was applied onto aluminum foil using the doctor-blade method, dried under vacuum overnight, and pressed by a roll-presser. Coin-type half cells (CR2032, Wellcos) were assembled using the composite electrode, a lithium metal counter electrode, a glass microfiber filter (grade GF/F, Whatman) as a separator, and 1 M LiPF₆ in ethylene carbonate/dimethyl carbonate (EC/DMC, 1:1 v/v, PanaX Etec) as the electrolyte. The water content in the electrolyte was measured to be less than 10 ppm using Karl–Fisher titration measurements. All the preparation processes were performed in an argon-filled glove box. Galvanostatic measurements of the charge/discharge of the Li/LiCoO₂ cells were conducted within the voltage range between a lower cut-off of 3.0 V and higher cut-offs of desired voltages (from 4.3 to 4.9 V) with a current density of 27 mA/g at 25 °C using a multichannel potentiogalvanostat (WBCS-3000, Wonatech, Korea). A rest step for 10 min was applied between every charge and discharge process. In cyclic voltammetry experiments, the voltage of the Li/LiCoO₂ cell was swept forward and backward repeatedly at a rate of 0.06 mV/s. Electrochemical impedance spectroscopy (EIS) analysis was performed after the Li/LiCoO₂ cell was charged to a desired upper voltage limit at each cycle number. A sine-modulated AC potential of 10 mV was applied in the frequency range of 200 kHz to 5 mHz.

3.2.3. Characterizations of Li_xCoO₂ electrodes after electrochemical test

After the electrochemical cycles, each coin cell was disassembled, and the composite cathode was retrieved and gently rinsed with DMC solution to perform additional

characterizations. The crystal structure of the retrieved electrode was analyzed using transmission electron microscopy (TEM; JEM-2100F, JEOL) and X-ray diffraction (XRD; D2 PHASER, Bruker). Chemical information for the surface was obtained using X-ray photoelectron spectroscopy (XPS; PHI 5000 VersaProbe, ULVAC-PHI). To minimize damage to the samples, especially those with organic surface films, which can be vulnerable to the electron beam, the acceleration voltage was set to 120 kV in the TEM observation. The cobalt dissolution behavior of the retrieved electrode was evaluated using inductively coupled plasma mass spectroscopy (ICP-MS; NexION 350D, Perkin-Elmer).

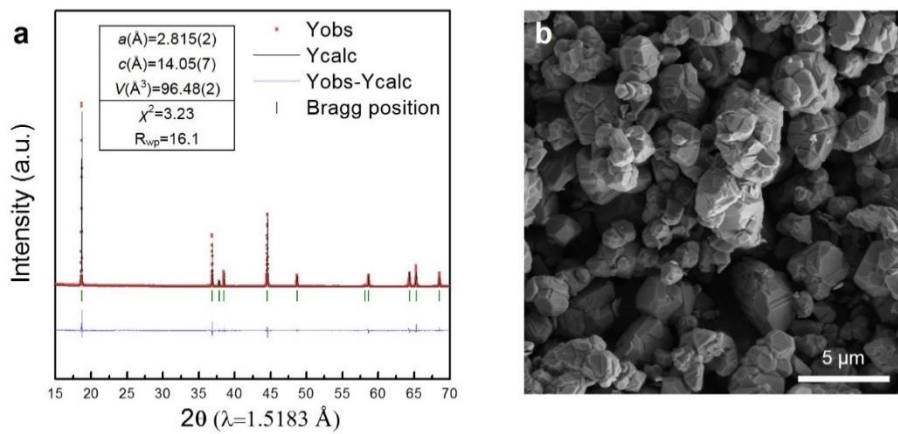


Figure 3.2.1. (a) Rietveld refinement results of HRPD pattern of synthesized LiCoO_2 .
(b) SEM image of synthesized LiCoO_2 powder.

3.3. Results and discussion

3.3.1. Inspiration: unexpected superior cyclability of LiCoO₂ electrode at 4.8-V cut-off compared with 4.6-V cut-off

Preliminary investigations on the phase evolution of LiCoO₂ at high delithiation states were first conducted to examine the validity of our samples. **Figure 3.3.1** shows that LiCoO₂ charged to 4.6 V contained both pristine O3 and H1-3 phases, indicating the occurrence of a phase transition from O3 to H1-3. Further charging to 4.8 V induced the disappearance of the O3 phase with a continuous peak shift for the H1-3 phase and the emergence of the O1 phase. These results confirm that our LiCoO₂ sample followed the typical phase transition behavior of O3→H1-3→O1 phases during the delithiation, which is consistent with that observed in previous works^{41, 51}. The detailed phase evolution as a function of voltage is shown in **Figure 3.3.2**. It should be noted that sliding of O–Co–O slabs in the layered structure accompanies these transitions and that the appearance of the O1 phase is considered a cause of the irreversible degradation of the pristine LiCoO₂ structure³⁶⁻⁴¹. Nevertheless, we observed that electrochemical cycling under these two cut-off conditions led to results that were opposite to the conventional belief. **Figure 3.3.3** presents the voltage profiles of Li/LiCoO₂ cells as a function of cycle number, which were operated under the same conditions except for the upper cut-off voltages, which were 4.6 and 4.8 V. With increasing cycle number, the voltage hysteresis between the charge and discharge was drastically amplified for the 4.6 V cut-off and the discharge capacity rapidly decreased from 218.6 to 131.8 mAh/g (~60 % of the initial capacity). However, the 4.8-V cut-off cycling resulted in a reasonably low voltage hysteresis after a short increase during the initial 10 cycles, which was maintained

stably for the subsequent cycles. Accordingly, the retention of the discharge capacity for the 4.8-V cut-off was significantly higher, ~73 % (175.5 mAh/g) of the initial capacity, than that for the 4.6-V cut-off. This finding was also confirmed by equivalent cyclic voltammetry experiments. **Figure 3.3.4** shows that the gap between the anodic and cathodic peaks rapidly increased during the 4.6-V cycling, whereas it was stably maintained after the initial several cycles for the 4.8-V cycling. The cycle stabilities for these two conditions with respect to the capacity retention and energy efficiency are compared in **Figure 3.3.5a** and **3.3.5b**, respectively. The superior capacity retention for the 4.8-V cut-off is clearly demonstrated in **Figure 3.3.5a**; 4.8-V cycling resulted in steady retention after the initial 10 cycles, whereas the capacity rapidly decreased for the 4.6-V cycling. In addition, **Figure 3.3.5b** shows that the energy efficiency, *i.e.*, the ratio of the output to input energy, after 50 cycles for the 4.8-V cut-off was 90.7%, which is almost the same as that for the initial cycles. In contrast, the energy efficiency for the 4.6-V cycling rapidly dropped to 76.3% because of the growing polarization. These behaviors were further supported by a series of identical tests for other cut-off voltages between 4.3 and 4.9 V and the detailed results for these additional tests are presented in **Figure 3.3.6**. As a result, we could comparatively display the capacity retentions and energy efficiencies after 50 cycles for various upper cut-off conditions in **Figure 3.3.7**. Notably, deterioration of both properties was observed with increasing cut-off voltages up to 4.6 V (*vs.* Li/Li⁺), which is consistent with previous results and expectations; however, the properties slightly recovered starting from 4.7 V with the best performances achieved near 4.8 V, followed by reduced stability at 4.9 V. This performance dependence on the upper cut-off voltages does not agree with the belief that LiCoO₂ electrodes in higher SOC operations would be simply subject to more severe degradation of the bulk and surface structures^{22, 25, 38-39}.

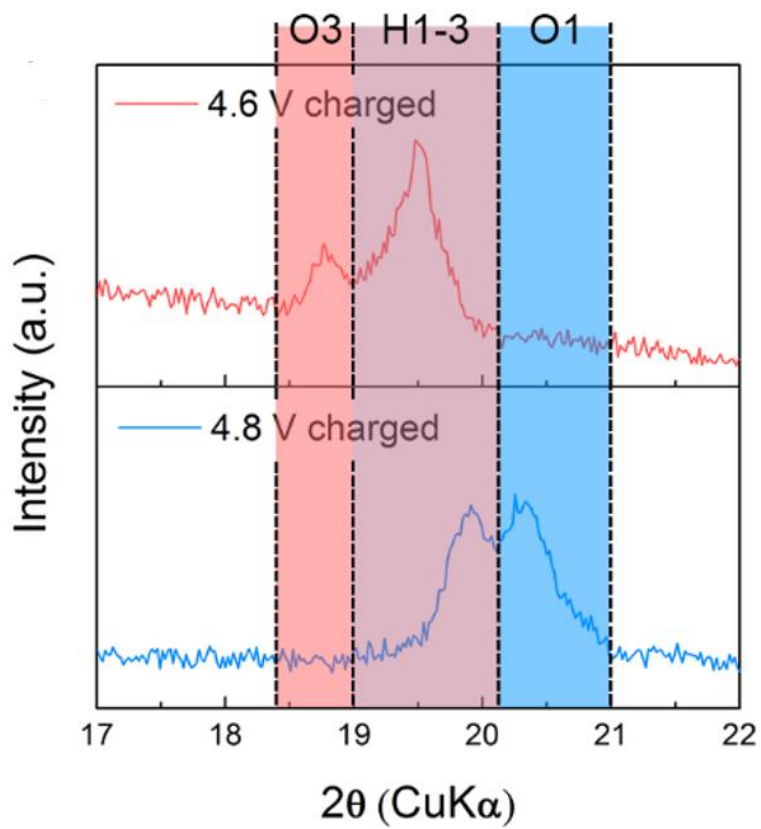


Figure 3.3.1. XRD patterns of Li_xCoO_2 electrodes after charging to desired cut-off voltage.

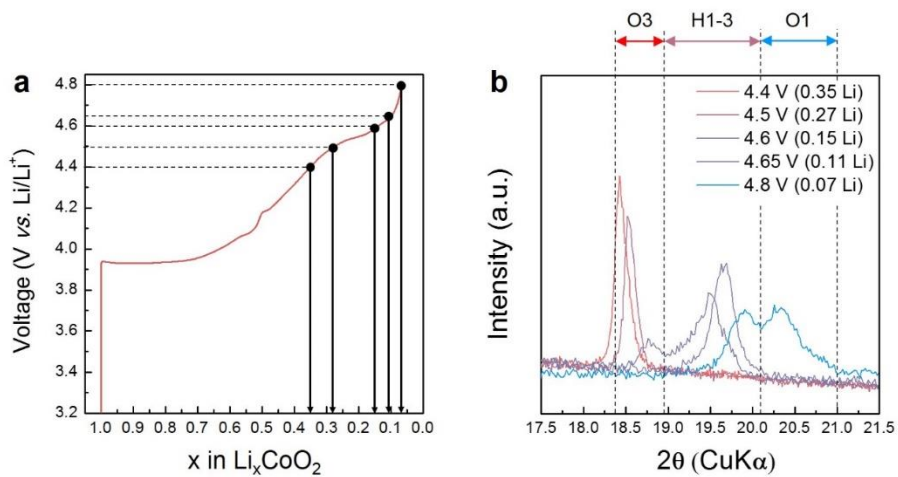


Figure 3.3.2. (a) Representative voltage-SOC profile of Li_xCoO₂. (b) Ex-situ XRD pattern of Li_xCoO₂ electrodes charged to desired SOC indicated in graph.

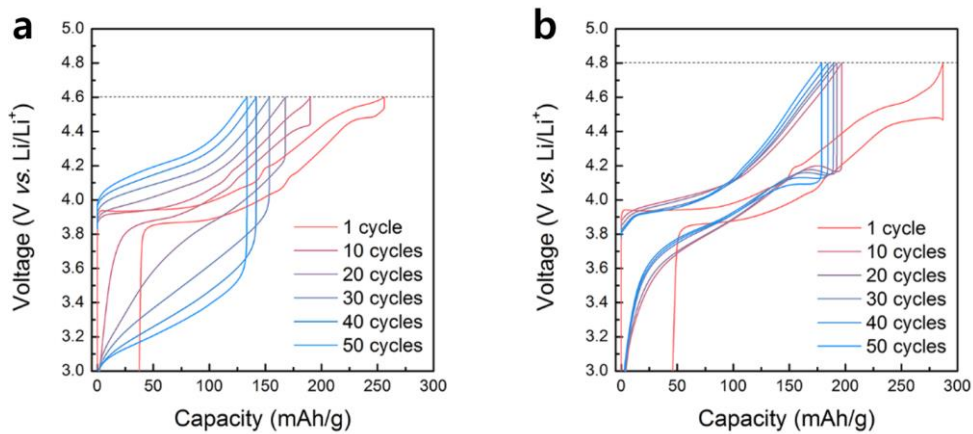


Figure 3.3.3. Galvanostatic charge/discharge profiles of Li/LiCoO₂ cell for upper cut-off voltage of (a) 4.6 and (b) 4.8 V. Applied current density is 27 mA g⁻¹

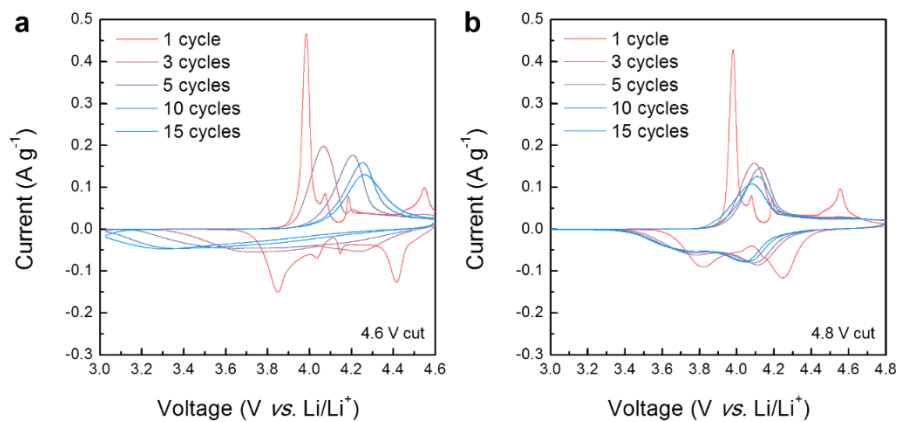


Figure 3.3.4. Cyclic voltammetry results of Li/LiCoO₂ cell for cycling at (a) 4.6-V and (b) 4.8-V cut-off potentials. The scan rate is 0.06 mV s⁻¹.

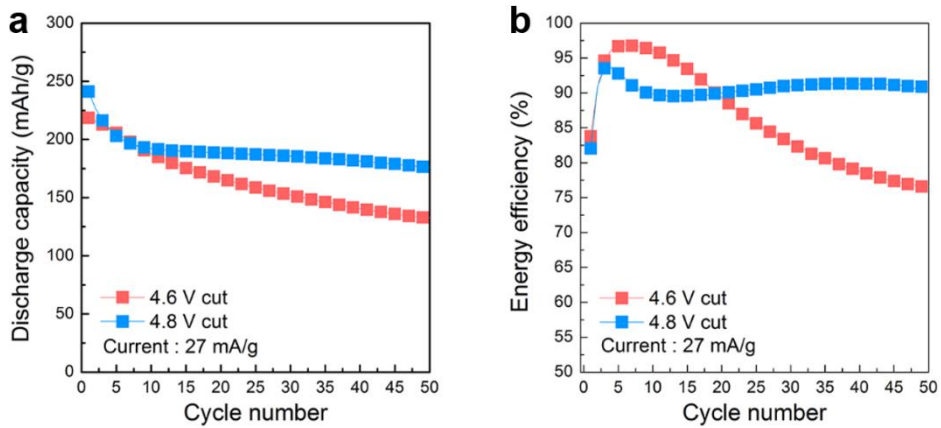


Figure 3.3.5. Change of (a) specific discharge capacity and (b) energy efficiency of Li/LiCoO₂ cell as electrochemical cycling proceeds.

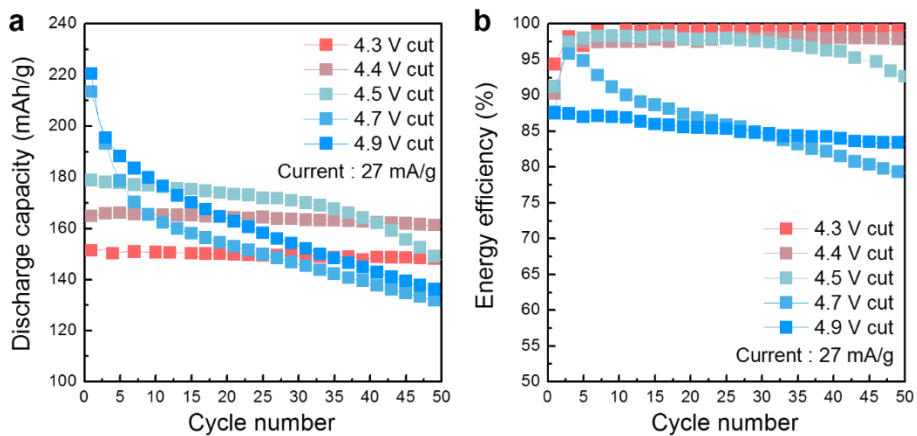


Figure 3.3.6. (a) Discharge capacity retention and (b) energy efficiency of Li/Li_xCoO₂ cells for electrochemical cycling at various upper potential cut-offs.

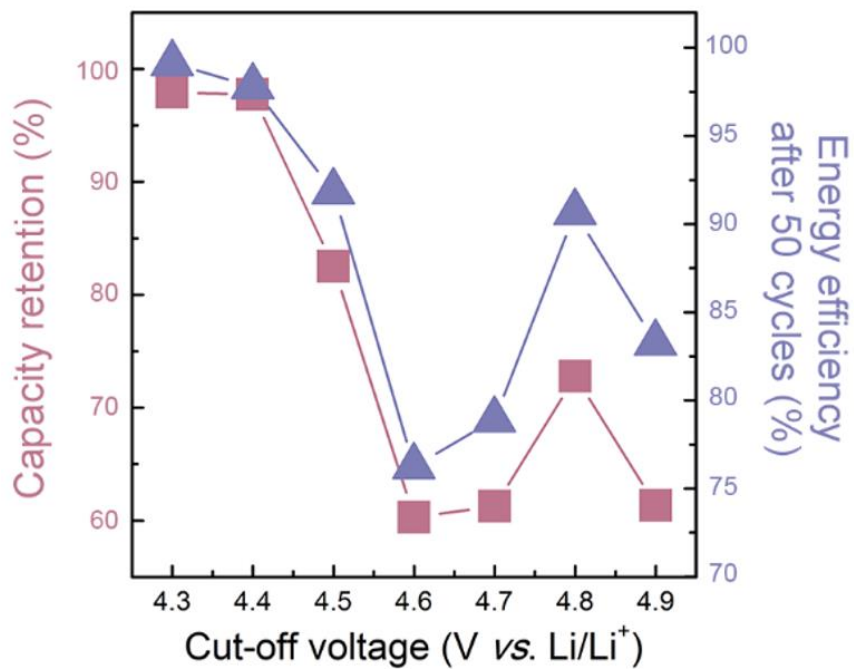


Figure 3.3.7. Summary of capacity retention of Li/LiCoO₂ cells at various upper cut-off voltages.

3.3.2. Mitigated surface construction: the origin of superior cyclability of LiCoO₂ at 4.8-V cut-off

To elucidate this unexpected behavior, the electrodes after cycling under respective conditions were carefully examined, and the changes in the bulk and surface structure were probed. The bulk analysis of the samples using XRD indicated that the overall layered structures were retained after cycling regardless of the cut-off voltages. However, **Figure 3.3.8** shows that the (003) main peaks of the two discharged electrodes after 50 cycles were broader than that for the pristine state. We suspect that this broadening can be partly attributed to the incomplete electrode reaction and the accumulated strain by slab sliding, which also could be supported by the presence of microcracks, as observed by SEM (**Figure 3.3.9**). The (003) peaks were asymmetric for the cycled LiCoO₂ electrodes, notably for the 4.6-V-cycled sample, containing more than one peak that could be deconvoluted (**Figure 3.3.10**). This finding indicates that the 4.6-V-cycled Li_xCoO₂ electrode at 3 V could not be fully discharged, with some regions remaining as high SOC states. Thus, we attempted to fully discharge the 4.6-V-cycled sample by forcibly maintaining its voltage at 3 V after cycling. As shown in **Figure 3.3.11**, the (003) peak became almost identical to that of the 4.8-V-cycled sample after full discharge. It indicates that the difference in the performance of the two electrodes may not originate from the crystalline structural aspects involving the irreversible transition but may instead be related to the sluggish kinetics in the 4.6-V-cycled electrode.

The sluggish electrode reactions with 4.6-V cycling compared with 4.8-V cycling upon extended cycling was also supported by the galvanostatic intermittent titration technique (GITT) measurements shown in **Figure 3.3.12a** and **3.3.12b**. Although the degree of polarization was almost the same regardless of the cut-off

voltages for the initial cycle, 4.6-V cycling induced faster growth of the polarization with increasing cycle number, implying the accelerated formation of ionic or electronic insulating components in the electrode. This finding is also consistent with the *in situ* EIS measurements for the two electrodes shown in **Figure 3.3.13a** and **3.3.13b**. The Nyquist plots obtained for each charge ends reveal that the semi-circle from the middle-to-low-frequency range (180 Hz to 5 mHz) grew faster as the cycling proceeded for the 4.6-V cut-off compared with that for the 4.8-V cut-off. The size of the semi-circle for 4.6-V cycling was smaller for the initial cycle; however, it exceeded that for the 4.8-V cycling after 20 cycles. Although the precise assignment of each semi-circle is not trivial, the semi-circles for middle-to-low-frequency regions have often been attributed to the surface charge-transfer resistance of the LiCoO₂ electrode⁵²⁻⁵³. In addition, these indicate that the surface charge-transfer kinetics are better maintained with 4.8-V cycling than with 4.6-V cycling, which contrasts with the expectedly more severe degradation of the surface structure of the electrode at high voltages⁵⁴⁻⁵⁵.

To understand this distinct change in the electrochemical performance, the nature of surface films on the electrodes after respective cycles was investigated using XPS from the outermost surface (0 nm) to the sub-surface region (20 nm) with bombardment of argon ions. The O 1s spectra are presented in **Figure 3.3.14a** and **3.3.14b** for the electrodes after 4.6-V and 4.8-V cycling, respectively. The surfaces of both electrodes were composed of typical organic byproducts originating from the electrolyte decomposition and surface impurities. However, according to the depth profiling, the film thickness of these surface byproducts differed negligibly for the two electrodes, suggesting that the formation of additional byproduct films is not likely the origin of their distinct surface properties. Additionally, we evaluated other elements, including cobalt, carbon, fluorine, and lithium, to further probe the surface;

however, we could not find any significant differences between the two electrodes (**Figure 3.3.15**).

The atomistic surface structures of discharged LiCoO₂ particles after cycling were further examined using high-resolution TEM (HRTEM). At first, pristine LiCoO₂ particle was observed by TEM, and also selected area electron diffraction (SAED) pattern of it was obtained for comparison, which shows pure layered structure with *R-3m* space group (**Figure 3.3.16**). Then it was compared with crystal structure of LiCoO₂ particle after cycling at 4.6- and 4.8-V cut-offs whose TEM images are shown in **Figure 3.3.17a** and **3.3.17d** respectively; the corresponding selected area electron diffraction (SAED) patterns are presented in **Figure 3.3.17b** and **3.3.17e**, respectively. The ordered diffraction spots confirm that the pristine layered structure was maintained for both particles even after prolonged cycling under harsh conditions. These result are also in accordance with the XRD patterns in **Figure 3.3.8** and **Figure 3.3.18** showing the preserved *R-3m* LiCoO₂ crystal structure. However, small diffraction spots that could not be observed in the XRD patterns were also universally identified, as indicated by the red circle in the SAED pattern. The *d*-spacing of the crystallographic plane corresponding to this diffraction spot (~2.8 Å) matched that of (220) planes of the disordered spinel Li₂Co₂O₄ phase^{32, 34}. When the objective aperture was positioned to obtain dark-field TEM images attributed to this spot, the corresponding phase was observed to be mostly populated on the region near the surface, as shown in **Figure 3.3.17c** and **3.3.17f** for the 4.6- and 4.8-V-cycled particles, respectively. It is noteworthy that this phase was observed to be substantially wider in the sub-surface region of the 4.6-V-cycled particle (**Figure 3.3.17c**) than in that of the 4.8-V-cycled particle (**Figure 3.3.17f**). As the surface reconstruction layer composed of Li₂Co₂O₄ phase is known to be resistive and typically formed on the electrochemically degraded LiCoO₂ surface³²,

³⁴, it is consistent with our results that the 4.6-V cycling was accompanied by a greater increase in the impedance which is related to surface charge-transfer kinetics.

Closer investigation of the TEM images in **Figure 3.3.19a** and **3.3.19b** also confirmed the thicker surface reconstruction layer for the 4.6-V-cycled electrode. Moreover, the surface of the 4.6-V-cycled particle could be divided into different regions on the basis of the constituents. Whereas the pristine *R-3m* LiCoO₂ phase was retained in the bulk region (region 3 in **Figure 3.3.19a**), as shown in **Figure 3.3.19e**, the surface with approximately 50–100-nm thickness was severely damaged, exposing two morphologically and chemically distinct layers. In the ~50-nm sub-surface region close to the bulk (region 2 in **Figure 3.3.19a**), nanoparticulate domains densely appeared in the crystalline matrix, as illustrated in **Figure 3.3.19d**. Fast Fourier transformation (FFT) of this region revealed that the main phases were Li₂Co₂O₄, which is consistent with the SAED findings. However, moving closer to the outermost surface with ~50-nm thickness (region 1 in **Figure 3.3.19a**), the nanoparticulate morphology became dominant, and the nanoparticles appeared to be severely etched. For this outermost surface region, the FFT results in **Figure 3.3.19c** suggest that randomly oriented Co₃O₄ particles are mainly distributed. On the contrary, it was found that the surface of the 4.8-V-cycled particles remained relatively undamaged, which means the mitigation of surface reconstruction of LiCoO₂. Exhaustive examinations of the 4.8-V-cycled particle proposed that an almost clean surface with the *R-3m* LiCoO₂ phase was maintained from the bulk to the near-surface region, as shown in **Figure 3.3.19b** and **3.3.19f**. To confirm this observation, we carefully examined many other particles with different histories of 4.6- and 4.8-V cycling, which presented the identical trend. That is, the surface of the 4.6-V-cycled electrode was damaged and transformed into surface reconstruction layers of nanoparticulate Co₃O₄ and Li₂Co₂O₄ phases, whereas that of the 4.8-V-

cycled electrode remained relatively undamaged (**Figure 3.3.20**). This finding indicates that the formation and/or deposition of the surface reconstruction layer of LiCoO_2 was suppressed during 4.8-V cycling, as opposed to 4.6-V cycling.

It is known that the spinel phase can be generated on the surface of LiCoO_2 through an oxidation reaction with the electrolyte at high SOC states^{35, 39, 54} as mentioned in **Chapter 1.3.1**. Moreover, the formation of highly symmetric metal oxides, such as the rock-salt phase, can be induced on the outermost surface of electrode particles with extended high-voltage cycling, as reported for LiNiO_2 ⁵⁶ and $\text{LiNi}_{0.5}\text{Co}_{0.3}\text{Mn}_{0.2}\text{O}_2$ ⁵⁷. In this respect, it can be inferred that during the high-voltage electrochemical cycling, the surface LiCoO_2 degrades into disordered spinel $\text{Li}_2\text{Co}_2\text{O}_4$, which is followed by the formation of the Co_3O_4 phase upon severe extended oxidative damage, which may account for the morphological evolution of the 4.6-V-cycled electrode.

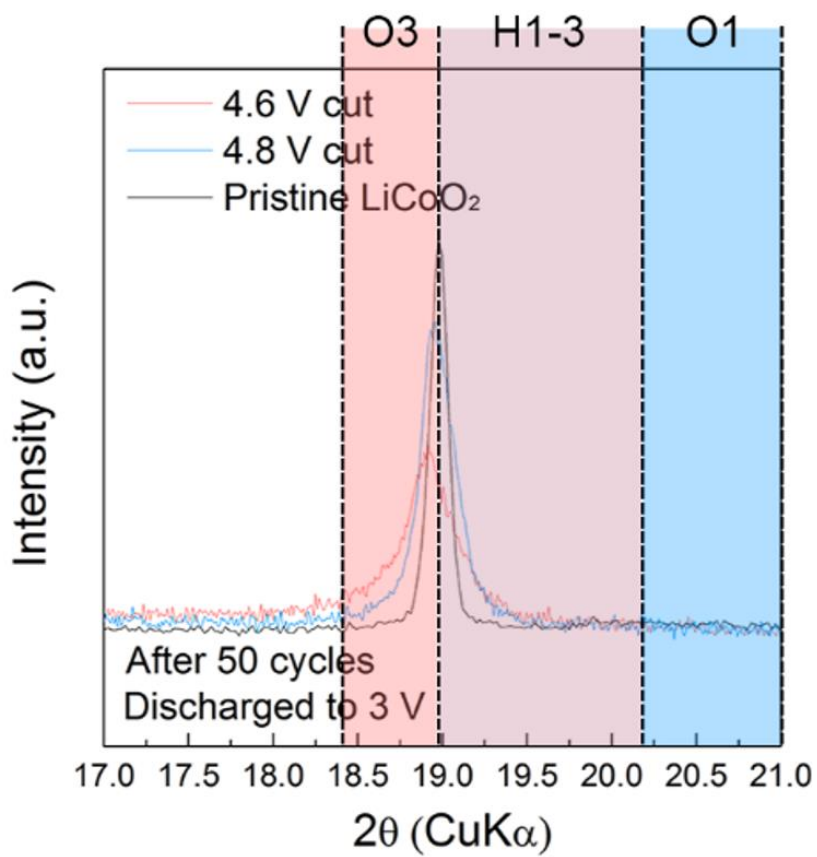


Figure 3.3.8. XRD patterns of discharged Li_xCoO_2 electrodes after 50 cycles at 4.6- and 4.8-V cut-offs.

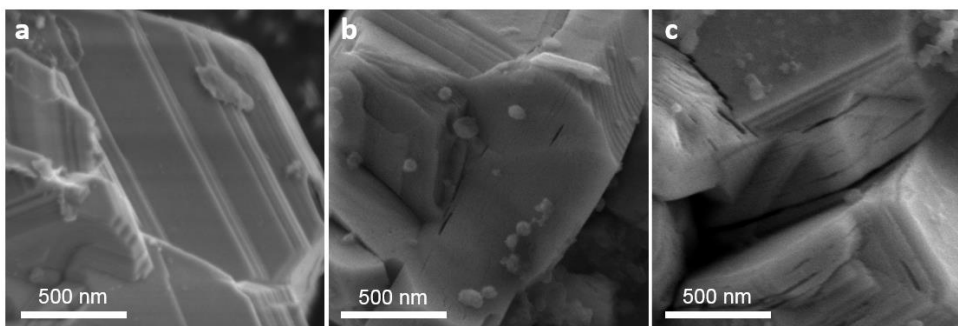


Figure 3.3.9. SEM images of (a) pristine LiCoO₂, (b) LiCoO₂ electrode cycled in 3.0–4.6 V range, and (c) LiCoO₂ electrode cycled in 3.0–4.8 V range.

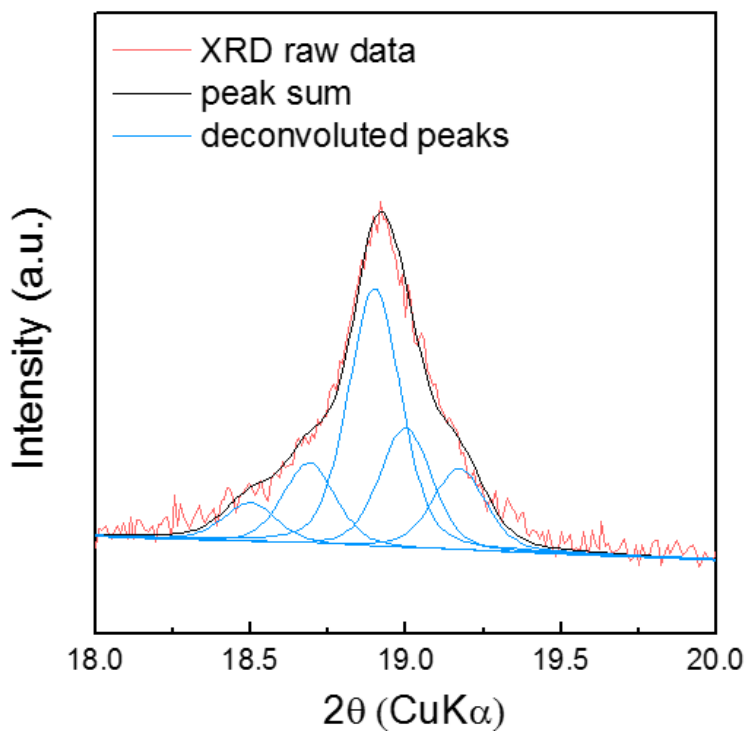


Figure 3.3.10. Deconvolution result of (003) plane XRD peak showing that this peak is composed of more than one peak. For deconvolution, the full width at half maximum (FWHM) was fixed at 0.2° , which is the same as that for the pristine LiCoO_2 (003) peak in **Figure 3.3.8**.

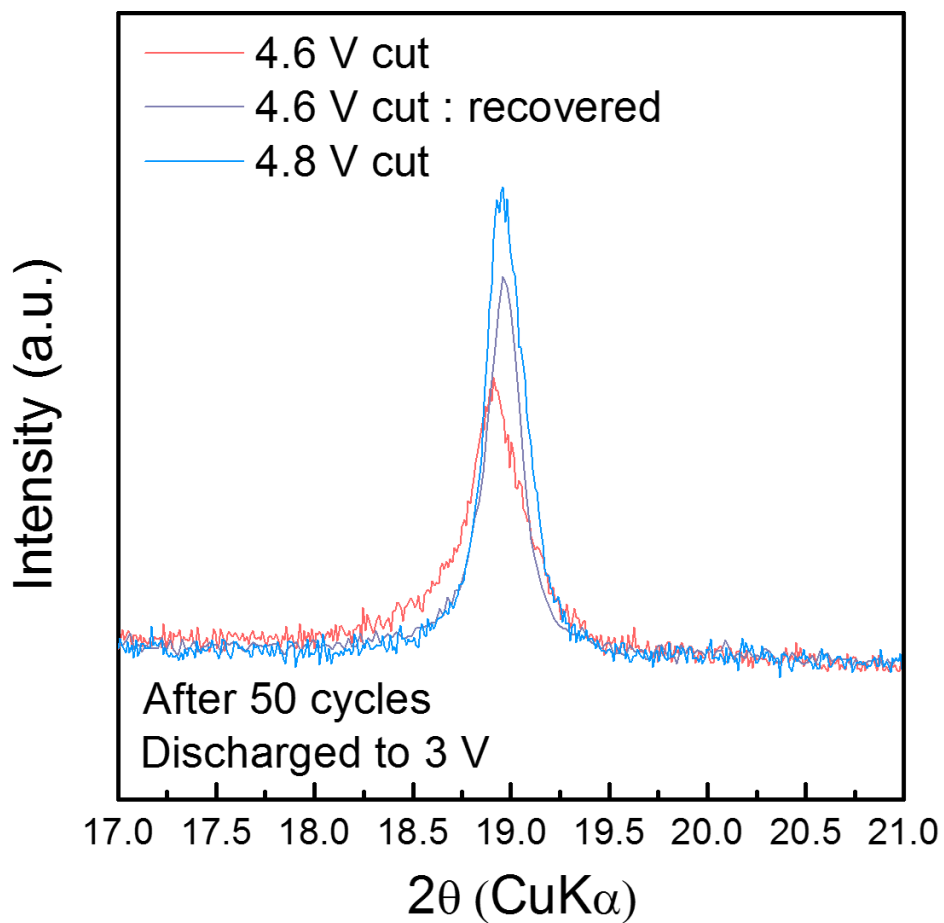


Figure 3.3.11. XRD pattern of Li_xCoO_2 obtained by maintaining its voltage at 3 V (vs. Li/Li^+) for 12 h after 50 cycles of 4.6-V cycling (indicated as ‘4.6 V cut: recovered’), which shows the recovery of its (003) peak broadness to that for 4.8-V cycling.

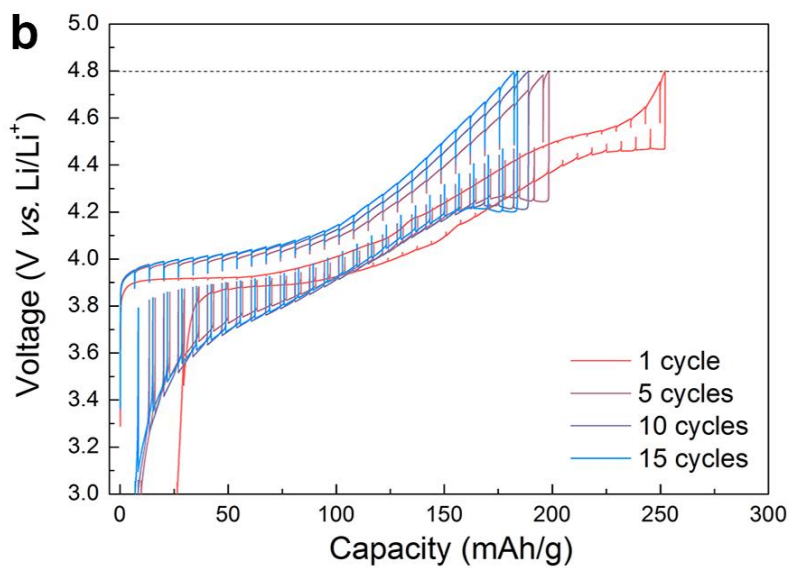
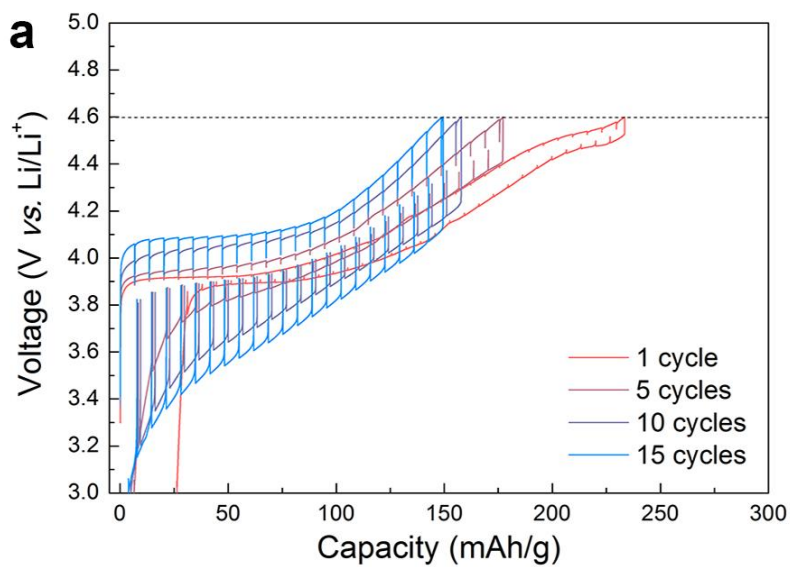


Figure 3.3.12. GITT measurements for Li/LiCoO₂ cell for (a) 4.6- and (b) 4.8-V cycling.

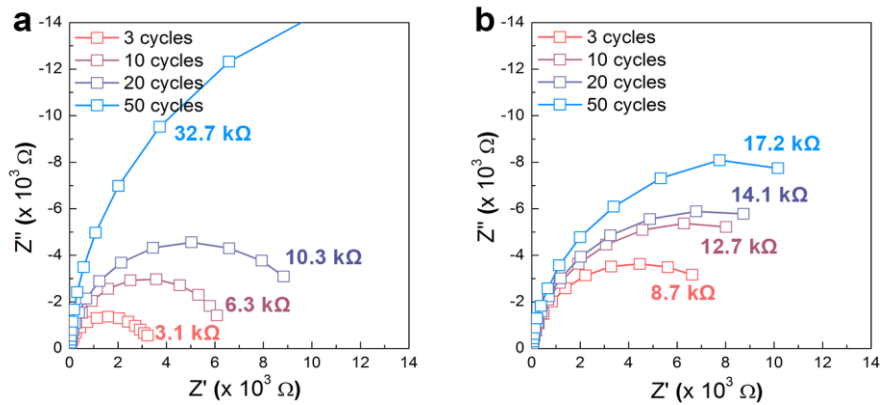


Figure 3.3.13. Nyquist plots from *in situ* EIS measurement results for upper voltage limit of (d) 4.6 and (e) 4.8 V. For each semi-circle, the corresponding charge-transfer resistance (R_{ct}) value is shown.

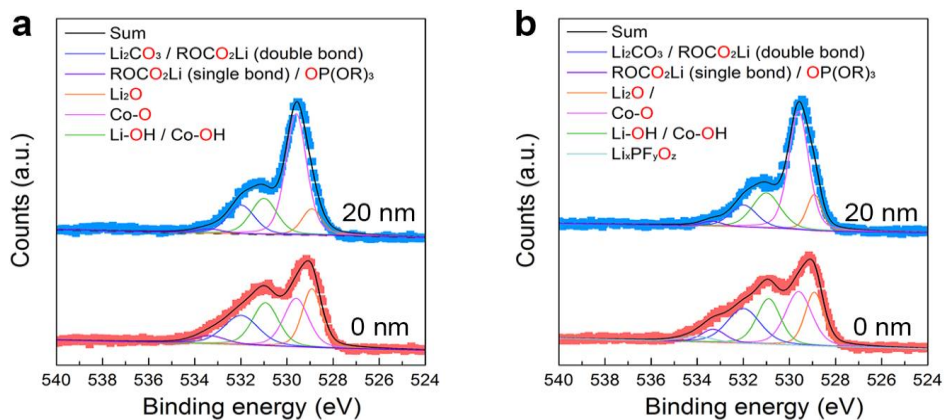


Figure 3.3.14. XPS results from O 1s spectra of (a) 4.6- and (b) 4.8-V-cycled LiCoO_2 , which show both the outermost surface (0 nm) and etched surface (20 nm). In the legend, the oxygen atoms that form the chemical bonds corresponding to each deconvoluted XPS peak are highlighted in red in the molecular formula.

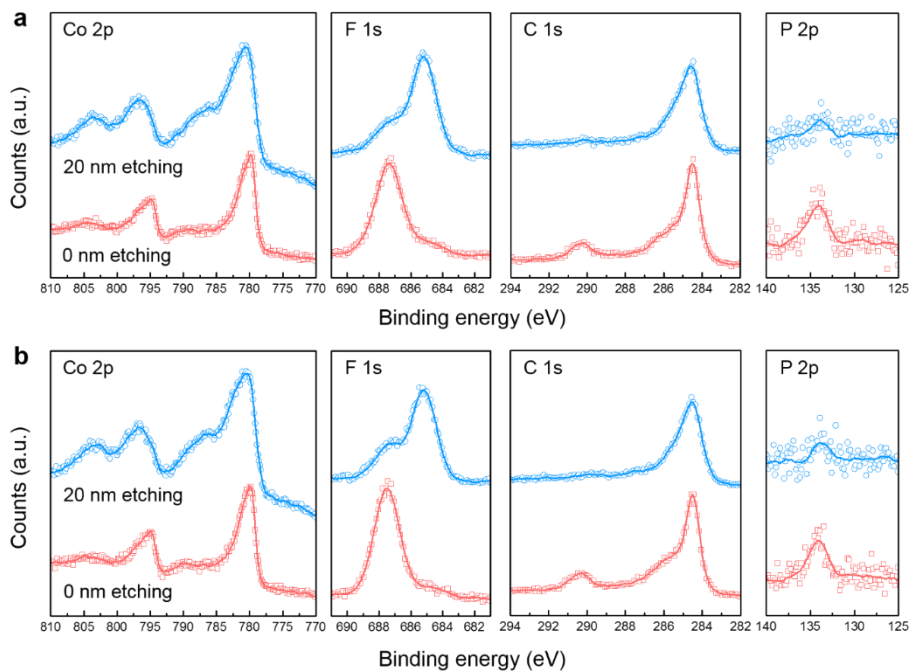


Figure 3.3.15. XPS spectra for Co 2p, F 1s, C 1s, and P 2p photoelectrons from (a) 4.6-V-cycled Li_xCoO_2 and (b) 4.8-V-cycled Li_xCoO_2 . The spectra were obtained before and after Ar-ion etching, as indicated in the graph.

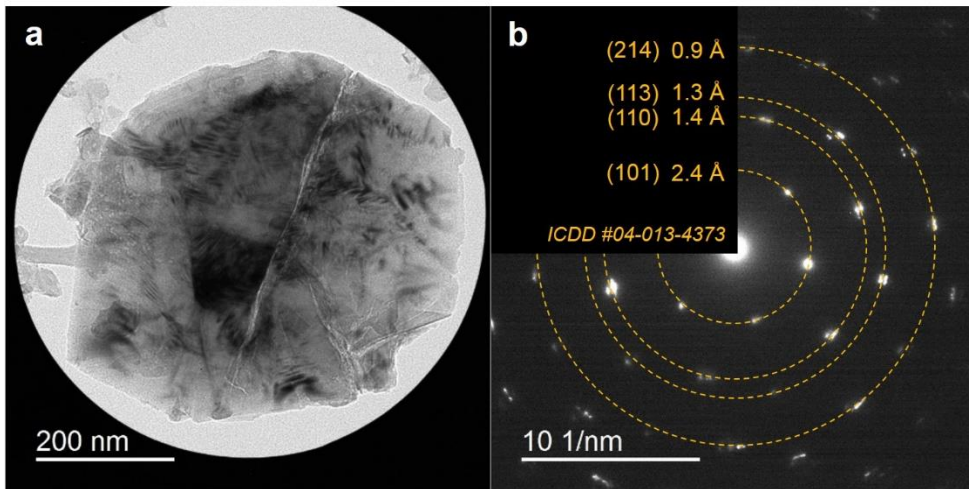


Figure 3.3.16. (a) TEM image and (b) SAED pattern of pristine LiCoO₂ particle.

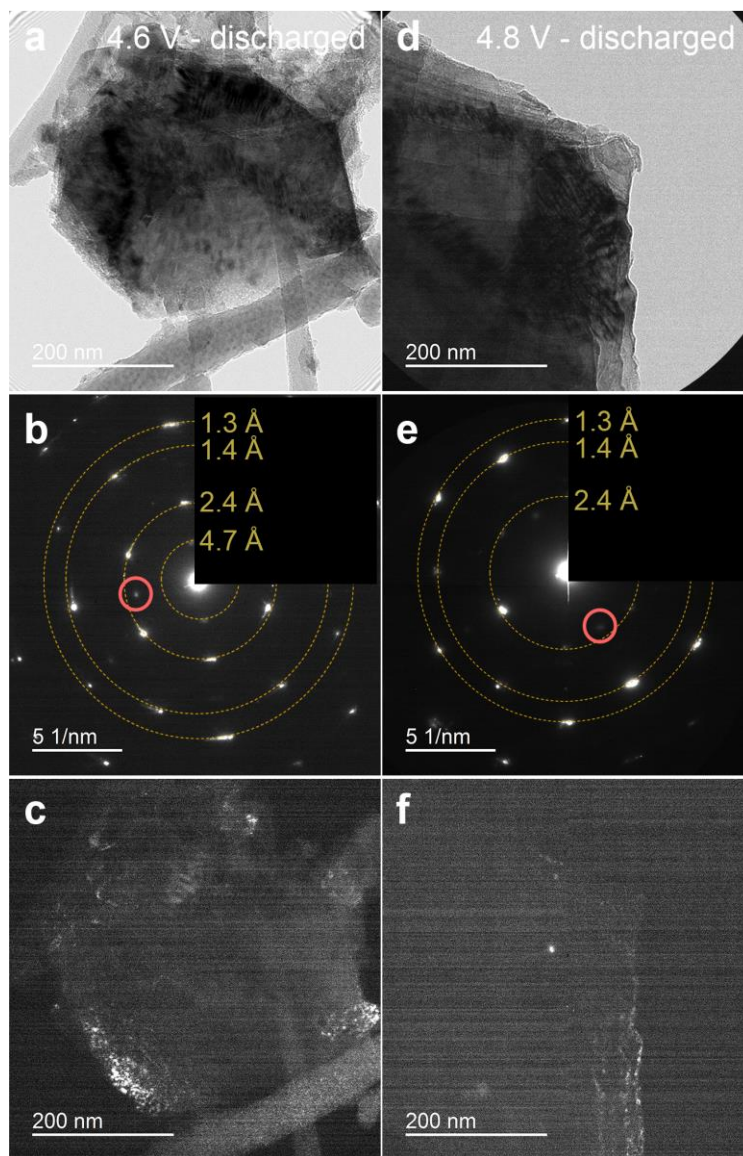


Figure 3.3.17. (a) and (d) bright-field TEM images, (b) and (e) SAED patterns, and (c) and (f), dark-field TEM images of LiCoO₂ particle obtained from electrochemically discharged electrode after 50 cycles of charge/discharge with upper voltage of 4.6 and 4.8 V, respectively. The position of the objective aperture for the dark-field image is indicated by the red circle in (b) and (e).

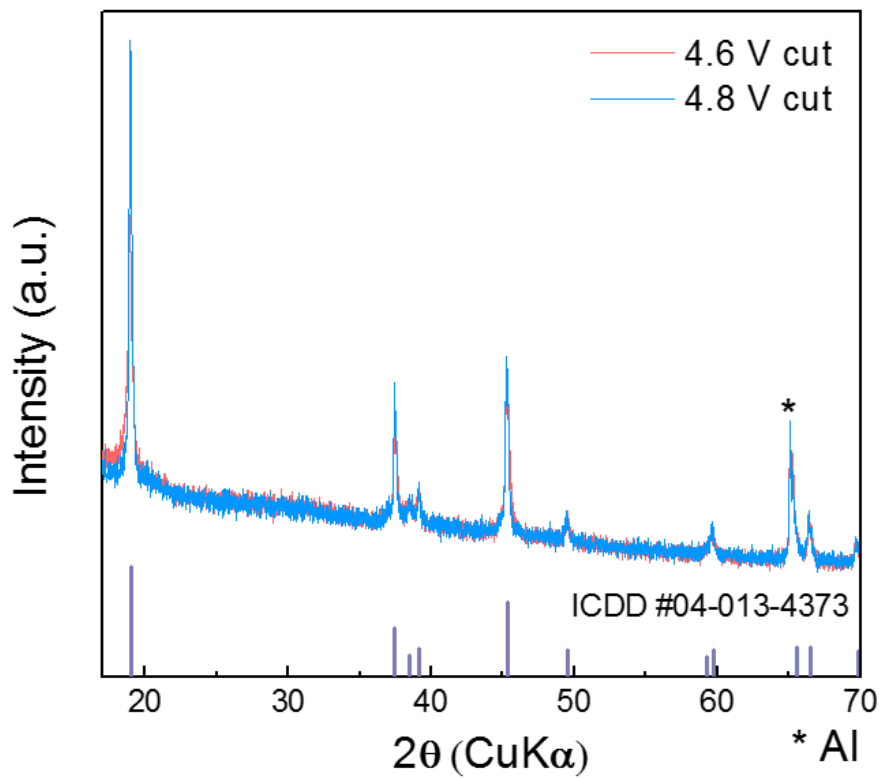


Figure 3.3.18. XRD pattern of 4.6- and 4.8-V-cycled LiCoO₂ discharged to 3.0 V (same result as **Figure 2a**) for entire 2θ measurement range (15°–70°).

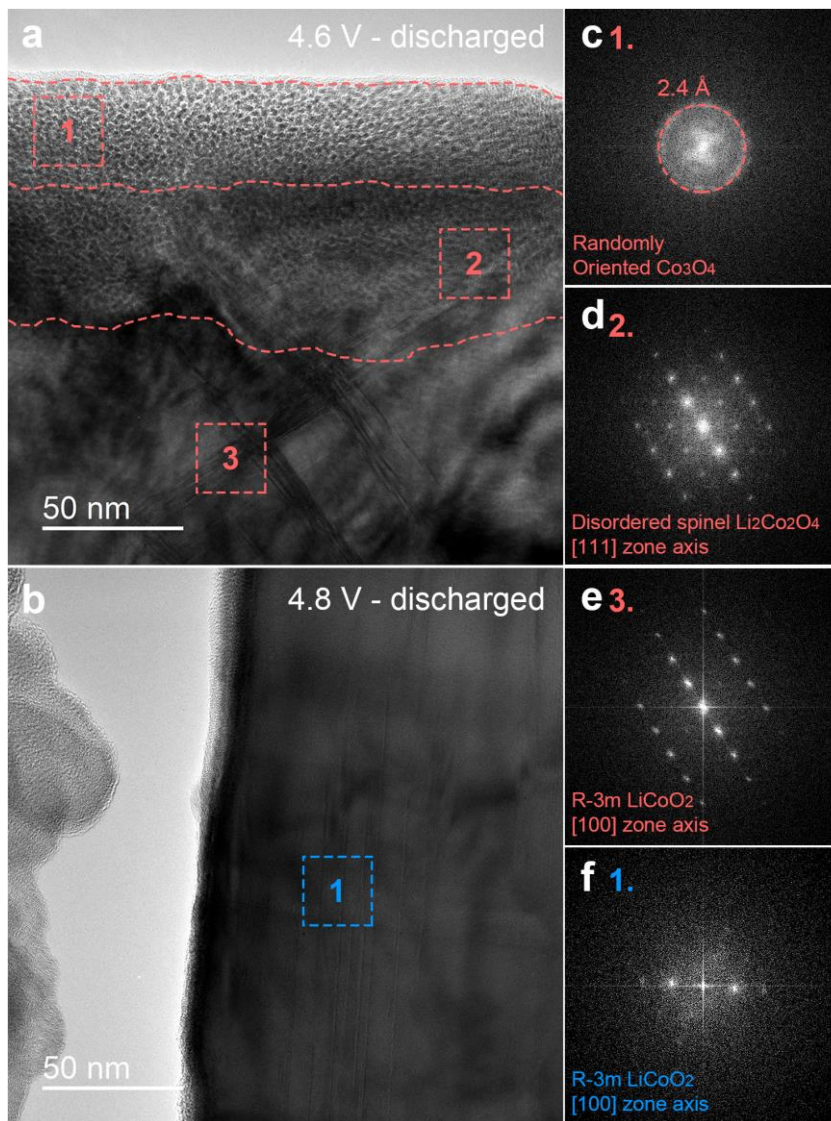


Figure 3.3.19. (a) and (b) high-resolution TEM images of near-surface region of LiCoO_2 for upper voltage of 4.6 and 4.8 V, respectively. (c)–(f) fast Fourier transformation calculated from regions indicated in (a) and (b).

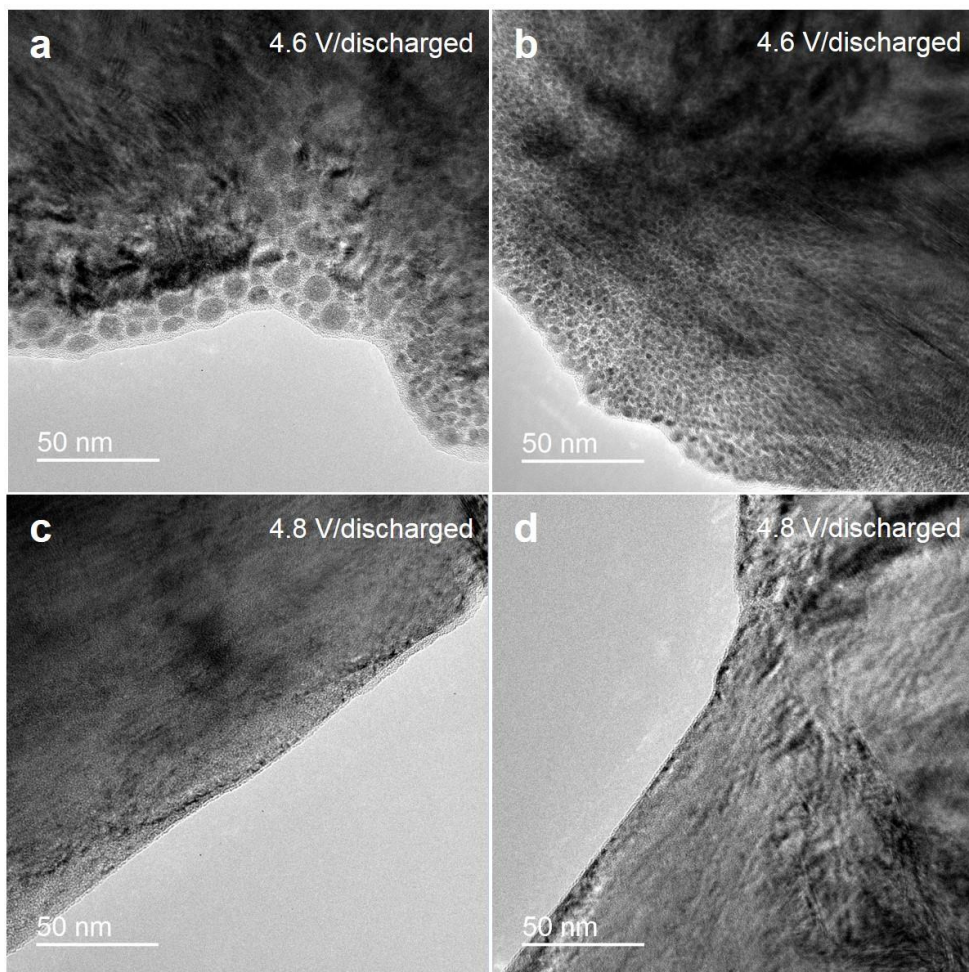


Figure 3.3.20. TEM images of the surface of (a and b) 4.6-V-cycled LiCoO_2 and (c and d) 4.8-V-cycled LiCoO_2 for other samples than those in **Figure 3.3.17**.

3.3.3. Suggestion of a new subtractive surface modification method

Although the origin of superior cyclability of LiCoO₂ at harsher 4.8-V cut-off condition was revealed, it is puzzling that the much more oxidative 4.8-V cycling condition results in a more robust surface of the LiCoO₂ electrode than 4.6-V cycling. To further confirm this result, we conducted additional galvanostatic charge/discharge experiments by alternating the cut-off voltages between 4.6 and 4.8 V. The experiment was performed in two ways: 1) 100 cycles with 4.8-V cut-off, followed by a change of the cut-off to 4.6 V (called '4.8→4.6-V cycling') and 2) 100 cycles with 4.6-V cut-off, followed by a change of the cut-off to 4.8 V (called '4.6→4.8-V cycling'). **Figure 3.3.21** presents the results for the first experiment with 100 cycles with a 4.8-V cut-off, followed by an additional 20 cycles with a 4.6-V cut-off. Although the electrochemical profiles for 80–100 cycles with the 4.8-V cut-off did not show a significant change (upper panel of **Figure 3.3.21**), the voltage hysteresis grew rapidly larger with the additional 4.6-V cut-off cycling (lower panel of **Figure 3.3.21**). The voltage hysteresis began to increase from the first cycle and continued to increase to the polarization value typically observed in 4.6-V cycling tests, as shown in **Figure 3.3.3a**. The EIS analysis in **Figure 3.3.22** also shows that the subsequent 4.6-V cycling led to a considerable increase in the surface charge-transfer resistance, as indicated by the growth of the semi-circle. The R_{ct} in **Figure 3.3.22b** decreased just after the cut-off voltage was decreased to 4.6 V; however, this observation appears to be a reflection of the lower polarization at low SOC, which can be cross-checked with the GITT results in **Figure 3.3.12b**.

The comparison of the surfaces of the 4.8-V-cycled and 4.8→4.6-V-cycled LiCoO₂ in **Figure 3.3.23** illustrates the apparent generation of a nanoparticulate structure at the surface with the additional 4.6-V cycling. The FFT of this

nanoparticulate region in **Figure 3.3.23b** reveals spots with a ring pattern corresponding to a d -spacing of 2.4 Å, indicating the growth of spinel Co_3O_4 , similar to the observations in **Figure 3.3.19c**. In contrast, the bulk region retained its pristine R-3m layered structure, as shown in **Figure 3.3.23c**. In contrast, the additional cycling with 4.8-V cut-off after 100 cycles with the 4.6-V cut-off led to a progressive reduction in the voltage hysteresis, as shown in **Figure 3.3.24**. Accordingly, the discharge capacity slightly improved over cycles as well. **Figure 3.3.22** shows that this improvement can be attributed to the recovered surface charge-transfer kinetics. The size of the semi-circle in the middle-to-low-frequency range was prominently reduced immediately after the cut-off voltage was increased to 4.8 V. The evolution of the surface morphology with the change of the cut-off voltage is consistent with the observations above. **Figure 3.3.25a** comparatively displays the surface morphology of the 4.6-V cycled and 4.6→4.8-V-cycled LiCoO_2 . It presents that the obvious nanoparticulate structure for the 4.6-V-cycled LiCoO_2 disappeared, leaving only a trace of a spinel-like phase at the surface (**Figure 3.3.25b**) with an apparently cleaner surface.

When the possibility that the Co_3O_4 at the surface transforms back to spinel $\text{Li}_2\text{Co}_2\text{O}_4$ or layered LiCoO_2 is ruled out, which is unrealistic for harsh 4.8-V cycling, it is speculated that the Co_3O_4 is electrochemically leached out from the surface during cycling, continuously exposing the clean LiCoO_2 surface. As it is well known that the cobalt dissolution of LiCoO_2 can occur when the operational cut-off voltage increases⁵⁸⁻⁵⁹, it may induce the removal of the resistive Co_3O_4 layer itself. Thus, we independently examined the cobalt dissolution characteristics by immersing the electrodes charged to 4.6 and 4.8 V in electrolyte at 25 °C for 24 h (**Table 3.3.1**). Inductively coupled plasma mass spectroscopy (ICP-MS) measurement of the electrolyte confirmed the faster dissolution from the 4.8-V-charged electrode than

from the 4.6-V-charged one. In addition, the faster dissolution at the 4.8-V cut-off was considerably augmented as the cycling proceeded: 1.55 times at the initial cycle and 11.0 times after 50 cycles (See **Table 3.3.1**). These observations suggest that the cobalt dissolution occurs sufficiently fast under such harsh conditions and can be rather ‘beneficial’, removing the detrimental surface layer. While it has been believed that dissolution of metal from the electrode is detrimental, the results also imply that the detrimental effect of cobalt dissolution on the electrode degradation is not as significant as that of the formation of the resistive surface layer during high-voltage cycling. For 4.8-V cycling of LiCoO₂ electrode whose result shown in **Figure 3.3.5a**, it is found that the major reduction of the discharge capacity took place for the first 10 cycles for the 4.8-V cycling: from 241.19 to 192.34 mAh/g (~19% decrease), then to 176.02 mAh/g after following 40 cycles (additional ~6.9% decrease). This is in contrast with the trend of Co dissolution rate with cycling as shown in **Table 3.3.1**: the Co dissolution becomes more dominant after more than 10 cycles. On the other hand, the Co dissolution is much smaller for the 4.6-V cycling, while the capacity fading is far severe. It indicates that the major capacity fading is not originated from only Co dissolution reaction. Instead, the change of the voltage profile in **Figure 3.3.3a** and **3.3.3b** clearly shows that the rapid increase of the polarization during the first 10 cycles plays the major role in the capacity fading. It also implies that the buildup of the polarization of LiCoO₂ electrode is effectively mitigated when Co dissolution occurs during the cycles from 10 to 50. This is consistent with our claim that the polarization growth by the resistive surface layer formation is the main reason for the rapid cycle degradations for high-voltage cut-off, which is the case of 4.6 V-cycling.

To further support our speculation about the ‘beneficial’ cobalt dissolution for the 4.8-V charging condition, we prepared a series of modified LiCoO₂ particles

that are known to be more resilient to cobalt dissolution *e.g.*, AlPO₄-coated LiCoO₂²¹⁻²². To coat AlPO₄ on LiCoO₂ powder, an AlPO₄-nanoparticle solution was prepared by dissolving Al(NO₃)₃·9H₂O and (NH₄)₂HPO₄ in distilled water until a white AlPO₄ nanoparticle suspension was formed. Then, 1 g of bare LiCoO₂ powder was added to this suspension and mixed vigorously for 10 min. The resulting slurry was dried in an oven at 120 °C for 6 h and heat-treated at 700 °C for 5 h in air. The nominal concentration of AlPO₄ in LiCoO₂ was set to 1 wt%. The SEM image of the AlPO₄-coated LiCoO₂ in **Figure 3.3.26a** clearly reveals the rough surface, which contrasts with the smooth surface of bare LiCoO₂ (see **Figure 3.3.9a**). This observation on rough surface is in accordance with previous report using the same coating method¹. The XPS spectra in **Figure 3.3.26b** indicate the existence of Al–O on the surface of the AlPO₄-coated LiCoO₂ particles⁶⁰. AlPO₄ coating has been known to generate the LiCo_{1-y}Al_yO₂ phase near the surface of LiCoO₂⁶⁰, and our result matches well with this previous report. The effect of AlPO₄-coating on LiCoO₂ during electrochemical cycling has been studied thoroughly by other groups⁶¹⁻⁶³. It has been proposed that the surface of AlPO₄-coated LiCoO₂ is covered by LiCo_{1-y}Al_yO₂ thin film, which is converted into Co-Al-O-F species by electrochemical cycling. This thin layer covers LiCoO₂ particle completely to serve as a protective layer to prevent Co dissolution and formation of byproduct such as LiF and Li_xPF_yO_z from side reactions at surface³. In **Table 3.3.1**, we confirmed by ICP-MS measurement that the dissolution of the Co from the AlPO₄-coated LiCoO₂ decreases compared with that of the noncoated LiCoO₂. This result agrees well with the previous report¹ and indicates that this role of blocking side reaction with electrolyte is beneficial for moderately high voltage condition such as 4.6-V cycling as shown in **Figure 3.3.27a**. On the other hand, the suppression of the surface side reaction appears not effective in the harsh 4.8-V cycling in **Figure 3.3.27b**. As previously discussed, the Co dissolution was important

in leaching out the resistive Co_3O_4 layer during 4.8-V cycling. Assuming that the similar phenomena occurs for the AlPO_4 -coated LiCoO_2 , the suppressed leaching effect with the protective AlPO_4 coating might lead to the buildup of the inactive Co_3O_4 in LiCoO_2 , which are expected to continuously increase the impedance. Interestingly, as shown in **Figure 3.3.28a**, the AlPO_4 -coated LiCoO_2 electrode after cycling showed the presence of Co_3O_4 , which contrasts to the case of the non-coated LiCoO_2 electrode after 4.8-V cycling, where Co_3O_4 are completely leached out, as shown in XRD pattern in **Figure 3.3.28b**. We believe that the coating of the AlPO_4 may have successfully protected the surface from the deposition of the electrolyte oxidation byproducts, however simultaneously retarded the leaching of the Co_3O_4 grown internally from the surface of LiCoO_2 . Thus, the unusual surface cleaning effect could not be observed even with the 4.8 V cut-off, leading to the eventual decay of the cycling. This result confirms that the ‘subtractive’ surface modification via the prompt cobalt dissolution played an important role in enhancing the stability of the 4.8-V cycling, which is distinguished from conventional ‘additive’ surface modification such as coating methods.

The effective removal of the resistive layer and the corresponding cycle stability hint that the reversibility of LiCoO_2 electrode with extended lithium extraction is intrinsically high, but has been covered by the high resistive film that increased the overall cell impedance. Moreover, it was shown that even with the substantial loss of the material from the surface due to leaching, the respectable cycle stability was demonstrated in the electrochemical half-cell. In this respect, we attempted to estimate the true reversibility of LiCoO_2 electrode ruling out the loss of the surface film material. The thickness of the accumulated resistive layer for the 4.6-V cycling was estimated to be ~50 nm from the TEM images in **Figure 3.3.19**

and 3.3.20. If this layer is assumed to be removed by the ‘subtractive’ surface modifications via 4.8-V cycling from the $\sim 2\text{-}\mu\text{m}$ size of the LiCoO_2 electrode particles (**Figure 3.2.1b**), roughly 15% of the pristine particle is removed after the 50 cycles. Considering this loss of the pristine LiCoO_2 electrode, the normalized capacity retention in **Figure 3.3.5a** with the effective weight of the electrode is as high as $\sim 86\%$ (207.4 mAh/g). This result indicates that the LiCoO_2 bulk has not been significantly deteriorated even with the cycling at 4.8-V cut-off, and implies that far more than 0.5 Li could be reversibly extracted/reinserted in remaining bulk LiCoO_2 without undergoing the irreversible phase transformation. It is believed that the phase transformations of the bulk structure are presumed to be relatively sluggish, thus the cycle degradation appears to be mainly caused by the resistive surface layer formation not by the irreversible phase transition even at high-voltage cycling.

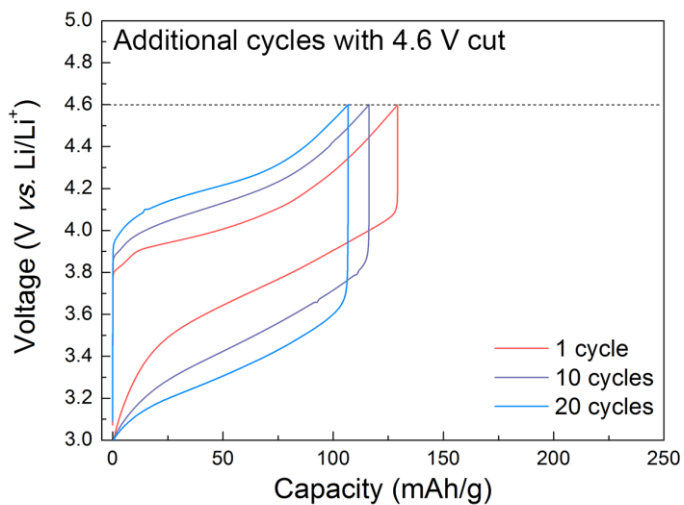
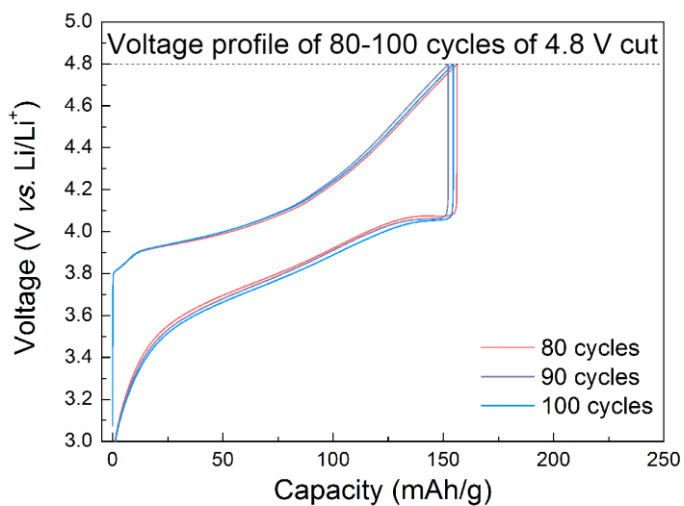


Figure 3.3.21. Galvanostatic charge/discharge profiles when upper voltage cut-off was changed from 4.8 V for 100 cycles to 4.6 V.

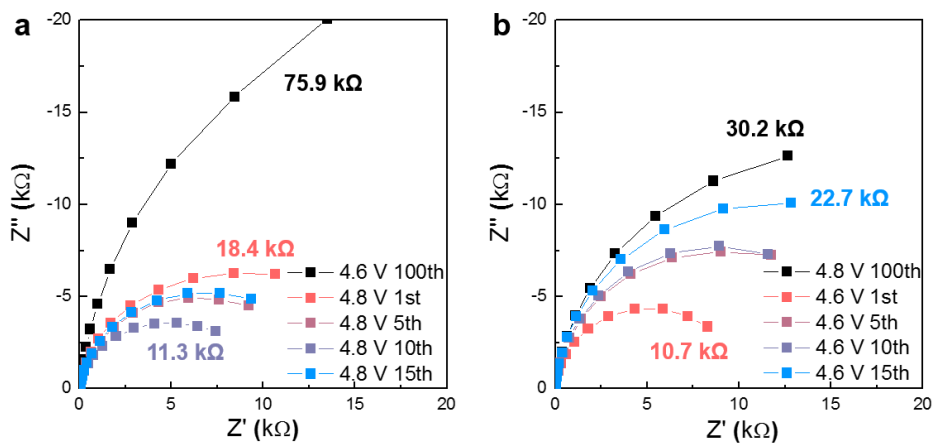


Figure 3.3.22. Nyquist plot obtained from EIS measurements by changing upper voltage cut-off (a) from 4.6 to 4.8 V and (b) from 4.8 to 4.6 V. The surface charge-transfer resistance R_{ct} values calculated from several representative semi-circles are denoted.

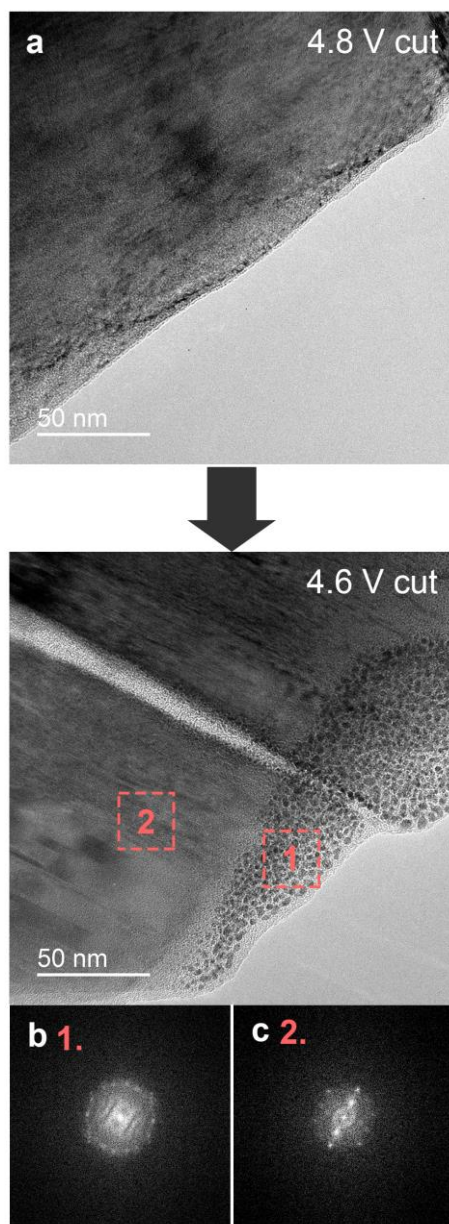


Figure 3.3.23. (a) TEM images of near-surface region of LiCoO₂ after 4.8 V for 100 cycles → 4.6 V for 50 cycles. (band c) FFT calculations from region 1 and 2, respectively.

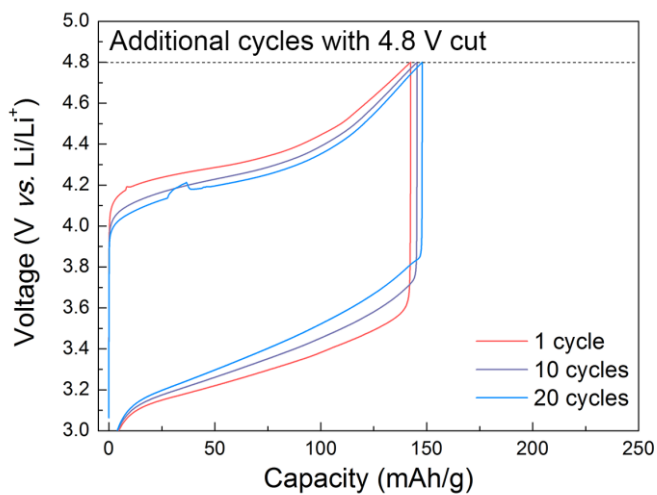
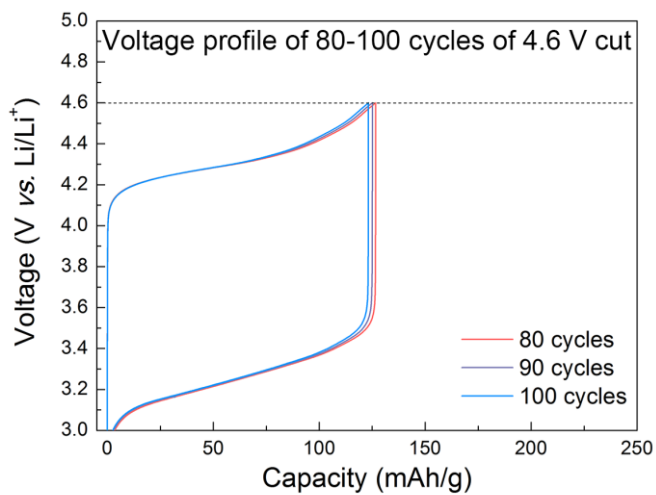


Figure 3.3.24. Galvanostatic charge/discharge profiles when upper voltage cut-off was changed from 4.6 V for 100 cycles to 4.8 V.

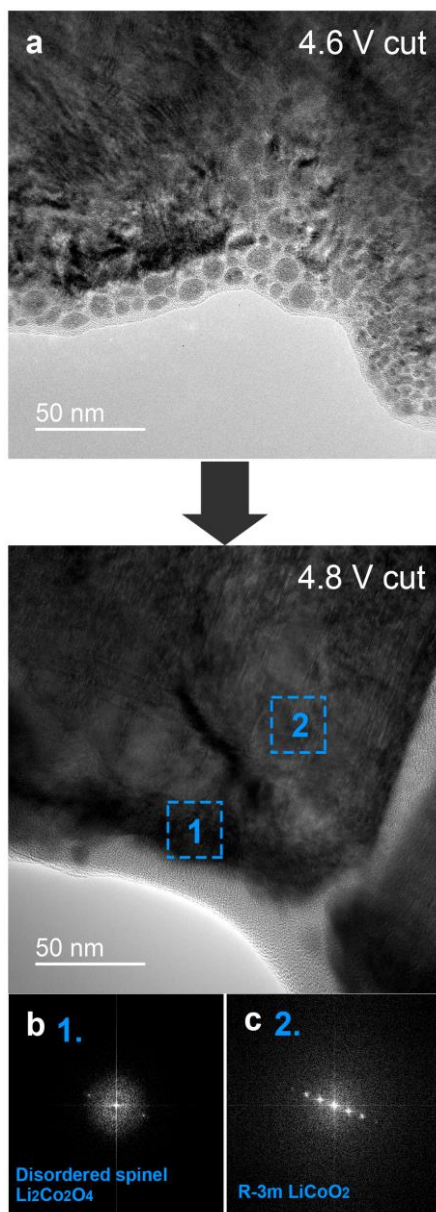


Figure 3.3.25. (a) TEM images of near-surface region of LiCoO₂ after 4.6 V for 100 cycles → 4.8 V for 50 cycles. (b and c) FFT calculations from region 1 and 2, respectively.

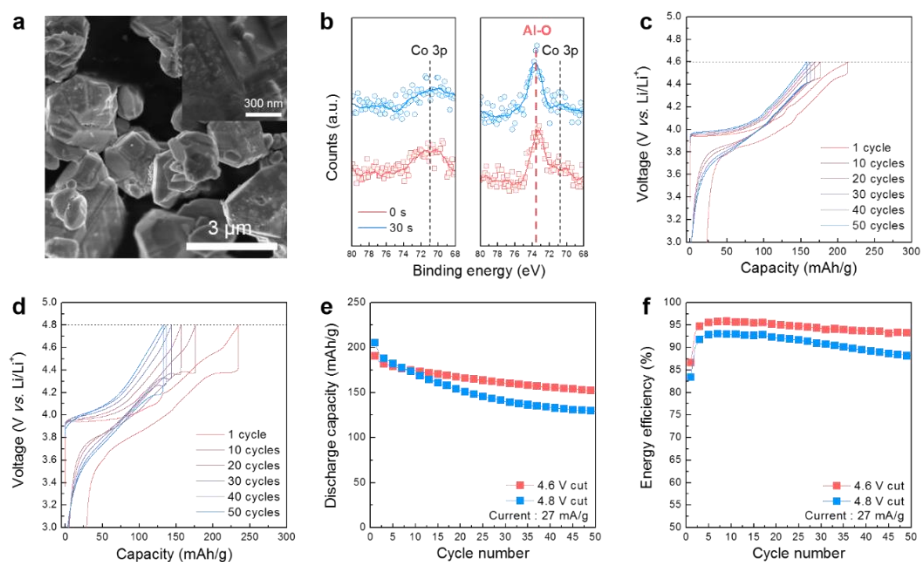


Figure 3.3.26. (a) SEM image of the surface of AlPO_4 -coated LiCoO_2 . (b) Al 2p XPS spectra of AlPO_4 -coated LiCoO_2 (right) and bare LiCoO_2 (left). The measurements were performed two times before and after Ar-ion milling for 30 s. (c–f) Comparison of cycle stability for 4.6- and 4.8-V-cut charge conditions after coating of AlPO_4 onto bare LiCoO_2 . (c) and (d) Galvanostatic charge/discharge profiles for upper voltage cut-offs of 4.6 and 4.8 V, respectively. (e) Discharge capacity and (f) energy efficiency change during electrochemical cycling.

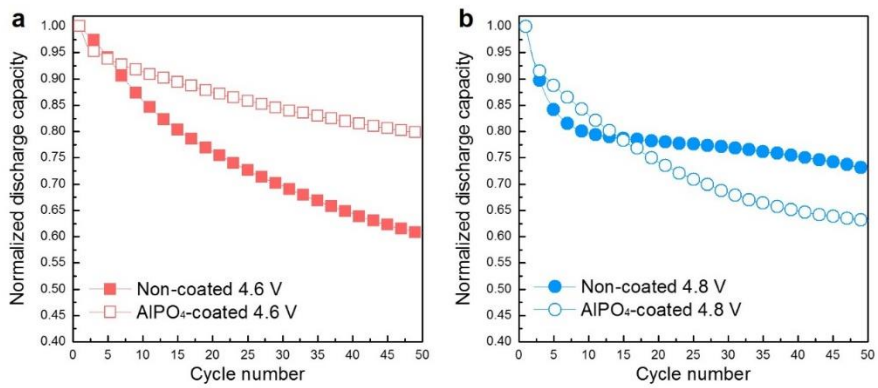


Figure 3.3.27. A comparison among the normalized discharge capacity cycled at (a) 4.6-V cut-off and (b) 4.8-V cut-off potential.

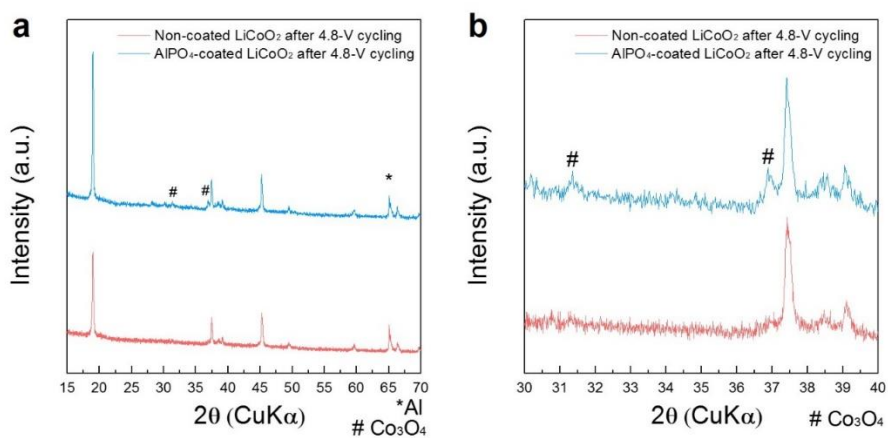


Figure 3.3.28. (a) XRD patterns of discharged non-coated and AlPO₄-coated LiCoO₂ electrode 50 cycles of 4.8-V cycling. (b) The enlarged XRD pattern of **Figure 3.3.28a** for the region where the presence or absence of Co₃O₄ impurities in the cycled electrode can be well compared.

Cut-off potential	Dissolved cobalt ion (ppb/weight of LiCoO ₂ in mg)			
	1 cycle	10 cycles	50 cycles	50 cycles : AlPO ₄ coated
4.6 V	206.0	69.67	52.53	15.04
4.8 V	320.9	143.1	579.1	119.6

Table 3.3.1. Concentration of dissolved cobalt ions in 1 M LiPF₆ in EC/DMC (1:1 v/v) electrolyte from charged Li_xCoO₂ measured by ICP-MS. The Li_xCoO₂ electrodes for the measurement were retrieved from Li/LiCoO₂ coin cells when the potential reached each cut-off at various cycle numbers: 1st, 10th, and 50th cycles with or without AlPO₄ coating.

3.4. Conclusion

We investigated the intrinsic reversibility of LiCoO_2 for high SOC range cycling (4.8-V cut-off). It was unexpectedly observed that electrochemical cycling of an uncoated LiCoO_2 electrode at 4.8-V cut-off results in superior capacity retention and smaller voltage hysteresis compared with those for the 4.6-V cut-off condition. In-depth experimental surveys revealed that the continuous formation of highly resistive surface layers composed of a spinel phase is the main reason for the rapid cycle degradations for high-voltage cut-off. However, 4.8-V cycling yields an abnormally clean surface because of the continuous etching of the surface, which occurs at a faster rate than the accumulation of the resistive spinel phase. This ‘beneficial’ leaching out of the resistive surface layer serves as ‘subtractive’ surface modification. Considering the loss of the active material on the surface, the reversible capacity of LiCoO_2 after 4.8-V cycling was estimated to be as high as ~86% after 50 cycles, which indicates that the instability of the crystalline Li_xCoO_2 ($x < 0.5$) has a limited effect, at least on this short-term cycle stability. This observation implies that the LiCoO_2 bulk is comparatively stable over high-voltage cycling, which contrasts with conventional belief, and that the cycle degradation is mainly caused by the resistive surface layer formation. Moreover, our findings explain why the strategy of coating foreign materials on the surface of LiCoO_2 can improve the high-voltage cycling to some extent despite the expected thermodynamic instability of the highly charged phase. This report sheds new light on the surface engineering of LiCoO_2 electrodes and the importance of the suppression of the formation of the resistive layer toward high-voltage cycle stability.

3.5. References

1. Berckmans, G.; Messagie, M.; Smekens, J.; Omar, N.; Vanhaverbeke, L.; Van Mierlo, J. *Energies* **2017**, *10* (9), 1314.
2. Chu, S.; Cui, Y.; Liu, N. *Nat. Mater.* **2016**, *16*, 16.
3. Patel, P. *ACS Cent. Sci.* **2015**, *1* (4), 161-162.
4. Kempton, W. *Nat. Energy* **2016**, *1*, 16131.
5. Myung, S.-T.; Maglia, F.; Park, K.-J.; Yoon, C. S.; Lamp, P.; Kim, S.-J.; Sun, Y.-K. *ACS Energy Lett.* **2017**, *2*, 196-223.
6. Kim, S.; Lee, J.; Lee, C. *Sustainability* **2017**, *9* (10), 1783.
7. Hong, J.; Gwon, H.; Jung, S.-K.; Ku, K.; Kang, K. *J. Electrochem. Soc.* **2015**, *162* (14), A2447-A2467.
8. Kim, S. Y.; Choi, S.-H.; Lee, E. J.; Kim, J.-S. *J. Korean Electrochem. Soc.* **2017**, *20* (4), 67-74.
9. Kumar, N. P.; M., E. E.; Florian, S.; Rao, P. T.; Nookala, M.; Philipp, A.; Hadar, S.; Francis, A.; Boris, M.; Doron, A. *Adv. Energy Mater.* **2018**, *8* (8), 1702397.
10. Xue, L.; Savilov, S. V.; Lunin, V. V.; Xia, H. *Adv. Funct. Mater.* **2018**, *28* (7), 1705836.
11. Ohzuku, T.; Ueda, A.; Nagayama, M.; Iwakoshi, Y.; Komori, H. *Electrochim. Acta* **1993**, *38* (9), 1159-1167.
12. Tsutomu, O.; Yoshinari, M. *Chem. Lett.* **2001**, *30* (7), 642-643.
13. Noh, H.-J.; Youn, S.; Yoon, C. S.; Sun, Y.-K. *J. Power Sources* **2013**, *233*, 121-130.
14. Tukamoto, H.; West, A. R. *J. Electrochem. Soc.* **1997**, *144* (9), 3164-3168.
15. Menetrier, M.; Saadoun, I.; Levasseur, S.; Delmas, C. *J. Mater. Chem.*

- 1999**, 9 (5), 1135-1140.
16. Xie, M.; Hu, T.; Yang, L.; Zhou, Y. *RSC Adv.* **2016**, 6 (68), 63250-63255.
 17. Mizushima, K.; Jones, P. C.; Wiseman, P. J.; Goodenough, J. B. *Mater. Res. Bull.* **1980**, 15 (6), 783-789.
 18. Kalluri, S.; Yoon, M.; Jo, M.; Park, S.; Myeong, S.; Kim, J.; Dou, S. X.; Guo, Z.; Cho, J. *Adv. Energy Mater.* **2017**, 7 (1), 1601507.
 19. Cho, J.; Kim, Y. J.; Park, B. *Chem. Mater.* **2000**, 12 (12), 3788-3791.
 20. Cho, J.; Kim, Y. J.; Kim, T. J.; Park, B. *Angew. Chem. Int. Ed.* **2001**, 40 (18), 3367-3369.
 21. Cho, J.; Kim, T.-G.; Kim, C.; Lee, J.-G.; Kim, Y.-W.; Park, B. *J. Power Sources* **2005**, 146 (1), 58-64.
 22. Lu, Y.-C.; Mansour, A. N.; Yabuuchi, N.; Shao-Horn, Y. *Chem. Mater.* **2009**, 21 (19), 4408-4424.
 23. Jung, Y. S.; Cavanagh, A. S.; Dillon, A. C.; Groner, M. D.; George, S. M.; Lee, S.-H. *J. Electrochem. Soc.* **2010**, 157 (1), A75-A81.
 24. Wang, D. Y.; Sinha, N. N.; Petibon, R.; Burns, J. C.; Dahn, J. R. *J. Power Sources* **2014**, 251, 311-318.
 25. Liu, A.; Li, J.; Shunmugasundaram, R.; Dahn, J. R. *J. Electrochem. Soc.* **2017**, 164 (7), A1655-A1664.
 26. Liu, Q.; Su, X.; Lei, D.; Qin, Y.; Wen, J.; Guo, F.; Wu, Y. A.; Rong, Y.; Kou, R.; Xiao, X.; Aguesse, F.; Bareño, J.; Ren, Y.; Lu, W.; Li, Y. *Nat. Energy* **2018**, 3, doi:10.1038/s41560-018-0180-6.
 27. Dong, T.; Zhang, J.; Xu, G.; Chai, J.; Du, H.; Wang, L.; Wen, H.; Zang, X.; Du, A.; Jia, Q.; Zhou, X.; Cui, G. *Energy Environ. Sci.* **2018**, 11 (5), 1197-1203.
 28. Nelson, K. J.; Harlow, J. E.; Dahn, J. R. *J. Electrochem. Soc.* **2018**, 165 (3), A456-A462.

29. Ceder, G.; Van der Ven, A. *Electrochim. Acta* **1999**, *45* (1), 131-150.
30. Reed, J.; Ceder, G.; Van Der Ven, A. *Electrochem. Solid-State Lett.* **2001**, *4* (6), A78-A81.
31. Jalem, R.; Mochiduki, Y.; Nobuhara, K.; Nakayama, M.; Nogami, M. *Phys. Chem. Chem. Phys.* **2012**, *14* (37), 13095-13100.
32. Wang, H.; Jang, Y. I.; Huang, B.; Sadoway, D. R.; Chiang, Y. M. *J. Electrochem. Soc.* **1999**, *146* (2), 473-480.
33. Aurbach, D.; Markovsky, B.; Rodkin, A.; Levi, E.; Cohen, Y. S.; Kim, H. J.; Schmidt, M. *Electrochim. Acta* **2002**, *47* (27), 4291-4306.
34. Gabrisch, H.; Yazami, R.; Fultz, B. *J. Electrochem. Soc.* **2004**, *151* (6), A891-A897.
35. Tan, H.; Takeuchi, S.; Bharathi, K. K.; Takeuchi, I.; Bendersky, L. A. *ACS Appl. Mater. Interfaces* **2016**, *8* (10), 6727-6735.
36. Amatucci, G. G.; Tarascon, J. M.; Klein, L. C. *J. Electrochem. Soc.* **1996**, *143* (3), 1114-1123.
37. Gabrisch, H.; Yazami, R.; Fultz, B. *Electrochem. Solid-State Lett.* **2002**, *5* (6), A111-A114.
38. Xia, H.; Lu, L.; Meng, Y. S.; Ceder, G. *J. Electrochem. Soc.* **2007**, *154* (4), A337-A342.
39. Yano, A.; Shikano, M.; Ueda, A.; Sakaebe, H.; Ogumi, Z. *J. Electrochem. Soc.* **2017**, *164* (1), A6116-A6122.
40. Radin, M. D.; Alvarado, J.; Meng, Y. S.; Van der Ven, A. *Nano Lett.* **2017**, *17* (12), 7789-7795.
41. Chen, Z.; Lu, Z.; Dahn, J. R. *J. Electrochem. Soc.* **2002**, *149* (12), A1604-A1609.
42. Delmas, C.; Braconnier, J.-J.; Hagenmuller, P. *Mater. Res. Bull.* **1982**, *17*

- (1), 117-123.
43. Armstrong, A. R.; Robertson, A. D.; Bruce, P. G. *Electrochim. Acta* **1999**, *45* (1), 285-294.
44. Jang, Y. I.; Huang, B.; Wang, H.; Sadoway, D. R.; Ceder, G.; Chiang, Y. M.; Liu, H.; Tamura, H. *J. Electrochem. Soc.* **1999**, *146* (3), 862-868.
45. Cho, W.; Myeong, S.; Kim, N.; Lee, S.; Kim, Y.; Kim, M.; Kang, S. J.; Park, N.; Oh, P.; Cho, J. *Adv. Mater.* **2017**, *29* (21), 1605578.
46. Aboulaich, A.; Ouzaouit, K.; Faqir, H.; Kaddami, A.; Benzakour, I.; Akalay, I. *Mater. Res. Bull.* **2016**, *73*, 362-368.
47. Dahéron, L.; Dedryvère, R.; Martinez, H.; Ménétrier, M.; Denage, C.; Delmas, C.; Gonbeau, D. *Chem. Mater.* **2008**, *20* (2), 583-590.
48. Ménétrier, M.; Carlier, D.; Blangero, M.; Delmas, C. *Electrochem. Solid-State Lett.* **2008**, *11* (11), A179-A182.
49. Ohzuku, T.; Ueda, A. *J. Electrochem. Soc.* **1994**, *141* (11), 2972-2977.
50. Laubach, S.; Laubach, S.; Schmidt, P. C.; Ensling, D.; Schmid, S.; Jaegermann, W.; Thi; Nikolowski, K.; Ehrenberg, H. *Phys. Chem. Chem. Phys.* **2009**, *11* (17), 3278-3289.
51. Van der Ven, A.; Aydinol, M. K.; Ceder, G. *J. Electrochem. Soc.* **1998**, *145* (6), 2149-2155.
52. Nobili, F.; Tossici, R.; Marassi, R.; Croce, F.; Scrosati, B. *The Journal of Physical Chemistry B* **2002**, *106* (15), 3909-3915.
53. Qiu, X.-Y.; Zhuang, Q.-C.; Zhang, Q.-Q.; Cao, R.; Ying, P.-Z.; Qiang, Y.-H.; Sun, S.-G. *Phys. Chem. Chem. Phys.* **2012**, *14* (8), 2617-2630.
54. Takamatsu, D.; Koyama, Y.; Oriyasa, Y.; Mori, S.; Nakatsutsumi, T.; Hirano, T.; Tanida, H.; Arai, H.; Uchimoto, Y.; Ogumi, Z. *Angew. Chem. Int. Ed.* **2012**, *51* (46), 11597-11601.

55. Lin, F.; Markus, I. M.; Nordlund, D.; Weng, T.-C.; Asta, M. D.; Xin, H. L.; Doeff, M. M. *Nat. Commun.* **2014**, *5*, 3529.
56. Yoon, C. S.; Jun, D.-W.; Myung, S.-T.; Sun, Y.-K. *ACS Energy Lett.* **2017**, *2* (5), 1150-1155.
57. Jung, S. K.; Gwon, H.; Hong, J.; Park, K. Y.; Seo, D. H.; Kim, H.; Hyun, J.; Yang, W.; Kang, K. *Adv. Energy Mater.* **2014**, *4* (1), 1300787.
58. Amatucci, G. G.; Tarascon, J. M.; Klein, L. C. *Solid State Ionics* **1996**, *83* (1), 167-173.
59. Kim, Y. J.; Cho, J.; Kim, T.-J.; Park, B. *J. Electrochem. Soc.* **2003**, *150* (12), A1723-A1725.
60. Y.-C. Lu, A. N. Mansour, N. Yabuuchi and Y. Shao-Horn, *Chem. Mater.*, 2009, **21**, 4408-4424.
61. Lee, J.-G.; Kim, B.; Cho, J.; Kim, Y.-W.; Park, B. *J. Electrochem. Soc.* **2004**, *151*, A801-A805.
62. Cho, J.; Lee, J.-G.; Kim, B.; Kim, T.-G.; Kim, J.; Park, B.; *Electrochim. Acta* **2005**, *50*, 4182-4187.
63. Lu, Y.-C.; Mansour, A. N.; Yabuuchi, N.; Shao-Horn, Y. *Chem Mater.* **2009**, *21*, 4408-4424.

Chapter 4. Controlling residual lithium chemistry during the synthesis of high-Nickel (>90%) $\text{Li}(\text{Ni}_x\text{Co}_y\text{Mn}_z)\text{O}_2$ cathode

4.1. Introduction

4.1.1. Obstacles for commercialization of high-Nickel layered cathode materials

Lithium-ion batteries (LIBs) are currently receiving great interest from both of scientific and industrial field not only due to its successful adoption to consumer electronics, but also its versatility extended to energy storage system in recent emerging electric vehicle (EV) technology^{1, 2}. The reason why LIBs are now dominant over other type of batteries such as nickel-metal hydride, nickel-cadmium, and lead-acid batteries is its even higher energy density than the others^{3, 4}. However, its energy density which directly determines the driving mileage of EVs is not high enough for overcome its strongest competitor, hydrogen fuel-cell. Although the broad distribution of fuel-cell electric vehicle (FCEV) is obstructed by its high infrastructure cost⁵⁻⁸, at least in terms of driving mileage FCEV (<600 km) shows much superior property than its counterpart (<400 km) raising its competitiveness^{8, 9}. For EVs to be broadly selected by customers of current passenger vehicles, developing LIBs with even higher energy density than ever is essential. To develop

LIBs with high energy density, energy density of cathode materials rather than anode materials has been known as a main bottleneck^{3, 4, 10-13}.

There are two main streams of strategy of improving energy density of cathode materials: the increase in operating voltage and specific capacity. Among them, increasing operating voltage of cathode material by increasing charge potential or state-of-charge (SOC) are now facing enormous obstacle caused by vigorous side reaction between electrolyte and cathode material^{14, 15}. Even if I somewhat succeeded to reveal the previously unattended interfacial behavior of cathode material at high voltage condition at **Chapter 3** in this thesis, still operating a battery with high voltage, normally indicating 5-volts-class battery, still remained as undeveloped wilderness to date. Instead of enduring needs of discovery of new electrode/electrolyte system, recently, makers of state-of-the-art EVs have attempted to develop high-Nickel $\text{LiNi}_x\text{Co}_y\text{Mn}_z\text{O}_2$ (NCM) layered cathode materials. In same potential range, doping of nickel into transition metal site of LiCoO_2 makes higher utilization level of lithium, leading to increased specific capacity. It is because of intrinsic superior specific capacity of LiNiO_2 : In the 3.0-4.3 V (vs. Li/Li^+) potential range, the specific capacity of LiCoO_2 is $\sim 150 \text{ mA h g}^{-1}$, while that of LiNiO_2 is $\sim 220 \text{ mA h g}^{-1}$ ^{16, 17}. The most of commercialized EVs nowadays adopts NCM with 60% of Ni ($\text{LiNi}_{0.6}\text{Co}_{0.2}\text{Mn}_{0.2}\text{O}_2$, known as NCM622), but demands on boosting driving ranges of EVs have attracted increasing interests on NCM with Ni content of $>80\%$ (high-Ni NCM). These demands are still far from accomplishment because of various deleterious phenomenon including Li/Ni site exchange, accelerated capacity fading, and poor thermal stability^{18, 19}. Above all, however, increasing tendency of formation of LiOH and Li_2CO_3 , so-called residual lithium compounds at surface acts as a big obstacle for commercialization of high-Ni NCM.

4.1.2. Current understanding on residual lithium at high-Ni NCM surface

There are two reasons of facile generation of LiOH and Li₂CO₃ at high-Ni NCM. The first cause is an unavoidable excess use of lithium source. To consider the volatile nature of lithium source, normally the mixture of precursor is composed of several percent of excess lithium compared with transition metal. Furthermore, it has been known that non-stoichiometric Li_{1-x}Ni_{1+x}O₂ is formed when lithium source is insufficient, which can deteriorate the performance of LIBs²⁰. This excess input of lithium precursor is generally led to remaining lithium compound which in turn act as 'residual lithium'. The second cause is more fundamental and about thermodynamic issue: unstable nature of trivalent Ni. When the content of Ni, Co and Mn is same in NCM, which is the case of LiNi_{0.33}Co_{0.33}Mn_{0.33}O₂, valence state of Ni is +2 while Co is +3, and Mn is +4²¹. As Ni content increases, the content of trivalent Ni becomes higher and great tendency of Ni³⁺ to be transformed into Ni²⁺ forms fragile surface composed of Ni²⁺-O bond²². This highly reactive surface can induce surface reconstruction to generate NiO phase at surface^{18, 19, 23} which result in the extraction of Li₂O during synthesis. This Li₂O at surface can be transformed into LiOH and Li₂CO₃ by reaction with ambient H₂O and CO₂ during the storage, respectively²⁴. The reactive surface itself can directly react with H₂O and CO₂ to make LiOH and Li₂CO₃, respectively.

This residual lithium can cause various detrimental effects during the operation of LIBs. One is the increase of pH of powder by large amount of LiOH and Li₂CO₃ can induce polymerization of the polyvinylidene fluoride (PVDF) by dehalogenation reaction^{25, 26}. Due to this phenomenon, electrode formation process is highly impeded by gelation of slurry by mixing high-Ni NCM, binder, conductive

agent in 1-methyl-2-pyrrolidone (NMP) solvent. The other is vigorous gas evolution due to side reaction of residual lithium with electrolyte during high temperature storage or battery operation²⁶⁻²⁸. As shown in page 16 in **Chapter 1**, LiOH and Li₂CO₃ can generate CO, CO₂ and in turn O₂ gas to raise safety issue which is fatal for adoption of high-Ni NCM in commercialized EVs.

4.1.3. Several attempts to mitigate residual lithium in high-Ni NCM

To reduce the residual lithium, there has been various attempts to reduce residual lithium in high-Ni NCM. The most common method is to simply wash the NCM powder with water to resolve the LiOH and Li₂CO₃^{20, 29-32}. Although this method is desirable from an industrial point of view due to its low cost and applicability to large-scale synthesis routes, it suffers from inevitable surface damage to active material itself²⁹⁻³². This causes reduction of discharge capacity of NCM, and the efficient post-treatment method has been developed^{31, 32}. Meanwhile, coating of alien material with low basicity such as Li₃PO₄, Na₂SO₄ and zirconium has been introduced by a number of research groups³³⁻³⁵, but high cost of coating method makes it still far from commercialization.

4.1.4. Purpose of this research

In this report, we suggest a new method to reduce residual lithium in high-Ni NCM layered cathode material without any post-treatment. During the annealing of mixture of lithium and transition metal precursor, other reactive gas was inserted shortly at high temperature to transform surface residual lithium to other species without basicity. In this methodology, different gas can be selected corresponding to target material to be formed at surface. In this report, we selected SO₂ gas to be

inserted during the synthesis to uniformly cover Li_2SO_4 at the surface of high-Ni NCM. Because of thermodynamically more stable nature of Li_2SO_4 than both of LiOH and Li_2CO_3 , the amount of LiOH and Li_2CO_3 sharply decreased without post-treatment such as washing and coating. Furthermore, this method aids the understanding of fundamental formation mechanism of residual lithium by altering the timing of insertion of SO_2 gas and tracking its effect on layered crystal structure and the amount of Li_2SO_4 . This bi-functional *in-situ* method for reduction of residual lithium compound will be attractive to be applied in large-scale synthesis route because of its removal of needs on post-treatment which can highly reduce synthetic cost.

4.2. Experimental section

4.2.1. Procedure of synthesis and SO₂-treatment of high-Nickel LiNi_{0.91}Co_{0.06}Mn_{0.03}O₂ powder

A homogeneous mixture of LiOH·H₂O and Ni_{0.91}Co_{0.06}Mn_{0.03}(OH)₂ was provided by industrial partner. The atomic composition ratio of Li and TM was 1.00 : 1 to rule out the possibility of formation of residual lithium by excess lithium source and remain only thermodynamic origin. The mixture was annealed at 700 °C for 10 h in O₂ atmosphere with heating and cooling rate of ~100 °C h⁻¹. The flow rate of oxygen during annealing was 1 L min⁻¹. For *in-situ* reduction of residual lithium compound during annealing, various type of gas (CO₂ or SO₂ or Ar/H₂(5%)) was inserted at certain timing for certain duration and flow rate corresponding to purpose of each experiment. After annealing, surrounding temperature of synthesized LiNi_{0.91}Co_{0.06}Mn_{0.03}O₂ (NCM9163) powder maintained at 200 °C, then immediately transferred into argon-filled glove box to avoid the exposure to ambient air (exposure time < 10 s).

4.2.2. Characterization of LiNi_{0.91}Co_{0.06}Mn_{0.03}O₂ powder

The amount of residual lithium compound was measured by common titration method. NCM9163 powders with/without SO₂ treatment were dispersed in deionized water for 30 min, then filtered water were subjected to titration method with 1 M HCl solution to calculate the each amount of LiOH and Li₂CO₃. Synthesized NCM9163 powders were analyzed using XRD (D2-PHASER, Bruker), SEM (SU-

70, Hitachi), TEM (JEM-2100F, JEOL), XPS (PHI 5000 VersaProbe, ULVAC-PHI), and time-of-flight secondary ion mass spectrometry (ToF-SIMS, TOF.SIMS-5, ION-TOF). In the XPS analysis, a monochromatic Al K α X-ray source (1486.6 eV) was generated using an acceleration voltage of 15 kV, and the binding energy was referenced to the C 1s peak at 284.5 eV. The electron takeoff angle was 45° relative to the sample plane, and the pass energy was set to 23.5 eV. Depth profile analysis was performed with Ar-ion sputtering of 2 kV acceleration voltage, and the raster size was 2 × 2 mm². The sputtering was performed in 1-min intervals for a total sputtering time of 25 min, and the rate was calibrated using a 100 nm SiO₂ reference film. It was observed that 20 nm of SiO₂ was etched by 1 min of sputtering. TOF-SIMS analysis were performed at a pressure of 3.8 × 10⁻⁹ torr. 100- μ s pulses of 30-keV Bi₁⁺ primary ions were used to scan a 200×200 μ m² area of the sample, which corresponds to an ion dose 2×10¹² ions cm⁻² (below the static limit). Each sample was analyzed 3 times at different locations and the average value was used. To minimize the damage of the surface of NCM9163 with the residual lithium compound, which can be vulnerable to the electron beam, the acceleration voltage was set to 120 kV in the TEM observation.

4.2.3. Electrode preparation and electrochemical analyses

NCM9163 powder (either treated with SO₂ gas or not), super P carbon black, and polyvinylidene fluoride (PVDF) were mixed in a weight ratio of 96:2:2 and added to *N*-methyl-2-pyrrolidone (NMP, anhydrous, 99.5%, Aldrich) for the electrode preparation. After this mixture was homogenized into a slurry, it was applied onto aluminum foil using the doctor-blade method, dried under vacuum overnight, and pressed by a roll-presser. Coin-type half cells (CR2032, Wellcos) were assembled

using the composite electrode as cathode, a lithium metal as an anode, Celgard 2400 separator, and LiPF₆-based carbonate electrolyte (provided by industrial partner) as an electrolyte. All of the preparation procedure mentioned above were performed in an argon atmosphere. Galvanostatic measurements of the charge/discharge of the Li/NCM9163 half-cells were conducted within the voltage range between 3.0 and 4.3 V at 25 °C as follows: formation cycle at 22 mA g⁻¹ (~0.1 C) followed by successive cycles at current rate of 0.1 C, 0.2 C, 0.5 C, and 1 C. For a cyclability test, repetition of charge/discharge was conducted at 1 C current rate 100 times. All of galvanostatic measurements utilized a multichannel potentiogalvanostat (WBCS-3000, Wonatech, Korea). *In-situ* gas detection spectrometry was carried out by a differential electrochemical mass spectrometry (DEMS) instrument constructed with the combination of a mass spectrometer (MS; HPR-20, Hiden analytical) and potentiogalvanostat to analyze the gases evolving from the Li/NCM9163 cell, by purging the cell with an Ar carrier gas (10 mL min⁻¹) continuously during electrochemical cycling. Simultaneously, the Ar carrier gas with gaseous products was pumped off to $\approx 10^{-7}$ Torr with rotary pump and turbomolecular pump sequentially (differential pumping), and then transferred to quadrupole mass spectrometer (MS; HPR-20, Hiden Analytical, UK). Before the DEMS experiment, the cell was connected to the MS being fully relaxed in the Ar flow for 12 h before charging. During cycling, electrochemical reaction and concomitant gas evolution from the cell were analyzed concurrently.

4.3. Results and discussion

4.3.1. The suggestion of *in-situ* gas-phase reaction method for surface modification of high-Ni layered cathode material

Thermodynamic unstable nature of high-Ni NCM surface makes complete prevention of formation of residual lithium compounds at surface so tough. Instead, transforming of them into other stable phase has been preferred³³⁻³⁵ and considered as facile method. However, different with other conventional surface coating method conducted after the synthesis, we tried to modify the surface ‘during’ the synthesis of high-Ni NCM by inserting reactive gas. In **Table 4.3.1**, we summarized the standard gibbs free energy of formation ($\Delta_f G^\circ$) of various LiX compound (X: anion)^{36, 37}. In spite of their relatively high stability, several LiX compound could be found as more stable species than LiOH and Li₂CO₃: Li₂SO₃ (only more stable than LiOH), Li₂SO₄ and Li₂S₂O₄. Because all of them has sulfur element in common, we chose SO₂ gas to be inserted during synthesis of high-Ni NCM to modify the surface of it. Our new gas-phase reaction methodology is schematically summarized in **Figure 4.3.1**. During the ‘normal annealing’ condition, common annealing process is proceeded, and SO₂ gas was injected for so-called ‘*In-situ* treatment’ shortly during annealing process to induce the transformation of residual lithium compound into S-containing compound. Flow rate and injection duration was set to 1 L min⁻¹ and 1 min, respectively. To limit reaction with SO₂ gas only at surface, reaction time (SO₂ injection duration) was only 1 min.

To test the effect of SO₂ gas injection during annealing process, XRD pattern of synthesized NCM9163 was measured for various SO₂ gas injection point. In

Figure 4.3.2, it is shown that overall layered structure is relatively unaffected (left panel), and small amount of Li_2SO_4 is formed when 20-30° range was magnified (right panel). To confirm that the origin of Li_2SO_4 is the reaction of SO_2 gas and LiOH or Li_2CO_3 , resultant powder was dispersed in deionized water, and filtered water was subjected to titration method with 1 M HCl solution. The results in **Table 4.3.2** shows that, interestingly, both of LiOH and Li_2CO_3 was reduced significantly irrespective of injection timing of SO_2 , even if the extent of reduction was different. Total residual lithium content in NCM9163 powder, expressed by ppm unit ((mass of total residual lithium element in mg) / (mass of active material in kg)) was decreased from 5114 to ~2000 ppm by simply injection of SO_2 gas only for 1 min during the synthesis. We also measured the amount of residual lithium in $\text{LiNi}_{0.6}\text{Co}_{0.2}\text{Mn}_{0.2}\text{O}_2$ (NCM622) powder for a comparison (result shown in **Table 4.3.2**), and even NCM622 that residual lithium issue is not important as that in high-Ni NCM (Ni>80 %) contains similar level of residual lithium in it. This means that the injection of SO_2 gas result in the transformation of residual lithium and emphasizes the effectiveness of this *in-situ* gas-phase reaction method.

Li_2SO_4 is known as weak acid³⁸, and we also measured the pH of Li_2SO_4 dissolved in water to ~6.1. In contrast, LiOH and Li_2CO_3 is known as very strong base, thus the effect of Li_2SO_4 to overall pH is expected to be negligible. Nevertheless, to rule out the effect of acidic atmosphere of Li_2SO_4 to cause the underestimation of pH even if real amount of LiOH and Li_2CO_3 is unchanged, we performed a model experiment of titration of LiOH - Li_2CO_3 - Li_2SO_4 mixture. While total number of lithium ion is fixed, the concentration of LiOH , Li_2CO_3 and Li_2SO_4 is systematically changed as presented in **Figure 4.3.3**. It should be noted that, we also fixed the ratio between LiOH and Li_2CO_3 as 1:1, and only concentration of Li_2SO_4 in powder mixture is changed while the sum of LiOH and Li_2CO_3 is

accordingly changed. As result, shown in **Figure 4.3.3**, both of volume of inserted 1 M HCl solution at equivalent point 1 (EP₁), indicative of the amount of LiOH, and the volume difference of EP₁ and EP₂, indicator of the amount of Li₂CO₃ decreased inverse-proportionally to Li₂SO₄ concentration in whole mixture (The fundamental detail of analysis of titration curve is explained elsewhere³⁹). This means that titration result is in accordance with the ‘real’ concentration of LiOH and Li₂CO₃.

Although the insertion of SO₂ gas during the synthesis of NCM9163 was succeeded in reduction of LiOH and Li₂CO₃ compounds, $I_{(003)}/I_{(104)}$ value calculated from XRD pattern, which is an indicator of Li/Ni site exchange and degree of ordering of layered crystal structure, of synthesized powder shown in **Table 4.3.2** indicates that the SO₂ gas insertion can rather impede the formation of layered structure. The origin of this deterioration of layered structure by SO₂ gas might due to its role as a reductant⁴⁰ and thus spoiling ability of oxidative atmosphere (built by O₂ gas flow) during the synthesis of NCM9163 which is highly necessary for the formation of layered structure⁴¹. However, considering very short duration of injection of SO₂ gas, this effect would be negligible. Instead, highly reactive nature of NCM9163 at high temperature would make it provide large amount of lithium inside the bulk structure to induce collapse of layered structure. Therefore, it can be inferred from this lesson that insertion of SO₂ gas after layered structure formation is complete would be effective in limiting the reaction only at surface. To demonstrate this suggestion, SO₂ gas insertion point is changed to cooling step during synthesis, and insertion temperature was set as a variable. In **Figure 4.3.4**, the XRD pattern of synthesized NCM9163 was collected and, as displayed in **Table 4.3.2**, $I_{(003)}/I_{(104)}$ value continuously increases as reaction temperature decreased. Meanwhile, however, the amount of residual lithium decreased sharply in between 600 °C and 500 °C and increased as reaction temperature decreased further. This

means that the reaction between SO_2 gas and $\text{LiOH}/\text{Li}_2\text{CO}_3$ is thermally-activated process and, interestingly, between 600 °C and 500 °C, the reaction is concentrated within surface region because reactivity of bulk NCM9163 decreased significantly at temperature below 700 °C. This trend of the changes in the amount of residual lithium and $I_{(003)}/I_{(004)}$ mentioned above is summarized in **Figure 4.3.5** to find the optimum reaction point between NCM9163 with SO_2 gas. As shown in figure, we could find the timing of SO_2 injection when layered structure retains that of pristine NCM9163 well and surface-concentrated reaction occurs; 500 °C during cooling step. At this point surface-concentrated reaction with SO_2 gas induces efficient transformation of LiOH and Li_2CO_3 into Li_2SO_4 without change of bulk crystal structure.

The generality of this gas-phase reaction method to modify the surface of high-Ni cathode materials is confirmed by insertion of other gas during synthesis. As presented in **Table 4.3.3**, we inserted CO_2 and Ar/H_2 (5 %) mixture gas at 500 °C during the cooling step and analyzed its effect on the amount of residual lithium compound. When CO_2 gas is inserted, the amount of Li_2CO_3 increased sharply and thus the amount of LiOH decreased accordingly. This can be simply interpreted by transformation of LiOH into Li_2CO_3 by reaction with CO_2 . On the other hand, Ar/H_2 (5%) mixture gas which creates reductive atmosphere increased LiOH and decreased Li_2CO_3 slightly to increase total residual lithium amount. Considering non-reactivity of H_2 gas with LiOH and Li_2CO_3 (much higher formation energy of LiH than them shown in **Table 4.3.1**), it confirms again that the reductive atmosphere itself is harmful for the high-Ni NCM by increasing total residual lithium.

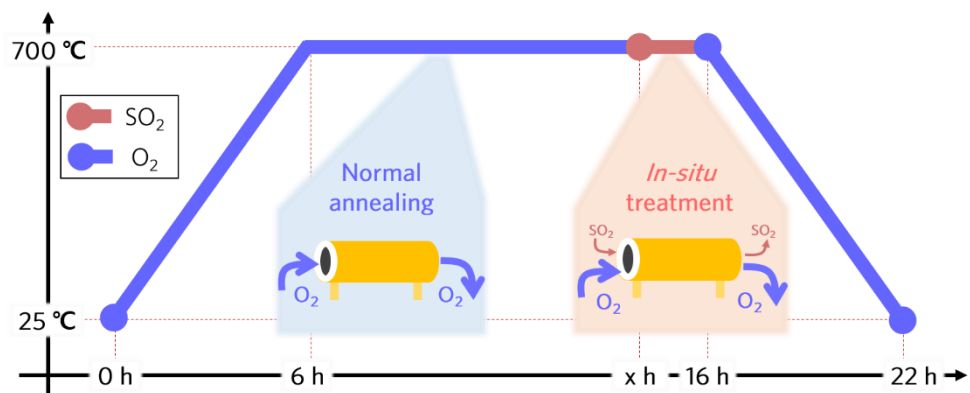


Figure 4.3.1. Schematic illustration of suggested in-situ gas-phase reaction method during synthesis of high-Ni NCM.

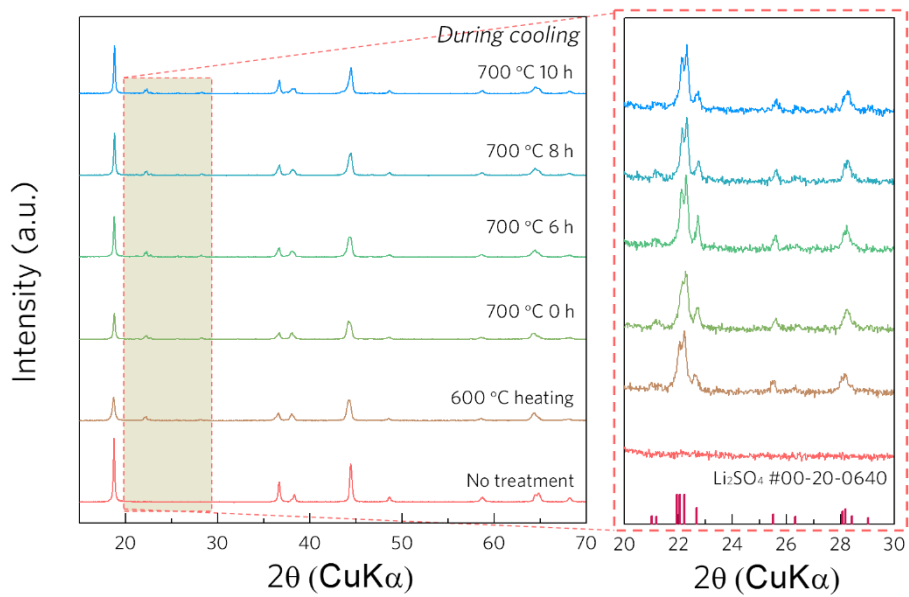


Figure 4.3.2. XRD patterns of synthesized NCM9163 powders for various reaction timing with SO_2 gas during annealing.

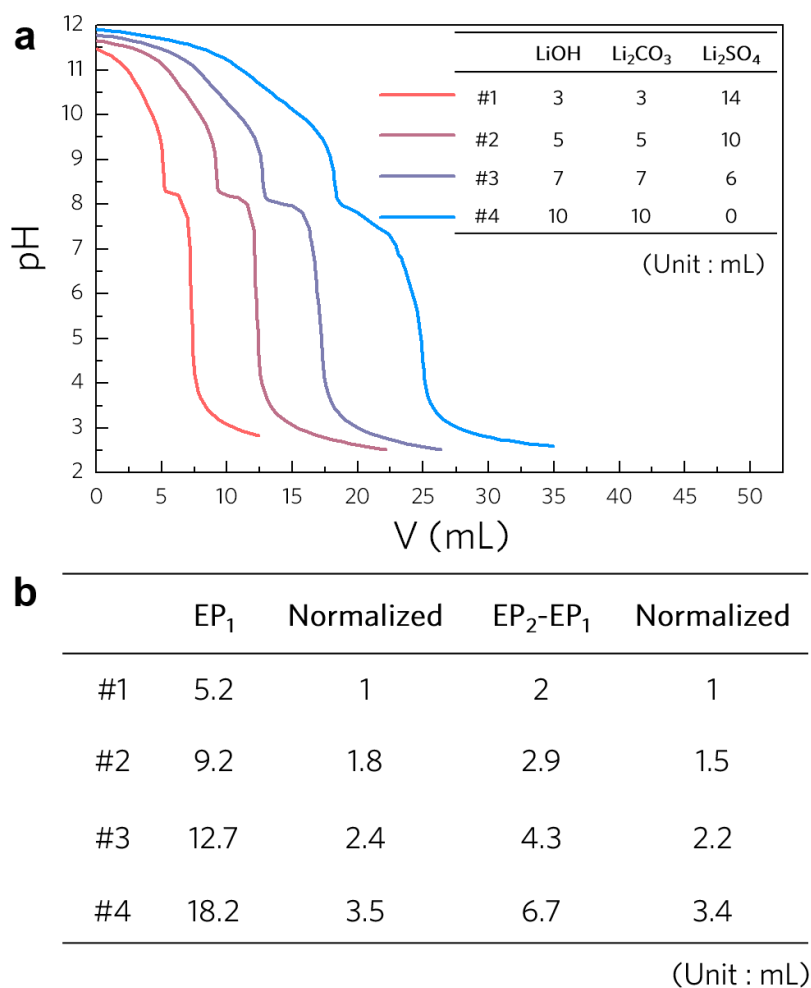


Figure 4.3.3. Effect of Li₂SO₄ on titration result by mixing LiOH, Li₂CO₃, and Li₂SO₄ powder. (a) Titration curve of LiOH-Li₂CO₃-Li₂SO₄ mixture. Legend shows the volume of each powder-based aqueous solution (concentration of powder was fixed to 2500 ppm). (b) A summary of equivalent points (EPs) derived from titration curve at (a)

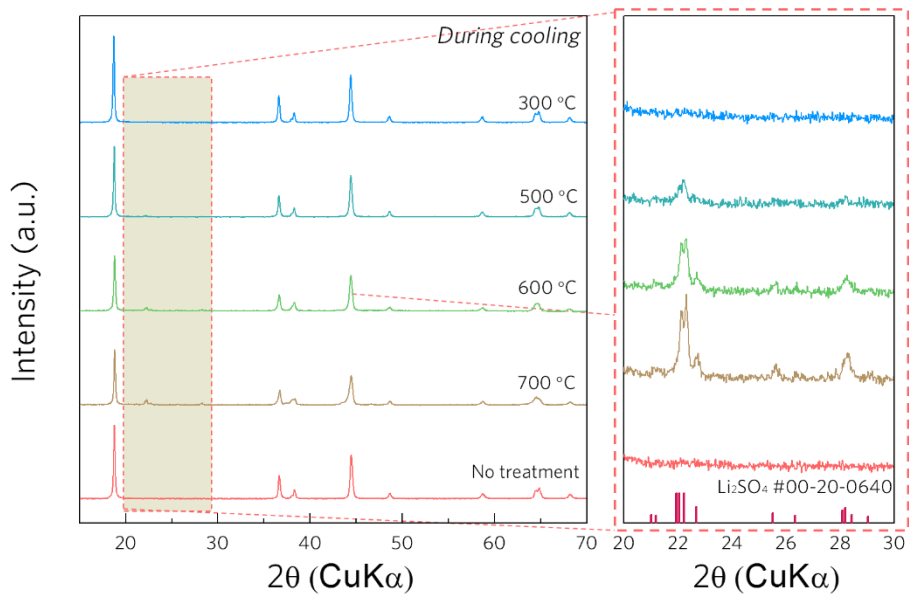


Figure 4.3.4. XRD patterns of synthesized NCM9163 powders for various reaction temperature with SO_2 gas during cooling step during annealing.

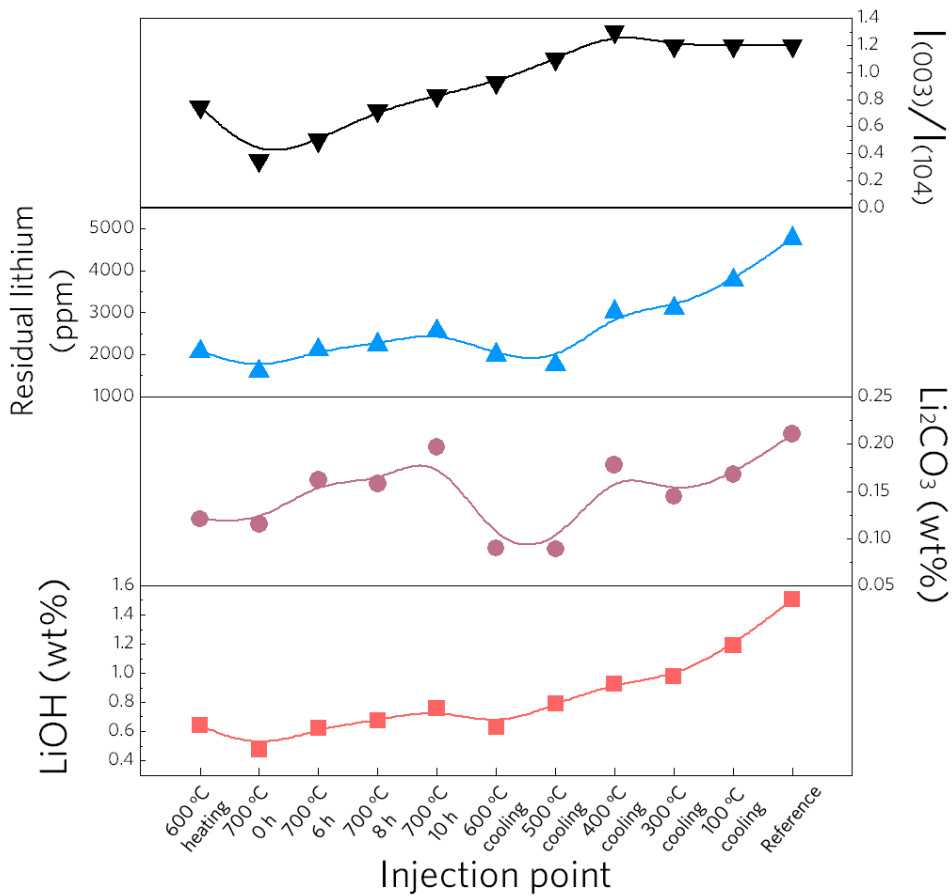


Figure 4.3.5. Changing trend of various characteristic parameters (The amount of residual lithium and $I_{(003)}/I_{(104)}$ which is an indicator of quality of layered structure) of surface-modified NCM9163.

LiX compound	Formation energy (kJ/mol)	LiX compound	Formation energy (kJ/mol)
Li ₂ SO ₄	-1324.7	Li ₂ S	-439.1
Li ₂ S ₂ O ₄	-1179.2	LiOH	-438.9
Li ₂ CO ₃	-1132.2	LiCl	-384.0
Li ₂ SO ₃	-1092.0	LiNO ₃	-381.2
LiOH•H ₂ O	-689.5	LiBr	-341.6
LiF	-588.7	LiI	-269.7
Li ₂ O ₂	-571.1	Li ₃ N	-154.0
Li ₂ O	-561.9	LiH	-69.9

Table 4.3.1. List of standard gibbs free energy of formation for various LiX compounds.

Sample	LiOH (wt%)	Li ₂ CO ₃ (wt%)	Total residual Li (ppm)	I ₍₀₀₃₎ /I ₍₁₀₄₎
No treatment (Reference)	1.62	0.218	5114	1.2
600 °C heating	0.621	0.118	2081	0.75
700 °C 0 h	0.480	0.115	1606	0.34
700 °C 6 h	0.623	0.162	2111	0.5
700 °C 8 h	0.674	0.158	2251	0.72
700 °C 10 h	0.760	0.196	2570	0.83
600 °C	0.633	0.0898	2003	0.93
500 °C	0.788	0.0890	2452	1.1
400 °C	0.930	0.177	3029	1.3
300 °C	0.977	0.144	3102	1.2
100 °C	1.19	0.168	3771	1.2
NCM622	0.608	0.148	2039	-

Table 4.3.2. Summary of the amount of residual lithium compounds at different reaction point with SO₂ gas and ratio of I₍₀₀₃₎/I₍₁₀₄₎ calculated from XRD pattern of corresponding NCM9163 powder. For comparison, the amount of residual lithium compounds on NCM622 powder was also measured and corresponding results are shown.

Sample	LiOH (wt%)	Li ₂ CO ₃ (wt%)	Total residual Li (ppm)
No treatment (Reference)	1.45	0.326	4967
CO ₂ annealed	0.734	5.75	12925
Ar/H ₂ (5%) mixed gas	1.99	0.272	6303

Table 4.3.3. The amount of residual lithium compounds of NCM9163 powder which undergone the treatment with other kinds of gas than SO₂ at ~500 °C during cooling.

4.3.2. Characterization of the surface of high-Ni layered cathode material

To characterize the morphology of Li_2SO_4 on the surface of NCM9163, scanning electron microscopy (SEM) was used to obtain its image. As displayed in **Figure 4.3.6a** and **c**, overall morphology of sphere-like secondary particle composed of primary particle whose size is several hundreds of nanometer is maintained even after the reaction with SO_2 gas. However, in **Figure 4.3.6d**, some crystallites are formed at the surface of this secondary particle, and this crystallites seem to be the strong evidence of formation of Li_2SO_4 , when compared with the surface of pristine NCM9163 particle shown in **Figure 4.3.6c**. Even if surface morphology is entirely changed to Li_2SO_4 crystallites, its bulk morphology is unchanged, which is confirmed by cross-sectional SEM image presented at **Figure 4.3.7**. This confirms again that the reaction with SO_2 gas is concentrated at the surface, not affecting the morphology of bulk structure. Microstructure of this surface Li_2SO_4 is further investigated by help of transmission electron microscope (TEM). To make thin-film sample from 10- μm -size sphere-like NCM9163, focused-ion beam (FIB) was used. NCM9163 particle was covered with platinum (Pt) protective film, and Ga^+ beam is bombarded to etch the sample. In **Figure 4.3.8**, pristine NCM9163 particle is covered with very thin, organic film with thickness of ~ 10 nm (**Figure 4.3.8c**) without any crystal structure (FFT calculation result shown in **Figure 4.3.8d**). In contrast, TEM observation on SO_2 -treated NCM9163 particle shows a film with thickness of ~ 50 nm as shown in **Figure 4.3.9c**. The crystal structure of this film is found to be Li_2SO_4 by FFT calculation on that region (**Figure 4.3.9d**). The relative uniform distribution of Li_2SO_4 on the surface of NCM9163 demonstrates the advantage of gas-phase reaction method. The elemental distribution of this film was analyzed by STEM-

EDS mapping. In **Figure 4.3.10** and **11**, it is confirmed that sulfur is contained only at surface film and not detected at bulk of SO₂-treated NCM9163. Even if sulfur is detected at platinum layer, it is because of Kramer's law⁴², mentioning that element of higher atomic number of platinum gives higher background that will counts as existence of sulfur during elemental mapping.

Surface-specific analysis is also performed to characterize the chemical nature of surface Li₂SO₄ film. At first, depth-profile of X-ray photoelectron spectroscopy (XPS) spectrum was obtained for pristine NCM9163 and SO₂-treated NCM9163 during etching of surface with bombarding Ar⁺ ion. In **Figure 4.3.12a**, Ni 2p XPS spectra was obtained and much lower nickel signal at sub-surface region until ~5 min of milling time at SO₂-treated NCM9163 implies the relative thick film of Li₂SO₄ at the surface. This region is composed mainly of sulfur which is confirmed by **Figure 4.3.12b** presenting S 2p XPS spectra. At right-side panel, sulfur was detected at thick region from outermost surface until ~10 min milling time. Interestingly, surface region is not only composed of Li₂SO₄, but also small amount of Li₂S₂O₄. It is because both of Li₂SO₄ and Li₂S₂O₄ is thermodynamically more stable than LiOH and Li₂CO₃, and Li₂SO₄ is the most stable phase (see **Table 4.3.1**). The formation of Li₂SO₄ at surface region is confirmed again by O 1s XPS spectra (**Figure 4.3.12c**), which shows Li₂SO₄ signal at same region where sulfur is detected in S 2p XPS spectra. It should be noted that outermost surface region is somewhat reduced which is indicated by slightly lower binding energy of oxygen of SO₂-treated NCM9163 than that of pristine NCM9163. This indicates the reductive nature of SO₂ gas again. Although the formation of Li₂SO₄ is clearly visualized by XPS spectra, the effect of reduction of LiOH and Li₂CO₃ compound is blurred in here by strong signal from Li₂SO₄. Therefore, time-of-flight secondary ion mass spectrometry (ToF-SIMS) was used to understand the distribution of molecular species at surface

film formed by reaction with SO_2 gas. This technique has much higher sensitivity for detecting ion from outermost surface region and effective to analyze only the nature of surface⁴³. In Figure 4.3.13, normalized ion density of various species containing lithium, carbon, and oxygen which are derived from surface residual lithium LiOH and Li_2CO_3 is displayed. It is proved that the amount of all of these species were significantly reduced by reaction with SO_2 gas. These surface-specific analyses validated our suggestion again that *in-situ* gas-phase reaction transformed surface LiOH and Li_2CO_3 into other component, Li_2SO_4 in this case.

Although we have been succeeded to transform surface LiOH and Li_2CO_3 into Li_2SO_4 without the degradation of bulk structure by simple gas-phase reaction during synthesis, the effect of this transformation on overall battery performance should be tested, because this method would be meaningless if it rather compromised battery performance of active material. Because Li_2SO_4 is electronically resistive⁴⁴, covering entire surface of NCM9163 with 50 nm of Li_2SO_4 film can be detrimental and increase polarization of LIB. Therefore, an electrochemical test on this surface-modified cathode material was performed with Li/NCM9163 half-cell. For a comparison, a test on pristine NCM9163 was also conducted. In Figure 4.3.14, voltage profile of Li/NCM9163 at various current rate is shown. For discharge capacity, reference NCM9163 exhibited 218 mA h g^{-1} at 0.1 C ($\sim 22 \text{ mA g}^{-1}$), 209 mA h g^{-1} at 0.2 C, 199 mA h g^{-1} at 0.5 C, and 193 mA h g^{-1} at 1 C. This performance is similar with other previous reports on high-Ni NCM with similar composition⁴⁵. Unfortunately, however, as can be seen in Figure 4.3.15, discharge capacity of Li/(SO_2 -treated-NCM9163) cell significantly reduced due to augmented polarization. Discharge capacity of SO_2 -treated NCM9163 showed 166 mA h g^{-1} at 0.1 C and 156 mA h g^{-1} at 0.2 C. This means that the additional optimization process is highly needed for increasing adaptability of this method to large-scale synthesis.

Although Li_2SO_4 formation concentrated at surface is confirmed by previous analyses, much thicker film of Li_2SO_4 than $\text{LiOH}/\text{Li}_2\text{CO}_3$ film should be rationalized because lithium source of Li_2SO_4 other than surface $\text{LiOH}/\text{Li}_2\text{CO}_3$ should be explained if mol amount of Li_2SO_4 is more than that of Li_2CO_3 and LiOH . In doing this, at first, molar density of Li_2SO_4 ($0.020 \text{ mol cm}^{-3}$) than Li_2CO_3 ($0.029 \text{ mol cm}^{-3}$) and LiOH ($0.061 \text{ mol cm}^{-3}$) should be considered. And, molar ratio of LiOH and Li_2CO_3 at pristine NCM9163 is needed and we calculated it to 22.4 :1 with molar mass of LiOH (23.95 g mol^{-1}) and Li_2CO_3 (73.89 g mol^{-1}) and weight ratio data at **Table 4.3.2**. Using this values, thickness of $\text{LiOH}/\text{Li}_2\text{CO}_3$ film should be increase to 150 % of original value if no lithium is provided out of residual lithium compound, which means that 10 nm of original film should be increased to 15 nm. However, TEM images showed much thicker film of Li_2SO_4 on SO_2 -treated NCM9163. This indicates that extra lithium came from the bulk of NCM9163 during synthesis to affect bulk crystal structure to slightly decrease $I_{(003)}/I_{(104)}$ value of SO_2 -treated NCM9163, as mentioned in previous chapter, and in turn somewhat contribute to degradation of the performance of $\text{Li}/\text{NCM9163}$ cell shown in **Figure 4.3.15**. This implies that light reaction at surface by inserting small amount of SO_2 to form thinner film would be a solution to protect the bulk crystal structure of NCM9163.

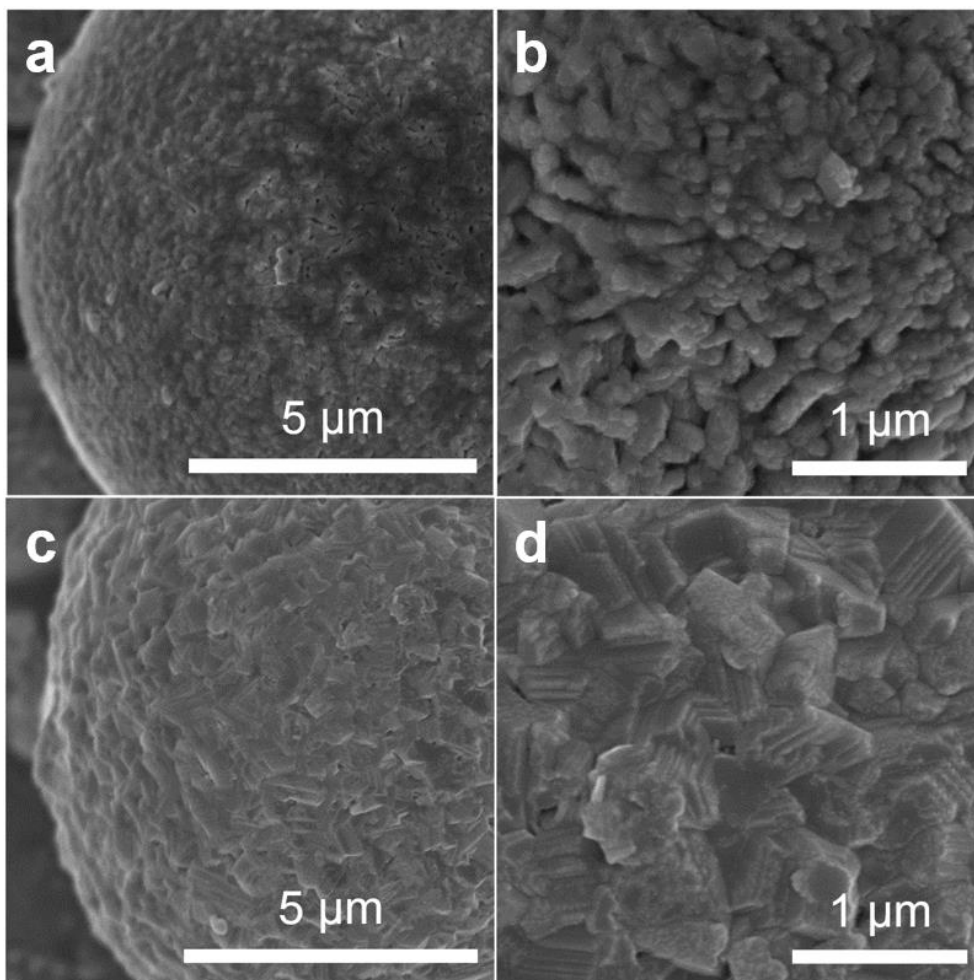


Figure 4.3.6. SEM images of (a and b) pristine NCM9163 particle and (c and d) surface-modified NCM9163 particle.

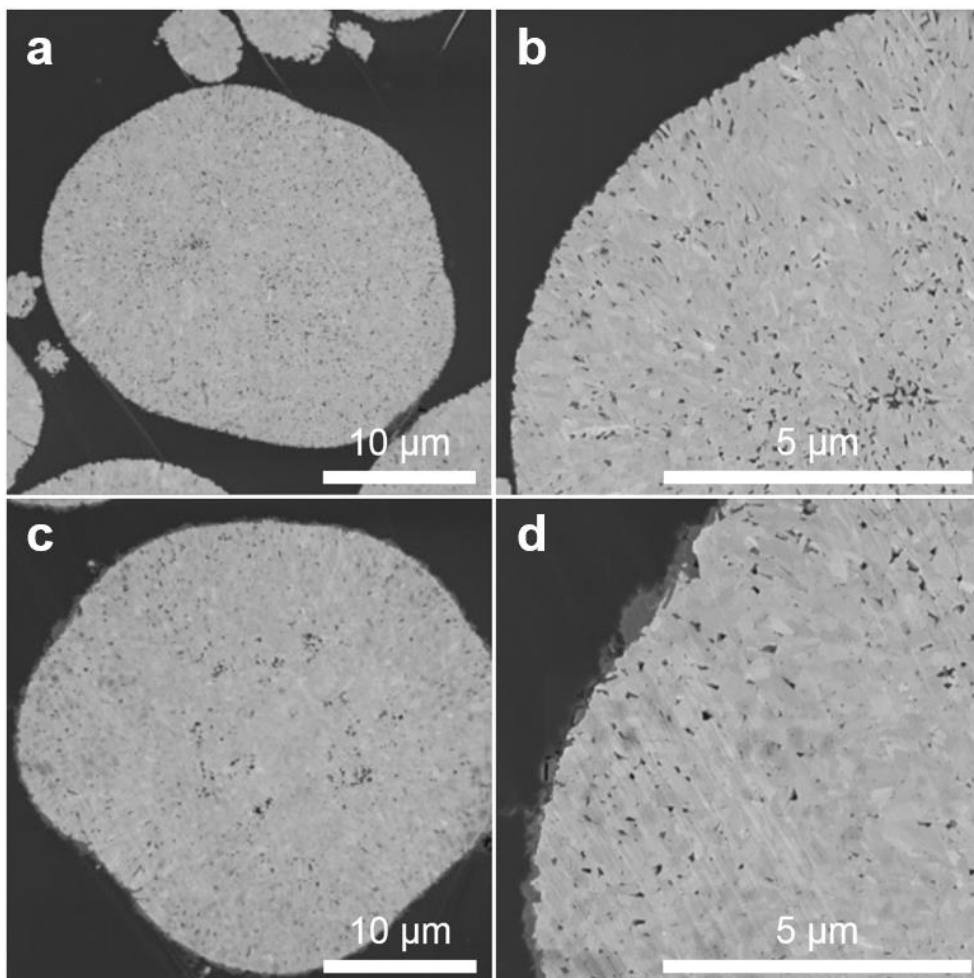


Figure 4.3.7. Cross-sectional SEM image of (a and b) pristine NCM9163 particle and (c and d) surface-modified NCM9163 particle.

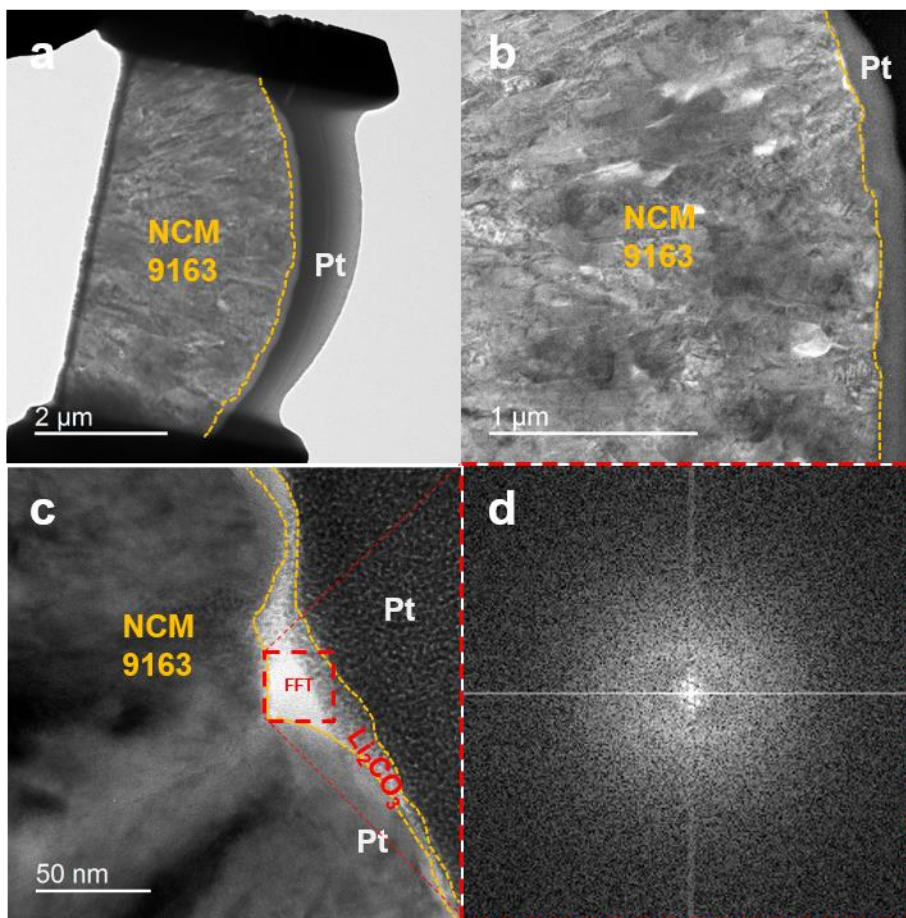


Figure 4.3.8. TEM images of the surface of NCM9163 pristine powder: (a) Low-magnification image for NCM9163 showing Pt deposition layer used to protect NCM9163 powder during milling by focused-ion beam (FIB) of Ga^+ . (b and c) High-magnification image of image (a). (d) fast-fourier-transformation calculation result from square region indicated by red-dotted line in (c).

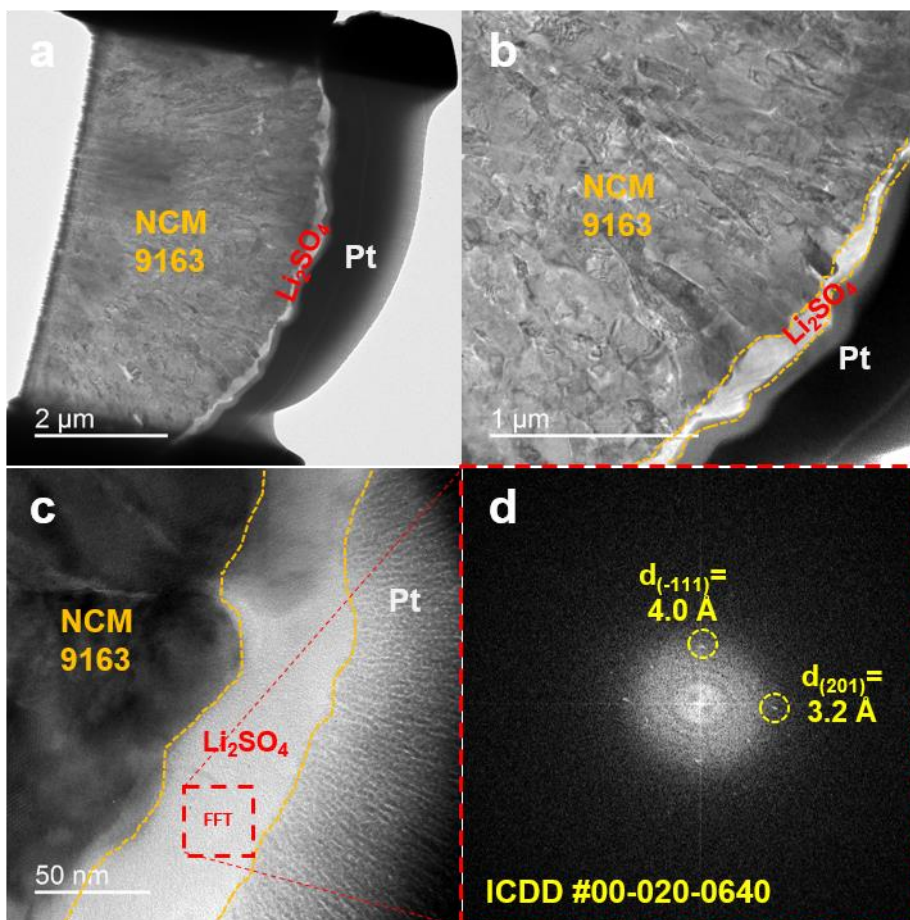


Figure 4.3.9. TEM images of the surface of NCM9163 pristine powder: (a) Low-magnification image for SO₂-treated NCM9163 showing Pt deposition layer used to protect NCM9163 powder during milling by focused-ion beam (FIB) of Ga⁺. (b and c) High-magnification image of image (a). (d) fast-fourier-transformation calculation result from square region indicated by red-dotted line in (c).

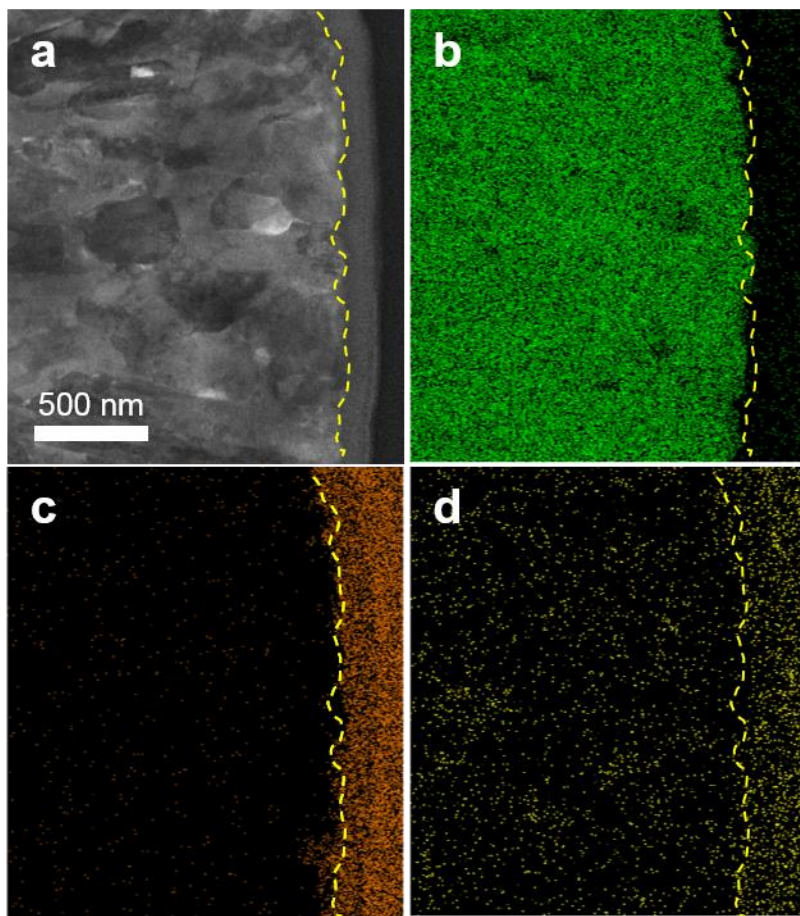


Figure 4.3.10. (a) STEM image of the surface region of NCM9163 pristine powder. STEM-EDS mapping result acquired from image in (a) for (b) Ni, (c) Pt, and (d) S.

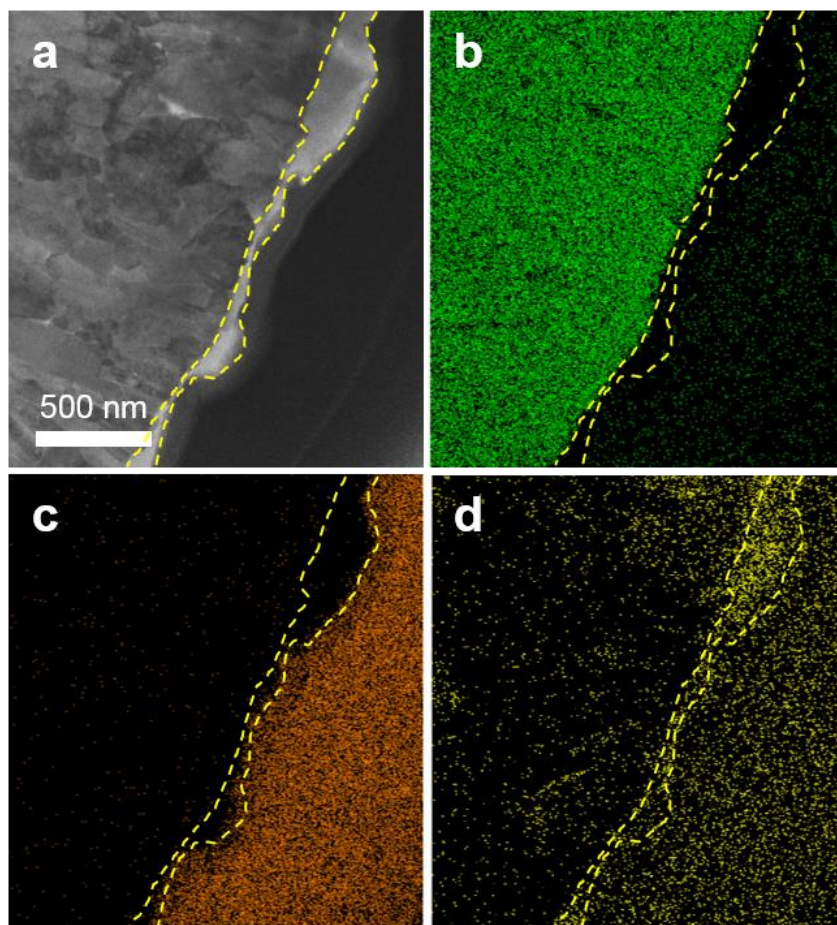


Figure 4.3.11. (a) STEM image of the surface region of SO₂-treated NCM9163 pristine powder. STEM-EDS mapping result acquired from image in (a) for (b) Ni, (c) Pt, and (d) S.

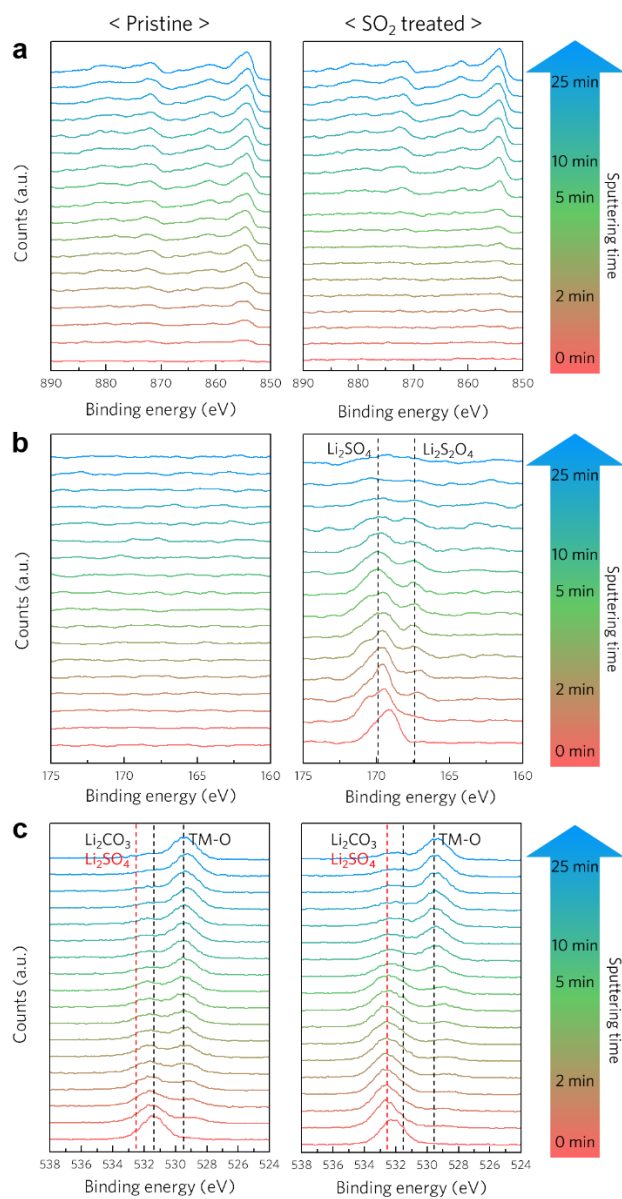


Figure 4.3.12. XPS spectra of (a) Ni 2p, (b) S 2p, (c) O 1s core electron from the surface of NCM9163 powder (left-side panels) and SO₂-treated NCM9163 powder (right-side panels).

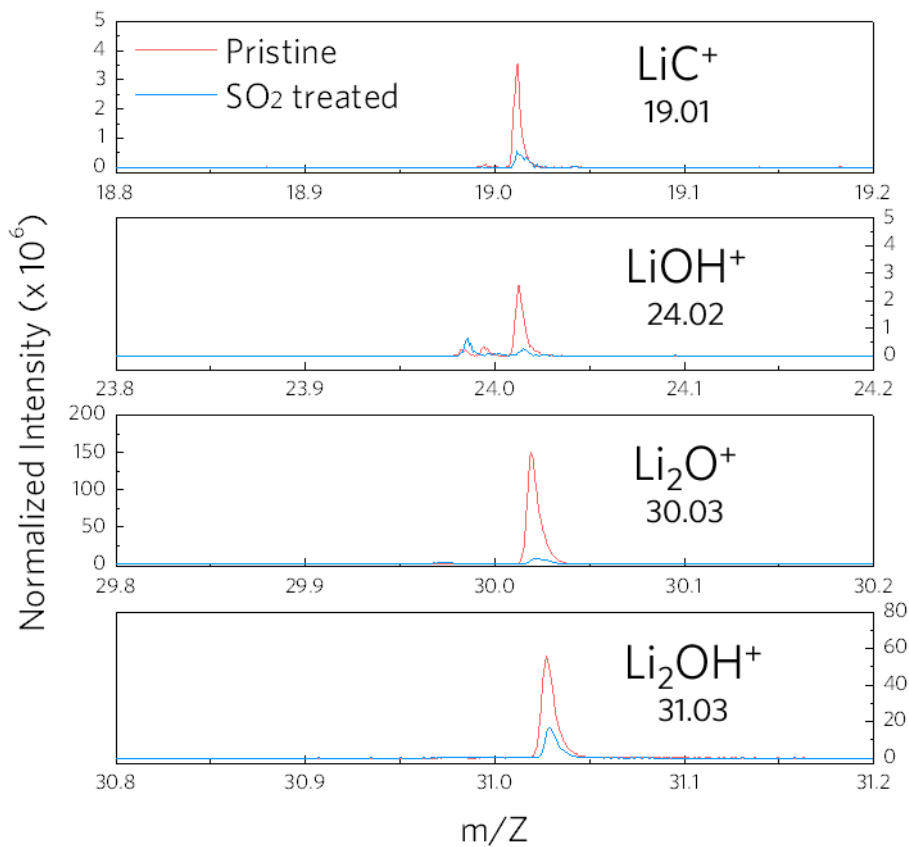


Figure 4.3.13. ToF-SIMS spectra showing peaks for LiC⁺, LiOH⁺, Li₂O⁺, and Li₂OH⁺ on NCM9163 and SO₂-treated NCM9163. Intensity was normalized by the total ion density.

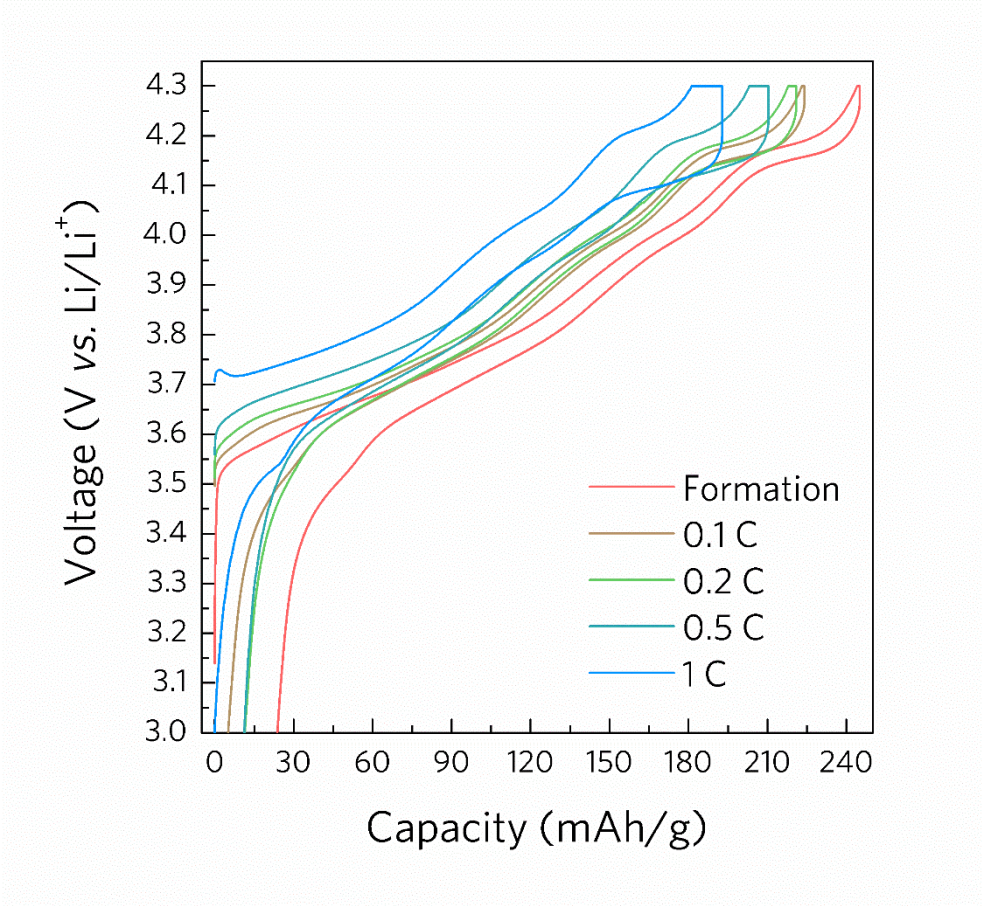


Figure 4.3.14. Voltage profile of Li/NCM9163 half-cell.

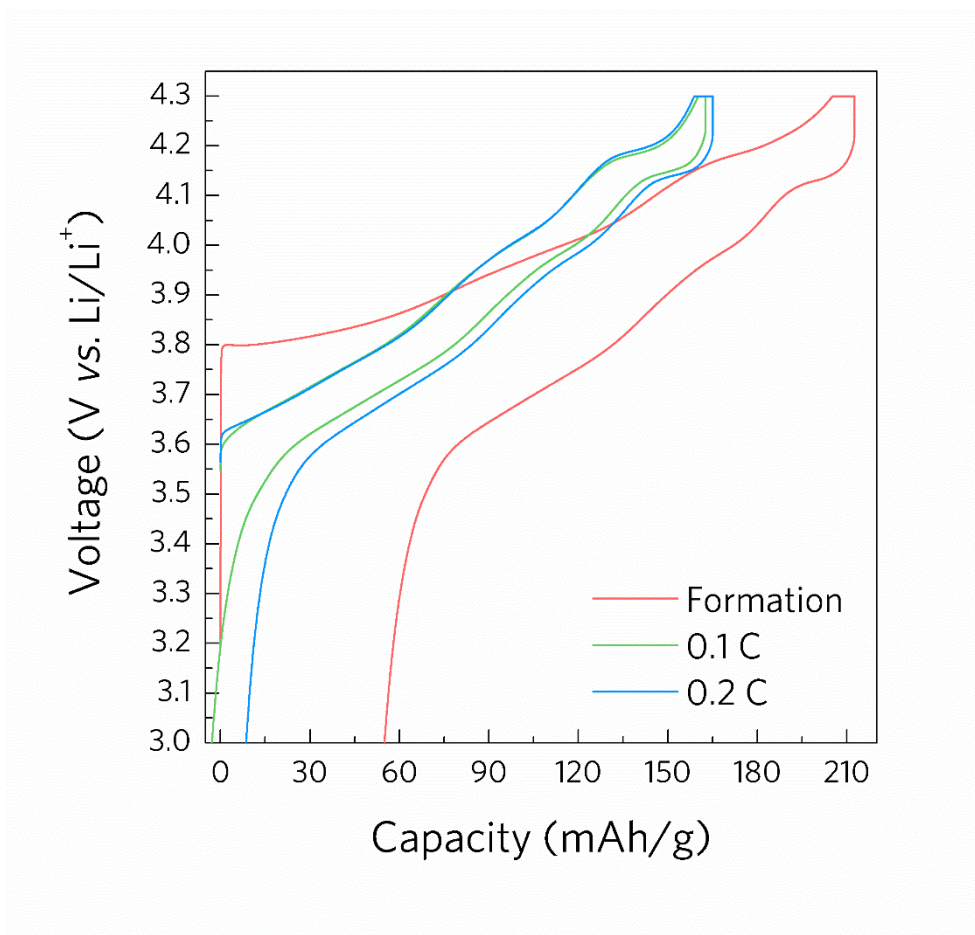


Figure 4.3.15. Voltage profile of Li/(SO₂-treated-NCM9163) half-cell.

4.3.3. Optimization of battery performance of SO₂-treated NCM9163

As mentioned above, optimization of battery performance of SO₂-treated NCM9163 should be conducted by decreasing the film thickness of Li₂SO₄ by inducing light reaction of NCM9163 with SO₂ gas. Therefore, diluted SO₂ in O₂ gas was used to modify the surface of NCM9163 during synthesis. The content of SO₂ in O₂ gas was 5 % (which is in turn 95 % of O₂ gas), and this gas was injected for the same duration, 1 min, with the SO₂-only case during the synthesis of NCM9163. Moreover, additional modification of reaction rate was tried by decreasing the flow rate of this O₂/SO₂ (5 %) gas systematically from 1.0 L min⁻¹ to 0.3 L min⁻¹. Synthesized NCM9163 powders with these various conditions were analyzed by measuring XRD patterns as shown in **Figure 4.3.16**. XRD patterns shown whole 2-theta region (left panel) seem to be almost the same irrespective of flow rate (left panel), and magnified at 20-30° region showed a few traces of Li₂SO₄ (right panel). This indicates much smaller amount of Li₂SO₄ on NCM9163 sample than that for the SO₂-only case, and maybe the formation of thin Li₂SO₄ film. When the amount of LiOH and Li₂CO₃ was obtained, as result shown in **Table 4.3.4**, both of them increased until as flow rate decreased to 0.5 L min⁻¹. When flow rate is 0.3 L min⁻¹, lower than 0.5 L min⁻¹, reduced amount of LiOH and Li₂CO₃ did not increase further. This is why we chose 0.3 L min⁻¹ condition as optimized condition to make thin and uniform film of Li₂SO₄.

To evaluate the electrochemical property of NCM9163 modified at the optimized condition, inserting diluted SO₂ gas at 500 °C during cooling at flow rate of 0.3 L min⁻¹, Li/(O₂/SO₂ (5 %)-treated NCM9163) cell was assembled and subjected to charge and discharge test. As displayed in **Figure 4.3.17**, discharge capacity of cell was 214 mA h g⁻¹ at 0.1 C, 201 mA h g⁻¹ at 0.2 C, 187 mA h g⁻¹ at 0.5

C, 178 mA h g⁻¹ at 1 C. The difference in discharge capacity between pristine and O₂/SO₂-treated-NCM9163 is small at low current (4 mA h g⁻¹ at 0.1 C) but the difference became slightly larger as current rate increases (15 mA h g⁻¹ at 1C). This means that intrinsic low electronic conductivity of Li₂SO₄ still somewhat influenced on the property of Li/NCM9163 cell at high current. From unchanged cycle retention property at 1C rate (**Figure 4.3.18**), however, it can be thought that the bulk property of NCM9163 is almost maintained by this surface modification.

Although it has been shown that the optimized surface modification condition of NCM9163 accomplished both of reduction of surface LiOH and Li₂CO₃ and maintaining battery performance, the reduction effect of those residual lithium decreased significantly by using dilute gas. As shown in **Table 4.3.4**, our optimized condition exhibited only 16 % (5114 ppm → 4316 ppm) decrease in residual lithium compared with pristine NCM9163. Thus, *in-situ* gas analysis during the charge of Li/NCM9163 cell using DEMS was conducted to evaluate the ability of mitigation of gas evolution effect despite only 16 % of residual lithium was reduced. To show clear difference, upper voltage limit for charge was increased to 4.8 V rather than 4.3 V which is conventional charge potential in commercialized cell. Interestingly, as shown in **Figure 4.3.19b**, DEMS result from Li/ (O₂/SO₂ (5 %)-treated-NCM9163) showed significantly mitigated evolution of CO₂ and O₂ gas during charge to 4.8 V (vs. Li/Li⁺). This is in stark contrast with DEMS result from Li/(pristine NCM9163) cell, which shows vigorous CO₂ evolution when the potential of cell surpassed 3.9 V (**Figure 4.3.19a**). Furthermore, there was no gas evolution until the cell was charged to 4.3 V, which means that there is will be no gas evolution in commercialized LIB when NCM9163 that undergone our surface modification method is applied to it. Because there was no evolution of SO₂ gas, it seems that thin coating of Li₂SO₄ is stable during the operation of battery. This mitigation of gas

evolution is not by just a decrease of site for side reaction, as shown in BET surface area analysis result. In **Figure 4.3.20**, BET specific surface area of SO₂-treated NCM9163 was all increased at both of 100%- and 5%-SO₂ case. Because gas evolution was alleviated even if the number of site for side reaction is increased, the reduction of residual lithium at surface can be indicated as a main reason for it. This result stresses the effectiveness of our surface modification method in mitigation of safety issue in LIBs. Also, we confirmed that slurry made from O₂/SO₂ (5 %)-treated NCM9163 was not gelled as shown in **Figure 4.3.21**. Thus, finally, our surface modification method was successful to resolve main problem induced by residual lithium compound in high-Ni NCM. This result is quite difficult to understand, because only 16 % of reduction in residual lithium affected the gas evolution rate and slurry gelation phenomenon as if all of residual lithium was removed. This might be related with the inaccuracy of way of measuring residual lithium by simple titration method. When NCM9163 powder is dispersed in water and stirred vigorously, not only LiOH and Li₂CO₃ at surface is dissolved in water, but also NCM9163 active material itself makes contact with water to additionally generate LiOH. This can in turn mean that not all of residual lithium compound measured by titration method came from surface of NCM powder. Only 16 % of reduction of residual lithium can alleviate gas evolution reaction considerably, and it implies that majority of residual lithium compound measured by titration method is generated by reaction of water with bulk NCM9163. Because layered structure collapsed significantly by reaction with concentrated SO₂ gas at high temperature (see changes of I₍₀₀₃₎/I₍₁₀₄₎ in **Table 4.3.2**), much higher extent of reduction of residual lithium shown in **Table 4.3.2** might come from degradation of bulk structure. When lithium came out from bulk to make excess amount of Li₂SO₄ and collapse layered structure, rate of ion-exchange between Li⁺ and H⁺ would be decreased because of decreased

number of reaction site. Until now, no other appropriate method than titration method has been developed, and our experimental results note that developing more efficient method for measuring residual lithium is highly required.

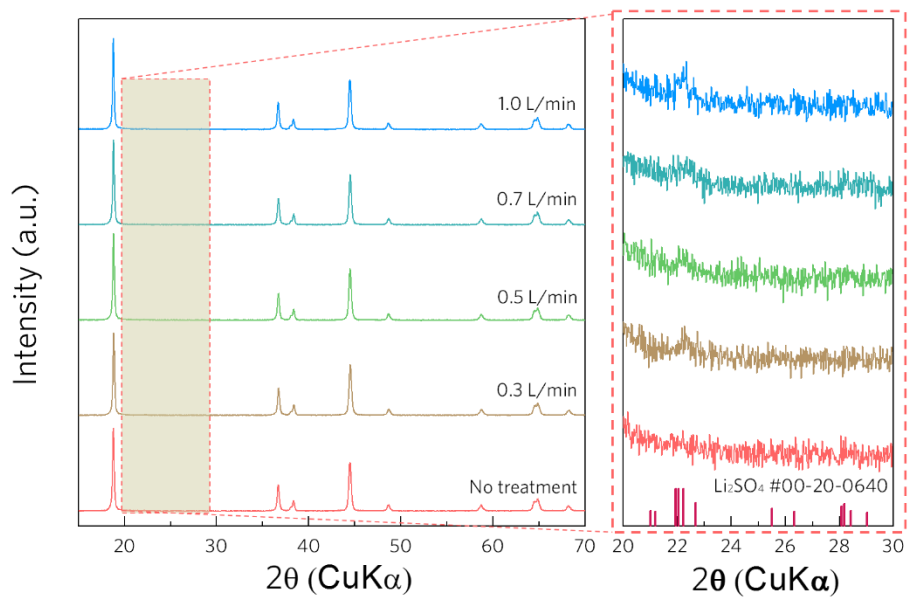


Figure 4.3.16. XRD patterns of NCM9163 reacted with diluted O₂/SO₂ (5%) mixture gas with various flow rate.

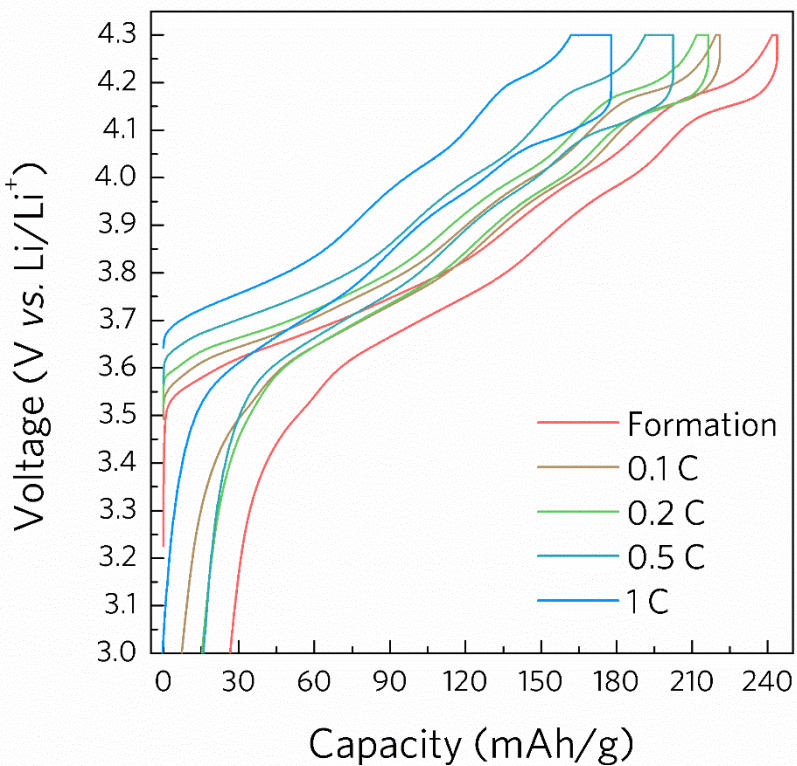


Figure 4.3.17. Voltage profile of Li/ (O₂/SO₂ (5%)-treated NCM9163) half-cell after surface treatment method was optimized.

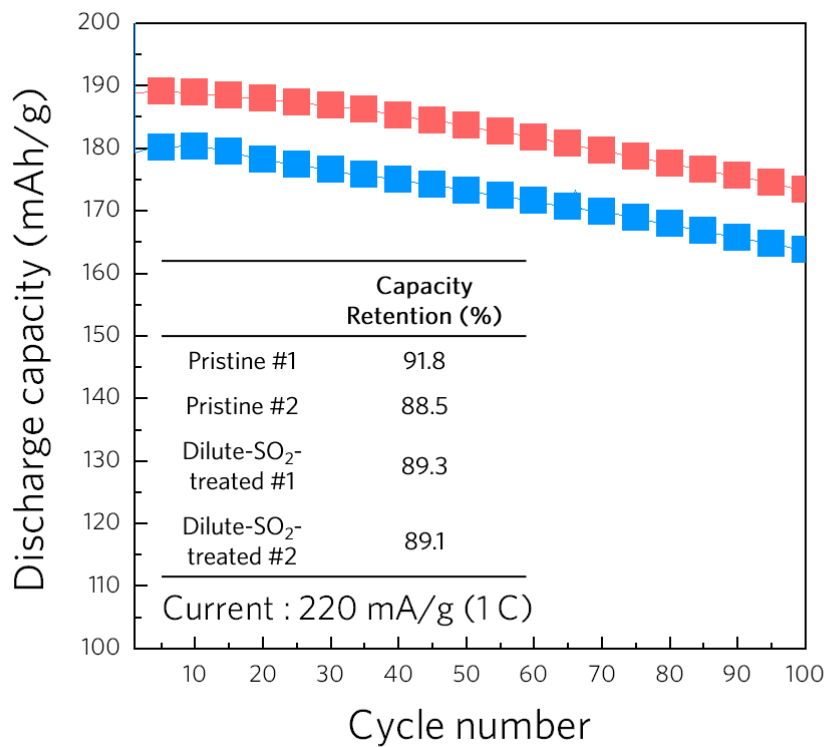


Figure 4.3.18. Cycle stability test result of Li/(O₂/SO₂ (5%)-treated NCM9163) powder whose surface modification condition was optimized compared with Li/(pristine NCM9163) cell.

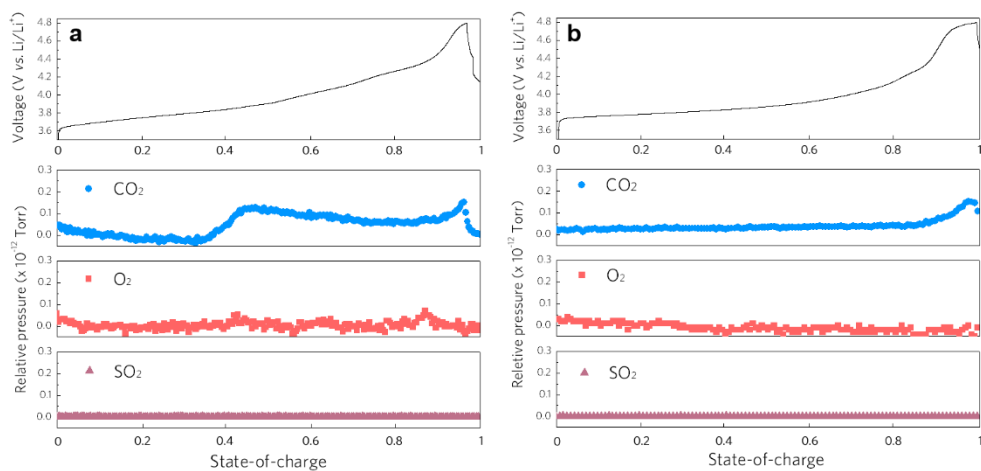


Figure 4.3.19. *In-situ* gas analysis result during charge process of the (a) Li/NCM9163 cell and (b) Li/ (O₂/SO₂ (5%)-treated NCM9163) cell by DEMS.

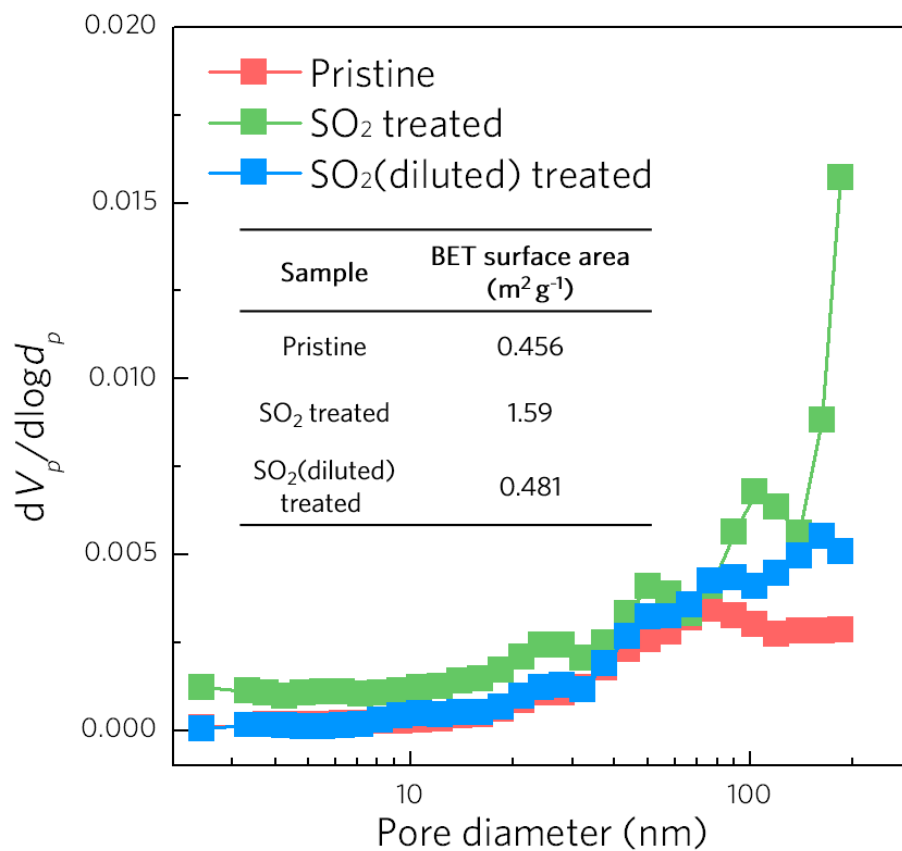


Figure 4.3.20. BJH pore size distribution plot and BET surface area of pristine NCM9163, SO₂-treated and O₂/SO₂ (5 %)-treated NCM9163 powder.

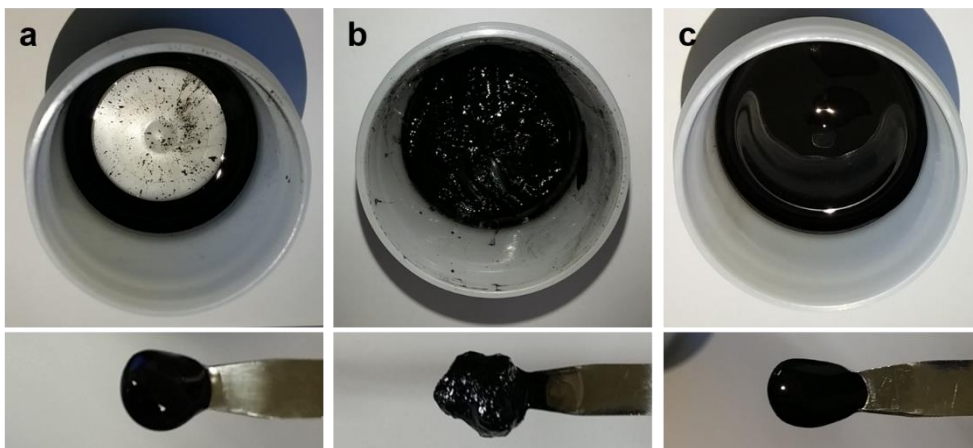


Figure 4.3.21. Photographs of slurry of (a) mixture of super-P carbon, PVDF binder and NMP solvent and (b) NCM9163 pristine powder mixed with slurry in (a), and (c) O₂/SO₂(5%)-treated NCM9163 power mixed with slurry in (a).

Sample	LiOH (wt%)	Li ₂ CO ₃ (wt%)	Total residual Li (ppm)	I ₍₀₀₃₎ /I ₍₁₀₄₎
No treatment (Reference)	1.62	0.218	5114	1.2
1 L min ⁻¹	1.16	0.201	3752	1.2
0.7 L min ⁻¹	1.26	0.192	3997	1.2
0.5 L min ⁻¹	1.37	0.198	4341	1.2
0.3 L min ⁻¹	1.36	0.195	4316	1.2

Table 4.3.4. Summary of the amount of residual lithium compounds of Diluted-SO₂-treated NCM9163 whose battery performance showed optimized properties.

4.4. Conclusion

In this report, we introduced a new *in-situ* gas-phase reaction method during the synthesis of high-Ni layered cathode material to modify its surface to reduce surface residual lithium compound, LiOH and Li₂CO₃. In this methodology, we injected reactive gas during annealing of high-Ni layered cathode material, LiNi_{0.91}Co_{0.06}Mn_{0.03}O₂ (NCM9163) in this case, shortly. We chose SO₂ gas as reactive gas, because it is able to react with LiOH and Li₂CO₃ to generate Li₂SO₄, which is much more thermodynamically stable phase. By injecting SO₂ gas at various point during synthesis, we could find the optimum point to reduce the LiOH and Li₂CO₃ without degradation of bulk crystal structure of NCM9163: moderately high temperature (~500 °C) during cooling step. It implies that the most of residual lithium compound is formed during cooling step, and this method can somewhat assist in understanding the fundamental mechanism of residual lithium formation. To minimize the deleterious effect of highly insulating nature of Li₂SO₄ to overall performance of battery, we additionally modified this method to decrease the layer of Li₂SO₄ film by using dilute SO₂ gas. This led to significant mitigation of both of gas evolution and slurry gelation effect without considerable degradation of battery performance including discharge capacity and cycle stability. This all-in-one method ruled out the necessity of post-treatment of high-Ni layered material such as washing, additional heat-treatment and coating of alien material. This is why additional optimization of this method can change the paradigm of synthesis method of high-Ni NCM to boost the commercialization of this material with high energy density to be applied to currently being investigated EVs and ESSs.

4.5. References

1. Chu, S.; Cui, Y.; Liu, N. *Nat. Mater.* **2016**, 16, 16.
2. Li, M.; Lu, J.; Chen, Z.; Amine, K. *Adv. Mater.* **2018**, 30, 1800561.
3. Tarascon, J. M.; Armand, M. *Nature* **2001**, 414, 359.
4. Armand, M.; Tarascon, J. M. *Nature* **2008**, 451, 652.
5. Eaves, S.; Eaves, J. *J. Power Sources* **2004**, 130, 208-212.
6. Thomas, C. E. *Int. J. Hydrogen Energy* **2009**, 34, 6005-6020.
7. Ligen, Y.; Vrubel, H.; Girault, H. *World Electric Vehicle Journal* **2018**, 9, 3.
8. Kim, J.; Kim, S. *IEEE Electrific. Mag.* **2018**, 6, 48-54.
9. Cano, Z. P.; Banham, D.; Ye, S.; Hintennach, A.; Lu, J.; Fowler, M.; Chen, Z. *Nat. Energy* **2018**, 3, 279-289.
10. Choi, J. W.; Aurbach, D. *Nature Reviews Materials* **2016**, 1, 16013.
11. Myung, S.-T.; Maglia, F.; Park, K.-J.; Yoon, C. S.; Lamp, P.; Kim, S.-J.; Sun, Y.-K. *ACS Energy Lett.* **2017**, 2, 196-223.
12. Nayak, P. K.; Erickson, E. M.; Schipper, F.; Penki, T. R.; Munichandraiah, N.; Adelhalm, P.; Sclar, H.; Amalraj, F.; Markovsky, B.; Aurbach, D. *Adv. Energy Mater.* **2018**, 8, 1702397.
13. Susai, F. A.; Sclar, H.; Shilina, Y.; Penki, T. R.; Raman, R.; Maddukuri, S.; Maiti, S.; Halalay, I. C.; Luski, S.; Markovsky, B.; Aurbach, D. *Adv. Mater.* **2018**, 30, 1801348.
14. Gauthier, M.; Carney, T. J.; Grimaud, A.; Giordano, L.; Pour, N.; Chang, H.-H.; Fenning, D. P.; Lux, S. F.; Paschos, O.; Bauer, C.; Maglia, F.; Lupart, S.; Lamp, P.; Shao-Horn, Y. *The Journal of Physical Chemistry Letters* **2015**, 6, 4653-4672.

15. Yu, X.; Manthiram, A. *Energy & Environmental Science* **2018**, 11 527-543.
16. Markevich, E.; Salitra, G.; Talyosef, Y.; Kim, U.-H.; Ryu, H.-H.; Sun, Y.-K.; Aurbach, D. *ACS Appl. Energy Mater.* **2018**, 1, 2600-2607.
17. Cho, W.; Myeong, S.; Kim, N.; Lee, S.; Kim, Y.; Kim, M.; Kang, S. J.; Park, N.; Oh, P.; Cho, J. *Adv. Mater.* **2017**, 29, 1605578.
18. Liu, W.; Oh, P.; Liu, X.; Lee, M.-J.; Cho, W.; Chae, S.; Kim, Y.; Cho, J. *Angew. Chem. Int. Ed.* **2015**, 54, 4440-4457.
19. Kim, J.; Lee, H.; Cha, H.; Yoon, M.; Park, M.; Cho, J. *Adv. Energy Mater.* **2018**, 8, 1702028.
20. Arai, H.; Okada, S.; Ohtsuka, H.; Ichimura, M.; Yamaki, J. *Solid State Ionics* **1995**, 80, 261-269.
21. Yoon, W.-S.; Balasubramanian, M.; Chung, K. Y.; Yang, X.-Q.; McBreen, J.; Grey, C. P.; Fischer, D. A. *J. Am. Chem. Soc.* **2005**, 127, 17479-17487.
22. Liu, H. S.; Zhang, Z. R.; Gong, Z. L.; Yang, Y. *Electrochem. Solid-State Lett.* **2004**, 7, A190-A193.
23. Abraham, D. P.; Twisten, R. D.; Balasubramanian, M.; Kropf, J.; Fischer, D.; McBreen, J.; Petrov, I.; Amine, K. *J. Electrochem. Soc.* **2003**, 150, A1450-A1456.
24. Cho, D.-H.; Jo, C.-H.; Cho, W.; Kim, Y.-J.; Yashiro, H.; Sun, Y.-K.; Myung, S.-T. *J. Electrochem. Soc.* **2014**, 161, A920-A926.
25. Kim, D.; Cha, J.; Kim, H. U.S. Patents 13/593,367, **2013**.
26. Jung, R.; Morasch, R.; Karayaylali, P.; Phillips, K.; Maglia, F.; Stinner, C.; Shao-Horn, Y.; Gasteiger, H. A. *J. Electrochem. Soc.* **2018**, 165, A132-A141.
27. Renfrew, S. E.; McCloskey, B. D. *J. Am. Chem. Soc.* **2017**, 139, 17853-17860.
28. Mahne, N.; Renfrew, S. E.; McCloskey, B. D.; Freunberger, S. A. *Angew.*

Chem. Int. Ed. **2018**, *57*, 5529-5533.

29. Park, J.-H.; Choi, B.; Kang, Y.-S.; Park, S. Y.; Yun, D. J.; Park, I.; Shim, J. H.; Park, J.-H.; Han, H. N.; Park, K. *Energy Technology* **2018**, *6*, 1361-1369.
30. Park, K.; Choi, B. *J. Alloys Compd.* **2018**, *766*, 470-476.
31. Kim, J.; Hong, Y.; Ryu, K. S.; Kim, M. G.; Cho, J. *Electrochem. Solid-State Lett.* **2006**, *9*, A19-A23.
32. Xiong, X.; Wang, Z.; Yue, P.; Guo, H.; Wu, F.; Wang, J.; Li, X. *J. Power Sources* **2013**, *222*, 318-325.
33. Choi, J.; Kim, J.; Lee, K.-T.; Lim, J.; Lee, J.; Yun, Y. S. *Adv. Mater. Interf.* **2016**, *3*, 1600784.
34. Park, K.; Park, J.-H.; Hong, S.-G.; Choi, B.; Seo, S.-W.; Park, J.-H.; Min, K. *Phys. Chem. Chem. Phys.* **2016**, *18*, 29076-29085.
35. Chen, S.; He, T.; Su, Y.; Lu, Y.; Bao, L.; Chen, L.; Zhang, Q.; Wang, J.; Chen, R.; Wu, F. *ACS Appl. Mater. Interf.* **2017**, *9*, 29732-29743.
36. Dean, John A. *Lange's Handbook of Chemistry, 12th ed.*; McGraw-Hill: New York, New York, **1979**.
37. Vegas, A.; Liebman, J. F.; Jenkins, H. D. B. *ACTA Crystallogr. B* **2012**, *68*, 511-527.
38. Abbas, Q.; Ratajczak, P.; Babuchowska, P.; Comte, A. L.; Bélanger, D.; Brousse, T.; Béguin, F. *J. Electrochem. Soc.* **2015**, *162*, A5148-A5157.
39. Kim, D.-H.; Paulsen, J., Sulfate Containing Rechargeable Battery Cathode with Oxidized Surface. U.S. Patents, 15/121,439, **2016**.
40. Bello-Teodoro, S.; Pérez-Garibay, R.; Bouchard, J. *Ind. Eng. Chem. Res.* **2014**, *53*, 7965-7970.
41. Shim, J.-H.; Kim, C.-Y.; Cho, S.-W.; Missiul, A.; Kim, J.-K.; Ahn, Y. J.; Lee, S. *Electrochim. Acta* **2014**, *138*, 15-21.

42. Reed, S. J. B. *X-Ray Spectrom.* **1975**, 4, 14-17.
43. Li, W.; Dolocan, A.; Oh, P.; Celio, H.; Park, S.; Cho, J.; Manthiram, A. *Nat. Commun.* **2017**, 8, 14589.
44. Rama Rao, S.; Bheema Lingam, C.; Rajesh, D.; Vijayalakshmi, R. P.; Sunandana, C. S. *Eur. Phys. J. Appl. Phys.* **2014**, 66, 30906.
45. Sun, H.-H.; Manthiram, A. *Chem. Mater.* **2017**, 29, 8486-8493.

Chapter 5. Concluding remarks

There is a growing significance of fundamental study on interfacial behavior between cathode and electrolyte in lithium rechargeable batteries to meet the demand on lithium rechargeable batteries with high energy density. Because a battery should endure more harsher condition such as high surrounding temperature and high voltage condition than ever, battery system for near future requires accordingly well-designed interface. However, delicate, systematic, and well-defined studies on fundamental understanding of interfacial behavior between these two components is still scarce due to difficulties in decoupling mixed factors related with this complex phenomenon and limitation of proper analytical methods. In this thesis, I investigated on the fundamental interplays between cathode and electrolyte in lithium-ion batteries, and discovered some new interfacial degradation mechanism of cathode accompanied by successful elucidation of underlying mechanism. Also I presented an effective way to address this interfacial problem of cathodes.

At first, high-temperature storage behavior of $\text{LiCoO}_2/\text{Electrolyte}$ interface is investigated, and I discovered a new phenomenon of accelerated reversible self-discharge in lithium batteries, which is called as abnormal self-discharge. By recording short-term thermal history to interface, lithium-rich material such as Li_3P and LiP is formed at surface of LiCoO_2 even after surrounding temperature is cooled down to room temperature. This new interfacial phenomenon is generated by vigorous reaction between LiPF_6 salt and LiCoO_2 surface, act as internal parasite to chemically provide lithium to charged Li_xCoO_2 to permanently accelerate self-discharge rate.

Second, interplay between LiCoO_2 and electrolyte at high-voltage

condition was investigated and a solution is suggested. When charge potential is increased to 4.8 V (vs. Li/Li⁺), resistive surface reconstruction layer formed at moderately high-voltage condition is rather dissolved out by vigorous cobalt dissolution (called as beneficial cobalt dissolution) to obtain superior cyclability in LiCoO₂. This so-called subtractive surface modification method enabled us to decouple the effect of surface and bulk during high-voltage cycling of LiCoO₂. Even during high-voltage cycling, thermodynamic instability of LiCoO₂ did not act as dominant a factor for battery performance, and surface reconstruction by side reaction with electrolyte primarily deteriorates cycle stability.

At last, cost-effective way to modify the reactive surface of LiNi_{0.91}Co_{0.06}Mn_{0.03}O₂ was suggested. In this *in-situ* gas-phase reaction method, reactive gas, SO₂ in this case was inserted shortly to transform surface residual lithium compound, LiOH and Li₂CO₃ into stable and non-reactive Li₂SO₄ during annealing process. This method rules out the necessity of post-treatment on high-Ni cathode material, and cut down the synthetic cost considerably. By forming stable Li₂SO₄ protective film on the surface of LiNi_{0.91}Co_{0.06}Mn_{0.03}O₂, problem of gas evolution due to side reaction with electrolyte and slurry gelation due to high basicity of cathode material was also significantly mitigated.

Interfacial behavior between cathode and electrolyte is receiving attention in other type of rechargeable battery whose guest ion is not lithium (Na, K, Mg, Ca, and so on) and next-generation battery such as metal-air, metal-sulfur, and even all-solid-state-battery. Therefore, it is highly expected that, this study might not only expand the frontier of understanding of interfacial behavior in conventional battery system, but also give hint or intuition to researches on other type of batteries to develop battery with unprecedented performance.

Chapter 6. Abstract in Korean

국문 초록

화석 연료의 사용으로 인한 범 지구적 환경 문제를 해결하기 위해 인류는 신재생 에너지를 이용한 전력 생산에 최근 관심을 기울이기 시작했다. 그러나 신재생 에너지는 그 공급이 장소와 시간 측면에서 일정하지 않아 생산된 전력을 저장해 두었다 필요 시에 공급할 수 있는 알맞은 저장 장치가 필요한데, 그 후보로서 최근 리튬 이차 전지가 각광받고 있다. 또한, 화석 연료를 사용하여 대용량의 에너지를 생산하던 자동차의 엔진을 이러한 전지를 이용하여 구동하려는 시도 또한 최근 전기 자동차의 출현으로 폭발적으로 증가하는 추세에 있다. 에너지 저장 시스템 (ESS) 및 전기 자동차 (EV)에 리튬 이차 전지를 적용하려면 기존에 비해 높은 에너지 밀도를 갖는 전지의 개발이 필수적이며, 이는 전지 내의 양극재의 에너지 밀도 증가를 필요로 한다. 이를 위해 기존 양극재의 작동 범위를 넓히거나 새로운 재료를 찾는 등의 시도 등이 있어 왔지만, 근본적으로 양극 재료와 계면을 이루는 전해질 사이의 적합성(compatibility)이 개선되지 않으면 아무리 좋은 성능의 양극재가 개발된다 하더라도 배터리 내의 활발한 부반응으로 인해 유발되는 저항 증가와 안정성 문제 등의 이유로 그 성과가 나타나기 어렵다. 그러나 매우 국소적인 계면 영역에서의 적절한 분석 장비가 한정되어 있으며 양극 및 전해질 모두에 대한 폭넓은 이해가 필요하다는 점 때문에 양극-

전해질 계면, CEI (Cathode-electrolyte interface) 에 대한 연구는 현재 까지도 양과 질적인 측면에서 모두 부족한 실정이다. 본 논문에서는 이러한 필요성에 따라 양극과 전해질 간의 계면 거동에 관한 기초 연구를 수행하고 CEI에서 나타나는 문제점들에 대한 개선 방안을 제시하고자 하였다.

2 장에서는, 단기간의 고온 저장만으로도 전해질 염(이 경우에는 LiPF_6)과 LiCoO_2 양극 사이의 반응에 의한 표면 재구성으로 인해 LiCoO_2 의 표면에 리튬이 풍부한 새로운 상을 갖는 재료가 형성됨을 밝혀냈다. 이 물질은 상온으로 돌아간 이후에도 마치 열 이력 (thermal history)의 형태로 표면에 영구적으로 남아 충전된 양극 재료에 화학적으로 리튬을 전달하여 배터리의 자가 방전 속도를 영구적으로 가속시킨다. 이러한 현상을 비정상 자가 방전(abnormal self-discharge)이라고 명명 하였으며, 상세한 메커니즘을 제안하였다.

3 장에서는, 배터리 고전압 사이클링을 위한 새로운 LiCoO_2 의 표면 개질법이 제안되었다. 본 연구에서는 극단적인 고전압 조건에서 LiCoO_2 의 표면 재구성 층이 오히려 용해되어 우수한 사이클 특성이 나타남을 밝혀냈다. 감산 표면 개질법 (subtractive surface modification) 이라 명명된 이 방법은 또한 고전압 사이클링 동안 LiCoO_2 의 표면 및 벌크에서 오는 배터리 성능 저하 효과를 분리하여 분석할 수 있게 해주었으며, 따라서 LiCoO_2 의 고전압 거동에 대한 새로운 이해를 바탕으로 한 고전압 사이클링 특성 개선 방안이 제시되었다.

4 장에서는 고니켈계 (High-Ni) $\text{LiNi}_{0.91}\text{Co}_{0.06}\text{Mn}_{0.03}\text{O}_2$ 양극재 표면의 잔류 리튬 (LiOH , Li_2CO_3)를 감소시키기 위한 새로운 표면 개질

방법이 제시되었다. 고니켈계 층상 전이 금속 산화물 표면에 잔류리튬 화합물이 표면에 다량 분포하는 것은 이 재료가 상용화 되는데 있어 가장 큰 장애물이었으며 후처리로 인한 합성 비용의 증가의 원인이 되어 왔다. 그러나 본 연구에서 제시된 방법은 소성 공정 중에 반응성이 높은 SO_2 가스를 짧은 시간 투입하여 표면의 LiOH 와 Li_2CO_3 를 열역학적으로 안정한 Li_2SO_4 로 변화시킴으로써 후처리의 필요성을 배제하여 합성 비용을 상당히 감소시켰으며, 동시에 표면 LiOH 및 Li_2CO_3 에 의해 야기되는 가스 발생, 슬러리의 겔화 등의 문제들 또한 완화했다.

주요어: 리튬 이차 전지, 대용량 저장시스템, 전기 자동차, 양극-전해질 계면 (CEI), 표면 재구성

학 번: 2011 - 22865

Chapter 7. Curriculum Vitae

| Education & Experiences |

- 03/2007 – 02/2011 B.S., Department of Materials Science and Engineering,
Seoul National University, Republic of Korea
- 06/2012 – 08/2012 World Class University (WCU) foreign education and
training program for graduate student, Electrochemical
Energy Laboratory, Department of Mechanical Engineering,
University of Colorado at Boulder (Prof. Sehee Lee)
- 03/2011 – 02/2019 Integrated Course of M. S. and Ph. D., Department of
Materials Science and Engineering, Seoul National
University, Republic of Korea
Supervisor : Prof. Kisuk Kang

| Research Interests & accomplishments |

- Crystalline cathode/anode materials for lithium-ion battery, and degradation mechanism of them during battery operation
- Interfacial behaviors in lithium-ion battery (solid/solid, solid/liquid and so on), and their effect on the performance of lithium-ion battery
- Expert in material characterization using various equipment: Analysis by X-ray diffraction (Rietveld refinement), transmission electron microscope (TEM), scanning electron microscope (SEM) and atomic force microscope (AFM)
- In-depth experience in a variety of material characterization techniques: Raman spectroscopy, focused ion beam (FIB), fourier-transform infrared (FT-IR) spectroscopy, X-ray photoelectron spectroscopy (XPS), time-of-flight secondary ion mass spectrometry (TOF-SIMS), differential electrochemical mass spectrometry

(DEMS)

| **First author publications** |

1. Controlling residual lithium chemistry during the synthesis of high-nickel (>90%) Li(Ni_xCo_yMn_z)O₂ cathode (*in preparation*)

Won Mo Seong, Ji-Won Park, Hyeokjun Park, Myeong Hwan Lee, Donggun Eum, and Kisuk Kang

2. Unveiling the intrinsic cycle reversibility of a LiCoO₂ electrode at 4.8-V cut-off voltage through subtractive surface modification for lithium-ion batteries

Won Mo Seong, Kyungho Yoon, Myeong Hwan Lee, Sung-Kyun Jung, and Kisuk Kang, *Nano Lett.* **2018**, *Online published*

(This paper is highlighted in *Nano Letters* by supplementary cover)

3. Abnormal self-discharge in lithium-ion batteries

Won Mo Seong, Kyu-Young Park, Myeong Hwan Lee, Sehwan Moon, Kyungbae Oh, Hyeokjun Park, Sechan Lee, and Kisuk Kang, *Energy Environ. Sci.* **2018**, *11*, 970-978.

4. Roughness of Ti substrates for Control of the Preferred Orientation of TiO₂ Nanotube Arrays as a New Orientation Factor

Won Mo Seong[†], Dong Hoe Kim[†], Ik Jae Park, Gyeong Do Park, Kisuk Kang, Sangwook Lee, and Kug Sun Hong, *J. Phys. Chem. C* **2015**, *119*, 13297-13305.

5. Nb-doped TiO₂ air-electrode for advanced Li-air batteries

Hee-Dae Lim[†], **Won Mo Seong**[†], Jinsoo Kim, Byungju Lee, Dong Hoe Kim, and

Kisuk Kang, *J. Asian Ceram. Soc.* **2015**, *3*, 77-81.

| Co-author publications |

1. Investigation on the interface between $\text{Li}_{10}\text{GeP}_2\text{S}_{12}$ electrolyte and carbon conductive agents in all-solid-state lithium battery

Kyungho Yoon, Jung-Joon Kim, **Won Mo Seong**, Myeong Hwan Lee, Kisuk Kang, *Sci. Rep.* **2018**, *8*, 8066.

2. Engineering Solid Electrolyte Interphase for Pseudocapacitive Anatase TiO_2 Anodes in Sodium-Ion Batteries

Zheng-Long Xu, Kyungmi Lim, Kyu-Young Park, Gabin Yoon, **Won Mo Seong**, Kisuk Kang, *Adv. Funct. Mater.* **2018**, *28*, 1802099.

3. Suppression of voltage decay through manganese deactivation and nickel redox buffering in high-energy layered lithium-rich electrodes

Kyojin Ku[†], Jihyun Hong[†], Hyungsub Kim, Hyeokjun Park, **Won Mo Seong**, Sung-Kyun Jung, Gabin Yoon, Kyu-Young Park, Haegyeom Kim, Kisuk Kang, *Adv. Energy Mater.* **2018**, *8*, 1800606.

4. Efficient method of designing stable layered cathode material for sodium ion batteries using aluminum doping

Hari Vignesh Ramasamy, Karthikeyan Kaliyappan, Ranjith Thangavel, **Won Mo Seong**, Kisuk Kang, Zhongwei Chen, Yun-Sung Lee, *J. Phys. Chem. Lett.* **2017**, *8*, 5021-5030.

5. Amorphous cobalt phyllosilicate with layered crystalline motifs as water oxidation

catalyst

Ju Seong Kim, Inchul Park, Eun-Suk Jeong, Kyoungsuk Jin, *Won Mo Seong*, Gabin Yoon, Hyunah Kim, Byunghoon Kim, Ki Tae Nam, Kisuk Kang, *Adv. Mater.* **2017**, *29*, 1606893.

6. High-efficiency and high-power rechargeable lithium–sulfur dioxide batteries exploiting conventional carbonate-based electrolytes

Hyeokjun Park, Hee-Dae Lim, Hyung-Kyu Lim, *Won Mo Seong*, Sehwan Moon, Youngmin Ko, Byungju Lee, Youngjoon Bae, Hyungjun Kim, Kisuk Kang, *Nat. Commun.* **2017**, *8*, 14989.

7. Lithium-free transition metal monoxides for positive electrodes in lithium-ion batteries

Sung-Kyun Jung, Hyunchul Kim, Min Gee Cho, Sung-Pyo Cho, Byungju Lee, Hyungsub Kim, Young-Uk Park, Jihyun Hong, Kyu-Young Park, Gabin Yoon, *Won Mo Seong*, Yongbeom Cho, Myoung Hwan Oh, Haegyeom Kim, Hyeokjo Gwon, Insang Hwang, Taeghwan Hyeon, Won-Sub Yoon, Kisuk Kang, *Nat. Energy*, **2017**, *2*, 16208.

8. Trackable galvanostatic history in phase separation based electrodes for lithium-ion batteries: a mosaic sub-grouping intercalation model

Kyu-Young Park, Jihyun Hong, *Won Mo Seong*, Jung-Joon Kim, Kyojin Ku, Byungju Lee, Kisuk Kang, *Energy Environ. Sci.* **2017**, *10*, 2352-2364.

9. Dissolution and ionization of sodium superoxide in sodium–oxygen batteries

Jinsoo Kim, Hyeokjun Park, Byungju Lee, *Won Mo Seong*, Hee-Dae Lim,

Youngjoon Bae, Haegyeom Kim, Won Keun Kim, Kyoung Han Ryu, Kisuk Kang, *Nat. Commun.* **2016**, *7*, 10670.

10. Niobium doping effects on TiO₂ mesoscopic electron transport layer-based perovskite solar cells

Dong Hoe Kim, Gill Sang Han, Won Mo Seong, Jin-Wook Lee, Byeong Jo Kim, Nam-Gyu Park, Kug Sun Hong, Sangwook Lee, Hyun Suk Jung, *Chem. Sus. Chem.* **2015**, *8*, 2392-2398.

11. High-performance flexible perovskite solar cells exploiting Zn₂SnO₄ prepared in solution below 100 °C

Seong Sik Shin, Woon Seok Yang, Jun Hong Noh, Jae Ho Suk, Nam Joong Jeon, Jong Hoon Park, Ju Seong Kim, Won Mo Seong, Sang Il Seok, *Nat. Commun.* **2015**, *6*, 7410.

12. CdS-sensitized 1-D single-crystalline anatase TiO₂ nanowire arrays for photoelectrochemical hydrogen production

Dong Hoe Kim, Hyun Soo Han, In Sun Cho, Won Mo Seong, Ik Jae Park, Jong Hoon Park, Sun Shin, Gyeong Do Park, Sangbaek Park, Sangwook Lee, Kug Sun Hong, *Int. J. Hydrogen Energy* **2015**, *40*, 863-869.

13. Observation of anatase nanograins crystallizing from anodic amorphous TiO₂ nanotubes

Ik Jae Park, Dong Hoe Kim, Won Mo Seong, Byung Suh Han, Gill Sang Han, Hyun Suk Jung, Mengjin Yang, Wen Fan, Sangwook Lee, Jung-Kun Lee, Kug Sun Hong, *CrystEngComm.* **2015**, *17*, 7346-7353.

14. Rheological and electrochemical properties of nanoclay added electrolyte for dye sensitized solar cells

Bo Ding, Youngsoo Jung, Dong Hoe Kim, **Won Mo Seong**, Sun-Dong Kim, Sang-Kuk Woo, Jung-Kun Lee, *Electrochim. Acta* 2014, 144, 275-281.

15. γ -Al₂O₃ nanospheres-directed synthesis of monodispersed BaAl₂O₄:Eu²⁺ nanosphere phosphors

Ik Jae Park, Hee-Suk Roh, Hee Jo Song, Dong Hoe Kim, Ju Seong Kim, **Won Mo Seong**, Dong-Wan Kim, Kug Sun Hong, *CrystEngComm* 2013, 15, 4797-4801.

16. Controlled synthesis and Li-electroactivity of rutile TiO₂ nanostructure with walnut-like morphology

Dong Hoe Kim, Kyung-Mi Min, Kyung-Soo Park, Ik Jae Park, In Sun Cho, **Won Mo Seong**, Dong-Wan Kim, Kug Sun Hong, *Dalton Trans.* **2013**, 42, 4278-4284.

17. Anatase TiO₂ nanorod-decoration for highly efficient photoenergy conversion

Dong Hoe Kim, **Won Mo Seong**, Ik Jae Park, Eun-Sang Yoo, Seong Sik Shin, Ju Seong Kim, Hyun Suk Jung, Sangwook Lee, Kug Sun Hong, *Nanoscale*, **2013**, 5, 11725-11732.

18. Transmittance optimized Nb-doped TiO₂/Sn-doped In₂O₃ multilayered photoelectrodes for dye-sensitized solar cells

Dong Hoe Kim, Sangwook Lee, Jong Hoon Park, Jun Hong Noh, Ik Jae Park, **Won Mo Seong**, Kug Sun Hong, *Sol. Energy Mater. Sol. Cells.* **2012**, 96, 276-280.

19. Crystallographically preferred oriented TiO₂ nanotube arrays for efficient photovoltaic energy conversion

Sangwook Lee, Ik Jae Park, Dong Hoe Kim, ***Won Mo Seong***, Dong Wook Kim, Gil Sang Han, Jin Young Kim, Hyun Suk Jung, Kug Sun Hong, *Energy Environ. Sci.* **2012**, *5*, 7989-7995.

| Awards |

2018, 12 Best graduate student award, Department of materials science & engineering, Seoul National University

2017, 10 Best poster award, 2017 fall conference of the Korean Institute of Metals and Materials

2015, 10 Best poster award, Materials fair 2015, Department of Materials Science and Engineering, Seoul National University

2012, 11 Excellence award, 2012 Campus Patent Strategy Universiade

| Patents |

1. KR 10-2018-0140301, 양극 활물질, 이의 제조방법 및 이를 포함하는 리튬 이차전지, POSITIVE ACTIVE MATERIAL, METHOD OF MANUFACTURING THE SAME AND RECHARGEABLE LITHIUM BATTERY INCLUDING THE SAME

Won Mo Seong, Kisuk Kang, Kwanghwan Cho, Ilseok Kim

| Conference participations |

2018, 11 Oral Presentation, 2018 MRS Fall meeting, Boston, Massachusetts, USA.

2018, 11 Poster Presentation, 2018 Fall Meeting of the Korean Ceramic Society,

Seoul, Republic of Korea

2018, 05 Oral Presentation, 233rd ECS meeting, Seattle, WA, USA

2017, 11 Oral Presentation, 2017 Fall Meeting of the Korean Electrochemical Society, Daejeon, Republic of Korea

2016, 11 Oral Presentation, 2016 Fall Meeting of the Korean Ceramic Society, Seoul, Republic of Korea

2015, 10 Poster Presentation, Materials fair, Department of Materials and Science, Seoul National University, Republic of Korea

2014, 09 Poster Presentation, Materials fair, Department of Materials and Science, Seoul National University, Republic of Korea

2013, 03 Oral Presentation, NANOSMAT-Asia, Wuhan, China

2012, 06 Poster Presentation, NANOTECH, Santa Clara, CA, USA

2011, 11 Poster Presentation, International Conference on Advanced Electromaterials (ICAE), Jeju, Republic of Korea